



Universiteit
Leiden
The Netherlands

Identification and characterization of novel factors in the DNA damage response

Singh, J.K.

Citation

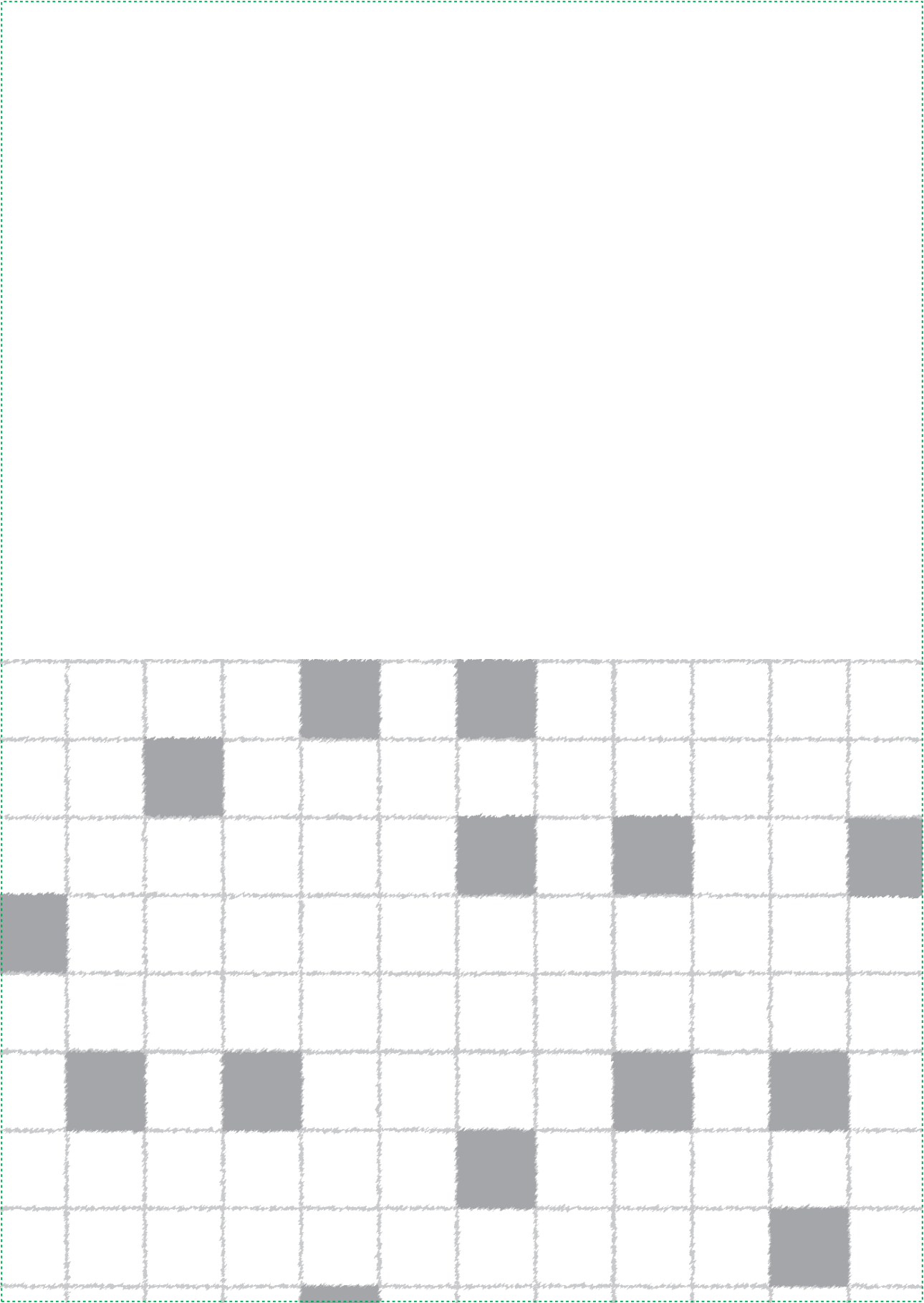
Singh, J. K. (2022, November 9). *Identification and characterization of novel factors in the DNA damage response*. Retrieved from <https://hdl.handle.net/1887/3485639>

Version: Publisher's Version

License: [Licence agreement concerning inclusion of doctoral thesis in the Institutional Repository of the University of Leiden](#)

Downloaded from: <https://hdl.handle.net/1887/3485639>

Note: To cite this publication please use the final published version (if applicable).



CHAPTER 3

Zinc finger protein ZNF384 is an adaptor of KU to DNA during classical non-homologous end-joining

Jenny Kaur Singh, Rebecca Smith, Magdalena B. Rother, Anton J.L. de Groot, Wouter W. Wiegant, Kees Vreeken, Ostiane D'Augustin, Robbert Q. Kim, Haibin Qian, Przemek M. Krawczyk, Román González-Prieto, Alfred C.O. Vertegaal, Meindert Lamers, Sébastien Huet and Haico van Attikum.

Published in *Nature Communications*

ABSTRACT

DNA double-strand breaks (DSBs) are among the most deleterious types of DNA damage as they can lead to mutations and chromosomal rearrangements, which underlie cancer development. Classical non-homologous end-joining (cNHEJ) is the dominant pathway for DSB repair in human cells, involving the DNA-binding proteins XRCC6 (KU70) and XRCC5 (KU80). Other DNA-binding proteins such as Zinc Finger (ZnF) domain-containing proteins have also been implicated in DNA repair, but their role in cNHEJ remained elusive. Here we show that ZNF384, a member of the C2H2 family of ZnF proteins, binds DNA ends *in vitro* and is recruited to DSBs *in vivo*. ZNF384 recruitment requires the poly(ADP-ribosyl) polymerase 1 (PARP1)-dependent expansion of damaged chromatin, followed by binding of its C2H2 motifs to the exposed DNA. Moreover, ZNF384 interacts with KU70/KU80 via its N-terminus, thereby promoting KU70/KU80 assembly and the accrual of downstream cNHEJ factors, including APLF and XRCC4/LIG4, for efficient repair at DSBs. Altogether, our data suggest that ZNF384 acts as a ‘Ku-adaptor’ that binds damaged DNA and KU70/KU80 to facilitate the build-up of a cNHEJ repairosome, highlighting a role for ZNF384 in DSB repair and genome maintenance.

Keywords: DNA double-strand break (DSB) repair, classical non-homologous end-joining (cNHEJ), DNA binding, ZNF384, KU70/KU80

INTRODUCTION

DNA double-strand breaks (DSBs) represent one of the most toxic lesions that can occur in the human genome. If left unrepaired or repaired incorrectly, they can lead to loss of genetic information, thereby contributing to the development of diseases, including cancer [1]. In order to maintain genomic stability, cells have evolved pathways for the signaling and repair of these DSBs [1]. DSB repair can occur by either homologous recombination (HR) or non-homologous end joining (NHEJ). HR is the more faithful repair pathway, which is active in the S and G2 phase of the cell cycle. It requires end-resection to form large stretches of single-stranded DNA (ssDNA), which in turn become coated by the ssDNA-binding complex RPA and the recombinase RAD51. Collectively, these and several other auxiliary factors contribute to HR by using the sister chromatid as a template for repair [2]. In contrast, the dominant repair pathway in human cells is canonical non-homologous end joining (cNHEJ), which requires minimal DNA-end processing and is initiated by the binding of KU70/KU80 heterodimers to the broken ends, followed by activation of DNA-PKcs and recruitment of APLF via its conserved KU-binding motif (KBM). This facilitates the assembly of the XLF-XRCC4-LIG4 complex, which stimulated by PAXX, ligates the broken ends predominantly in an error-free manner [3]. When cNHEJ is disabled, DSB repair can also occur via alternative non-homologous end joining (aNHEJ), which seals the broken ends in an error-prone fashion by microhomology usage and in a manner dependent on the XRCC1-Ligase III complex or POLQ [3]. Alternatively, in the case of more extensive end-resection microhomology usage may lead to deleterious, RAD52-dependent repair of DSBs via single-strand annealing (SSA) [4].

Efficient detection and repair of DSBs is complicated by the packaging of DNA into chromatin. ATP-dependent chromatin remodeling enzymes and a wide plethora of enzymes that induce post-translational modifications (PTMs) on damaged chromatin, including but not limited to acetylation, methylation and ubiquitylation, are therefore required to change chromatin structure at DSB sites to facilitate repair [5-7]. One of these enzymes is poly(ADP-ribose) polymerase 1 (PARP1), which becomes activated upon binding to DNA breaks and promotes chromatin expansion by the formation of poly(ADP-ribose) (PAR) chains on itself and adjacent nuclear proteins, such as histones, as well by promoting the recruitment of ATP-dependent chromatin remodelers in the vicinity of these breaks [8-10]. This increases chromatin accessibility and the recruitment of several DSB repair proteins, including KU70/KU80 and XRCC4, via direct PAR binding or DNA binding [9, 11].

Interestingly, a number of transcription factors have also been shown to localize at sites of DNA damage either in a PARP/PAR-dependent manner or via their DNA binding domains [11, 12]. Their role in DSB repair, is however, largely unknown. One such class of transcription factors are Zinc Finger (ZnF) domain-containing proteins. ZnF domains exist in approximately 5% of all human proteins and bind to a large variety of substrates including DNA, RNA, lipids and post-translational modifications (PTMs) [13, 14]. Due to their versatile binding ability, ZnF proteins play roles in different cellular processes such as transcription regulation, signal transduction and cell migration [15]. Interestingly, recent studies have implicated ZnF domain-containing proteins as new players in DSB repair [13]. For instance, ZMYND8 was found to play a role in transcription repression during DSB repair via HR [16], whereas ZNF830 promotes HR by facilitating RBBP8 (CTIP)-dependent DNA end resection [17]. ZNF281, on the other hand, was shown to promote XRCC4-dependent NHEJ of DSBs [18]. Together, these findings suggest a more important role for ZnF domain proteins in DSB repair than previously anticipated, although their mode of action is still poorly understood.

Here we describe an important regulatory role for the C2H2-type ZnF protein ZNF384 in DSB repair by cNHEJ. ZNF384 is recruited to sites of DNA damage in a manner dependent on PARP/PAR-mediated chromatin expansion followed by binding to the exposed DNA via its internal C2H2 domain. Moreover, ZNF384 physically interacts with KU70/KU80 via its N-terminus and both its interaction with DNA and KU70/KU80 are critical for efficient KU70/KU80 loading. This in turn allows for the assembly of a complete repairosome that includes cNHEJ proteins such as APLF and XRCC4/LIG4, thereby facilitating cNHEJ. Collectively, our data show that zinc-finger protein ZNF384 is an adapter of KU to DNA during DSB repair via cNHEJ.

RESULTS

ZNF384 is recruited to DNA damage sites and interacts with NHEJ proteins

ZNF384 was among the candidate ZnF proteins that localize to sites of DNA damage induced by laser micro-irradiation [12]. To validate this finding, we transiently co-expressed GFP-tagged ZNF384 (isoform 2, containing 6 C2H2 motifs) and the DNA damage sensor mCherry-NBS1 in *ZNF384* knockout (KO) U2OS cells (Supplementary Fig. 1A) and measured their recruitment to sites of DNA damage induced by multiphoton irradiation using live cell imaging (Supplementary Fig. 1B). GFP-ZNF384 was recruited

to NBS1-marked DNA damage sites within 1 minute and remained enriched at these sites for at least 3 minutes (Fig. 1A). We also observed the accumulation of endogenous ZNF384 at UV-A laser-induced DNA damage, which was completely abolished following ZNF384 knockdown, confirming the specificity of the ZNF384 antibody (Supplementary Fig. 1C). Since multiphoton and UV-A laser micro-irradiation may induce a variety of lesions other than DSBs, we next examined whether ZNF384 is specifically recruited to DSBs. First, we monitored its accumulation at chromatin regions micro-irradiated by ultra-soft X-rays (USX) [19]. Endogenous ZNF384 accumulated at USX-induced DSBs, co-localizing with γ H2AX (Supplementary Fig. 1D-E), and with the core NHEJ proteins KU70 and XRCC4 (Supplementary Fig. 1F-G). Second, we measured the co-localization between ZNF384 and γ H2AX at *Asi*SI nuclease-induced DSBs by proximity ligation assay (PLA) (Fig. 1B). We observed a clear co-localization between ZNF384 and γ H2AX at these DSBs (Fig. 1C), as well as between TP53BP1 (53BP1) and γ H2AX (Supplementary Fig. 1H-I and [20], showing the validity of the approach. Together, these observations demonstrate that ZNF384 is recruited to DSBs.

To gain insight into ZNF384's function at sites of DNA damage, we aimed to identify possible interaction partners of ZNF384. To this end, we generated U2OS Flp-In/T-Rex cells stably expressing inducible GFP-tagged ZNF384 or GFP-NLS, and performed GFP-trap-based pulldowns followed by label-free mass spectrometry (MS) (Fig. 1D). Our analysis revealed that ZNF384 interacts with 24 proteins that were at least 2-fold enriched in GFP-ZNF384 pulldowns when compared to those of GFP-NLS (Fig. 1D and Supplementary Table 1). Interestingly, KU70/KU80 and PARP1 belonged to the top-interactors, all of which regulate DSB repair via cNHEJ [9, 21]. GFP pulldowns coupled to western blot analysis confirmed that GFP-tagged ZNF384 interacts with endogenous KU70, KU80 and PARP1 (Fig. 1E), while reciprocal pulldowns of both GFP-KU80 (Fig. 1F) and GFP-PARP1 (Fig. 1G) revealed interactions with endogenous ZNF384. Moreover, we also confirmed the ZNF384-KU70 interaction endogenously (Fig. 1H), using *ZNF384* knockdown cells to show specificity of the ZNF384 signal in the KU70 immunoprecipitation (Supplementary Fig. 1J). To rule out an indirect interaction between these proteins we purified His-MBP-tagged ZNF384 and addressed its ability to bind KU70/KU80 *in vitro*. In agreement with our *in vivo* pulldown results, we found that recombinant ZNF384 bound recombinant KU70/KU80, demonstrating a direct protein-protein interaction (Fig. 1I). These findings suggest that ZNF384 forms a complex with KU70/KU80 and PARP1, manifesting a possible role for ZNF384 in NHEJ.

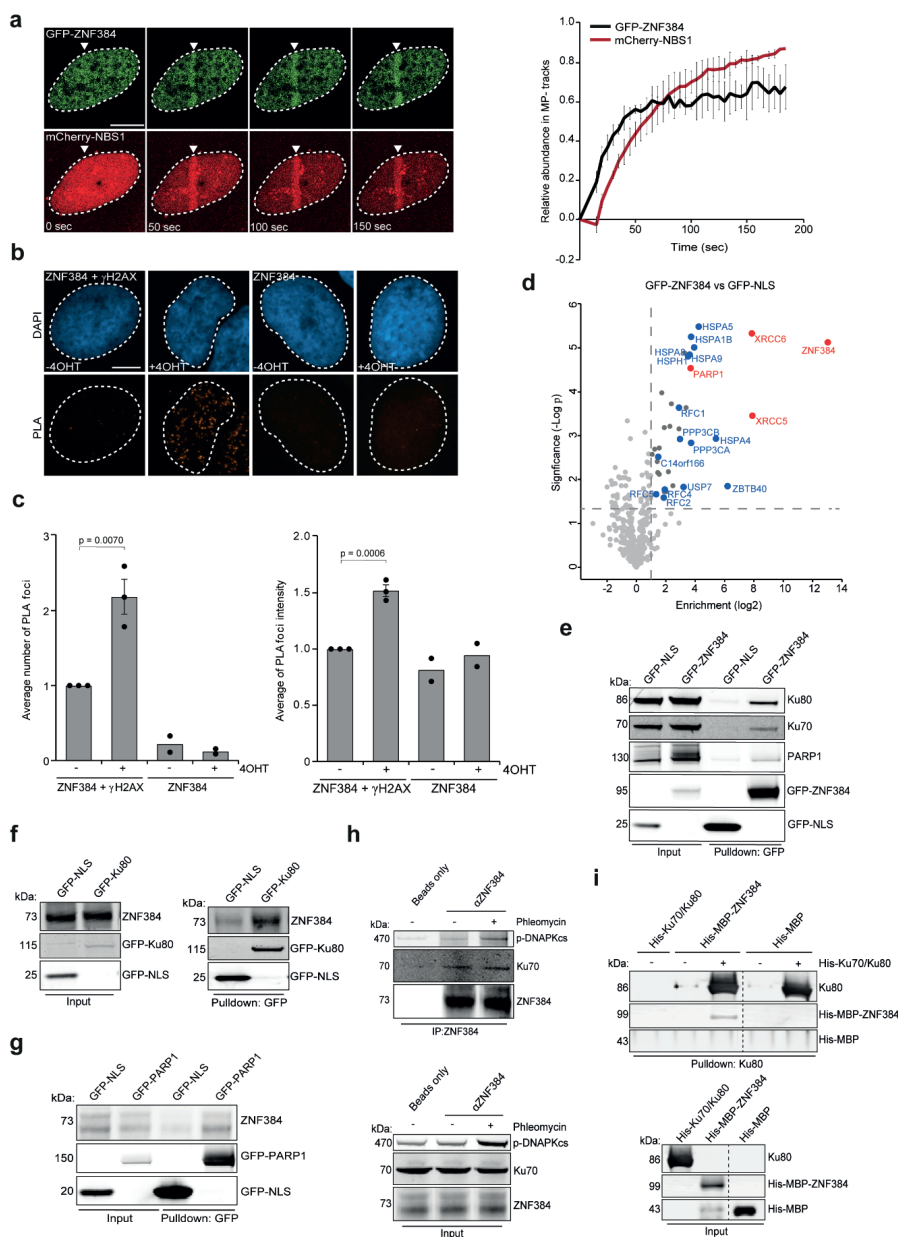


Figure 1. ZNF384 is recruited to DNA damage sites and interacts with NHEJ proteins. (A) Recruitment of GFP-ZNF384 to 800 nm multiphoton tracks in U2OS Flp-In/T-Rex *ZNF384* KO cells. mCherry-NBS1 was used as a damage marker (left panel). White triangles indicate irradiated regions. Quantification of the data is plotted on a time scale as relative abundance in tracks. Peak values were set to 1. The graph represents the mean \pm SD of >30 cells acquired in 2-3 independent

experiments (right panel). (B) PLA of ZNF384 and γ H2AX in *Asi*SI-ER-U2OS cells treated with 4-OHT for DSB induction. PLA foci were quantified after 5 hours of DSB induction. (C) Quantification of B. The mean \pm SEM of PLA foci formation and foci intensity from >200 cells acquired in 2-3 independent experiments are shown. Statistical significance was calculated using the two-tailed Student's *t* test. (D) Volcano plot depicting the statistical differences of the MS analysis on GFP-ZNF384 versus GFP-NLS pulldowns. The enrichment is plotted on the x-axis and the significance (t -test $-\log_2$ p-value) is plotted on the y-axis. NHEJ factors are shown in red and several hits are shown in blue (see also Supplementary Table 1). (E) Pulldowns of the indicated GFP fusion proteins in U2OS Flp-In/T-Rex cells. Blots were probed for GFP, KU70, KU80 and PARP1. (F) Pulldowns of the indicated GFP fusion proteins in HeLa cells. Blots were probed for GFP and ZNF384. (G) Pulldowns of the indicated GFP fusion proteins in HeLa cells. Blots were probed for GFP and ZNF384. (H) Immunoprecipitation (IP) of endogenous ZNF384 from 500 μ M Phleomycin treated U2OS cells. Control IP contained beads only. Blots were probed for ZNF384, p-DNA-PKcs (S2056) and KU70. (I) In *vitro* KU80 pulldown in the presence or absence of His-KU70/KU80 and His-MBP or His-MBP-ZNF384. Control IP contained beads only. Blots were probed for KU80 and MBP. Scale bar 5 μ m. Source data are provided as Source Data file.

ZNF384 recruitment to DNA damage sites requires the activity of PARP1

Because of ZNF384's interaction with KU70/KU80 and PARP1, we first analyzed whether it is recruited to DNA breaks via KU80. We observed that GFP-ZNF384 recruitment to UV-A laser micro-irradiation induced DNA damage, as well as that of the DNA damage marker NBS1 (Supplementary Fig. 2A-B), remained unchanged in cells depleted of KU80 or its interaction partner in the DNA-PK complex, DNA-PKcs kinase (Supplementary Fig. 2A-B) [22]. Moreover, we also found endogenous ZNF384 at γ H2AX marked UV-A laser-inflicted DNA damage to remain unaffected in cells depleted for KU70 (Supplementary Fig. 2C-D), KU80 or DNA-PKcs (Supplementary Fig. 2E), which was confirmed in *Xrcc6* KO hamster cells (Supplementary Fig. 2F-G, ruling out effects of incomplete knockdown. In addition, inhibition of DNA-PKcs kinase activity did not exert any effect on the recruitment of GFP-ZNF384 (Supplementary Fig. 2H) and endogenous ZNF384 (Supplementary Fig. 2I-J), suggesting that ZNF384 recruitment is independent of DNA-PK.

Next, we treated cells with the PARP1 and PARP2 inhibitor (PARPi) olaparib (Fig. 2A), and found this treatment to impair the recruitment of GFP-ZNF384 at multiphoton laser micro-irradiation (Fig. 2A), as well as UV-A laser micro-irradiation induced DNA damage (Supplementary Fig. 3A-B). Similarly, knockout of PARP1 alone or in combination with PARP2 completely impaired ZNF384 recruitment, whereas knockout of PARP2 alone, and knockdown of PARP3 had no major effect (Fig. 2B and Supplementary Fig. 3C-F). PARP3 knockdown, however, impaired KU80 recruitment as expected (Supplementary Fig. 3G-H) [23]. Importantly, we previously showed that PARP1 itself is still recruited

to sites of DNA damage in PARPi-treated cells [24], suggesting that the recruitment of ZNF384 does not involve a physical interaction between ZNF384 and PARP1, but rather relies on PARP1's activity. Possibly, this interaction is important for the PARP1-dependent PARylation of ZNF384, which we and others observed in response to DSB induction (Supplementary Fig. 3I), in accordance with a previous report [25]. Collectively, these results suggest that ZNF384 is rapidly recruited to DSB-containing tracks in a manner dependent on the activity of PARP1.

PARP1-dependent chromatin unfolding facilitates DNA binding of ZNF384 at DNA damage sites

We next asked whether the PARP1 activity-dependent recruitment of ZNF384 to DNA breaks could be due to direct binding of ZNF384 to PARP1-generated PAR moieties. To investigate this, we used a previously established fluorescence three-hybrid assay (Supplementary Fig. 4A) [26]). This assay measures the ability of a lacO-anchored putative 'ADP-ribose-binding' protein of interest to interact with PARylated PARP1 that is naturally released from sites of laser-induced DNA damage and is then free to diffuse and bind to the lacO-anchored PAR-binder. Indeed, we observed recruitment of PARylated PARP1 to the lacO-anchored macrodomain of macroH2A1.1, a well-characterized PAR binding protein [11, 27], which was abolished following treatment with PARPi, but remained unaffected by treatment with PARGi (likely to due to the availability of a limited number of lacO-anchored macrodomain molecules) (Supplementary Fig. 4B-D). In contrast, we did not observe an interaction between lacO-anchored ZNF384 and PARylated PARP1 (Supplementary Fig. 4E,F). To corroborate and extend these findings, we used a second independent approach that can discriminate whether ZNF384 is recruited by binding to PAR, or to DNA that becomes exposed upon PAR-dependent chromatin relaxation. In this assay *ZNF384* KO cells were micro-irradiated and, 240 seconds post-irradiation, after the completion of the initial wave of PARP/PAR-dependent chromatin relaxation [9, 26, 28], PARPi was added to acutely block PARP enzymatic activity. Under these conditions PAR-binding proteins are rapidly released from the damaged area, while proteins that bind DNA are maintained [11]. Indeed, we observed that the WWE domain of RNF146, which is a known PAR-binder [29], was rapidly released from the irradiated area (Fig. 2C-D and Supplementary Fig. 5A). While its binding was nearly completely reversed at 450s post-irradiation due to rapid degradation of PAR (Supplementary Fig. 5A), counteracting the removal of PAR

chains by adding PARGi to the PARPi-treated cells preserved the accumulation of the WWE domain at sites of DNA damage (Supplementary Fig. 5A-B). In contrast, PARPi treatment did not revert the recruitment of GFP-ZNF384 at the damaged area (Fig. 2E-F), suggesting that ZNF384 does not bind PAR, but rather associates with DNA. To corroborate these findings, we investigated whether DNA binding of ZNF384 depends on PARP/PAR-dependent chromatin relaxation, which we and others have shown to facilitate the association of DNA-binding proteins with DNA at sites of damage [9, 26, 28]. We found that overexpression of the ATP-dependent chromatin remodeler ALC1, which enhances chromatin unfolding without affecting PAR-signaling (Supplementary Fig. 5C and), increased ZNF384 accumulation at sites of DNA damage when compared to that after overexpression of ATPase-dead (E175Q) ALC1 (Fig. 2G). PARPi treatment inhibited ZNF384 recruitment in both WT ALC1 and ATPase-dead (E175Q) ALC1 overexpressing cells (Fig. 2G), consistent with the PARP-dependent recruitment of these proteins [8]. Interestingly, we did not find a significant enrichment of ZNF384 in chromatin-enriched extracts from cells treated with phleomycin (Supplementary Fig. 5D-E), nor a change in ZNF384 turnover at DNA lesions as measured by FRAP (Supplementary Fig. 5F-H), suggesting that the binding of ZNF384 to damaged DNA is not qualitatively different from its binding to undamaged DNA and is mostly triggered by the increased accessibility of DNA consecutive to PAR-driven chromatin relaxation. This behaviour of ZNF384 is comparable to that of the DNA binding domain BZIP of C/EBPa (Supplementary Fig. 5I and [11]) and the chromatin remodeler CHD4 (Supplementary Fig. 5I and [26]), which were both shown to recruit to DNA lesions due to increased accessibility of damaged DNA through PAR-dependent chromatin unfolding. In contrast, the ZNF384 interaction partners and DNA-end binding proteins KU70/KU80 showed a clear slowing of its turnover following DNA damage (Supplementary Fig. 5J). Thus, ZNF384 recruitment is dependent on PAR-dependent chromatin unfolding, allowing ZNF384 to bind to the exposed damaged DNA.

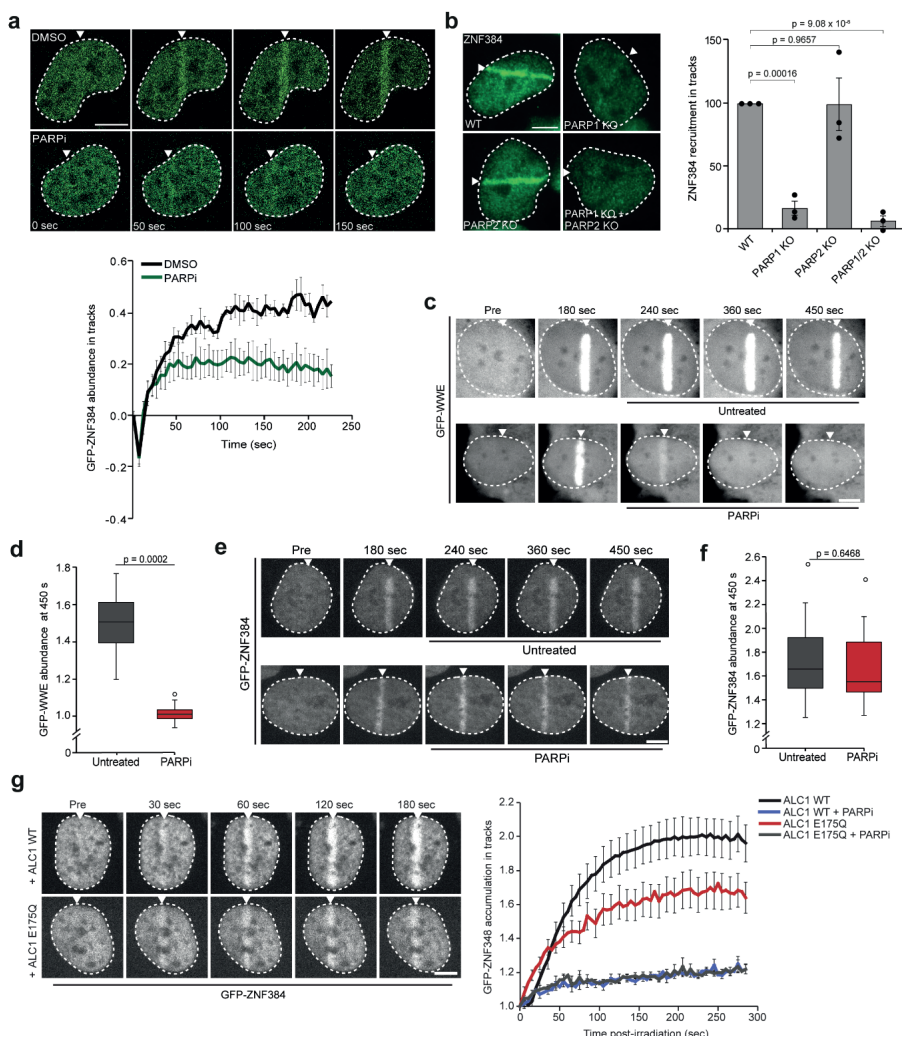


Figure 2. PARP1 activity facilitates DNA binding of ZNF384 at sites of damage. (A) GFP-ZNF384 recruitment to 800 nm multiphoton tracks in stable U2OS Flp-In/T-Rex cells treated with PARP inhibitor (PARPi) for 1 hour before micro-irradiation (top panel). Quantification of the data is presented as the mean \pm SEM of >35 cells acquired in 3 independent experiments (bottom panel). (B) ZNF384 recruitment to 365 nm UV-A tracks 10 minutes after DNA damage induction in BrdU-sensitized wildtype (WT) and indicated KO U2OS cells (left panel). The mean \pm SEM of >180 cells from 3 independent experiments is shown (right panel). (C) Confocal images showing accumulation of GFP-WWE at sites of 405 nm laser micro-irradiation in Hoechst-sensitized U2OS cells. Cells were left untreated or treated with PARPi 180 seconds after DNA damage induction. (D) Boxplot limits correspond to the 25th and 75th percentiles and the center line in the box indicates the median value of the accumulation of GFP-WWE at 450 sec post irradiation from 23-25 cells from a representative of 3 independent experiments. (E) As in C, except for GFP-ZNF384. (F) As in D, except for GFP-ZNF384 from 21-27 cells. (G) GFP-ZNF384 recruitment to 405 nm laser tracks in U2OS cells overexpressing iRFP-ALC1 wildtype (WT) and iRFP-ALC1 ATPase-dead (E175Q)

treated with PARPi for 1 hour before micro-irradiation (left panel). GFP-ZNF384 recruitment is displayed as intensity integrated over the damaged area (right panel). The mean \pm SEM from 13-16 cells from a representative of 3 independent experiments is shown. White triangles indicate irradiated regions. Scale bar 5 μ m. Source data are provided as a Source Data file. Boxplot limits correspond to the 25th and 75th percentiles and the center line in the box indicates the median value. The whiskers extend 1.5 times the interquartile range. All P-values were calculated using the unpaired Student's *t* test, assuming unequal variances.

Previous work indeed showed that ZNF384 belongs to one of the few C2H2-type of ZnF proteins reported to have unique DNA binding affinity, particularly for homopolymeric dA:dT DNA consensus elements enriched in the genome [30]. We performed biolayer interferometry (BLI) experiments and *in vitro* DNA pulldown experiments using purified His-MBP-tagged ZNF384 and confirmed that His-MBP-ZNF384, in contrast to His-MBP alone, has a high affinity to bind T-rich single-strand (ss)DNA (Supplementary Fig. 6A-B), as opposed to A-rich ssDNA (Fig. 3A). Extending this finding, we also found ZNF384 to bind double-stranded (ds)DNA with either a 3'- or 5' overhang in both BLI and *in vitro* DNA pulldown assay, albeit with a seemingly lower affinity when compared to ssDNA (Fig. 3A-B). Importantly, ZNF384 bound poorly, if at all, to dsDNA, and did not show RNA binding (Supplementary Fig. 6C). Moreover, it showed reduced colocalization with ethynyl uridine labeled RNA compared to Hoechst labeled DNA as quantified by the Pearson correlation coefficient (Supplementary Fig. 6D). Collectively, these results suggest that ZNF384 recruitment to DNA damage sites is dependent on PARP-induced chromatin relaxation and its affinity to bind damaged DNA *in vivo* and *in vitro*.

ZNF384 is recruited to sites of DNA damage via its C2H2 DNA binding motif

The fact that ZNF384 is recruited to DNA damage and binds DNA, encouraged us to investigate whether the C2H2, N-terminal or C-terminal domain of ZNF384 is implicated in this process (Fig. 3C). To this end, we purified His-MBP-tagged versions of these ZNF384 domains (Supplementary Fig. 6A), and assessed their ability to bind dsDNA with a 3' overhang, a common substrate found at DNA breaks, *in vitro* by BLI and DNA-pulldown assay. As expected, full-length ZNF384 was able to bind this DNA substrate, whereas its N-terminus C-terminus revealed very poor to no binding (Supplementary Fig. 7A-B). In contrast, the C2H2 domain showed a stronger binding to this substrate, which was even comparable to that of full-length ZNF384 in the BLI assay (Supplementary Fig. 7C). Finally, we also observed that the C2H2 domain, similar to full-length ZNF384, has affinity for ssDNA, as well as for dsDNA with a 3'- or 5'-overhang,

albeit that the affinity for the latter two substrates was seemingly lower when compared to that for ssDNA (Supplementary Fig. 7D). Together, these findings show that ZNF384 binds different DNA substrates through its C2H2 domain.

Given the different DNA binding affinities of these ZNF384 domains, we next assessed their relevance for ZNF384 recruitment to DNA damage sites. To this end, we studied the recruitment of GFP-tagged versions of the C2H2, N-terminal or C-terminal domains to UV-A laser micro-irradiation inflicted DNA damage (Fig. 3D) in *ZNF384* KO U2OS. This was to avoid the possible dimerization of any of the GFP-tagged domains with endogenous ZNF384 as observed for GFP-ZNF384 and endogenous ZNF384 (Supplementary Fig. 7E). mCherry-NBS1 was co-expressed in these cells to control for DNA damage induction (Supplementary Fig. 7F). In agreement with our *in vitro* experiments, we found that the C2H2 domain was still recruited, while the N-terminus and C-terminus recruitment was completely abolished (Fig. 3D). Consistently, we also found the colocalization between ZNF384 and DNA to be dependent on its C2H2 motif (Supplementary Fig. 6C).

Next, we sought to test the DNA binding affinity of ZNF384 deletion mutants *in vivo*. We generated a Δ C2H2 mutant lacking the 6 C2H2 motifs, (Δ C2H2), as well as mutants lacking the N-terminus (Δ N-terminus) or C-terminus (Δ C-terminus) (Supplementary Fig. 7G), and estimated the ability of full-length ZNF384 and Δ C2H2 to bind DNA using FRAP. In this assay, strong DNA binding affinity corresponds to a slow FRAP recovery and *vice versa*. While full-length ZNF384 showed a slow recovery after photobleaching of the damaged area, we observed a fast recovery of the Δ C2H2 ZNF384. In contrast, ZNF384 Δ N-terminus- and Δ C-terminus showed a slower FRAP recovery compared to full-length ZNF384, suggesting that both domains slightly destabilize ZNF384's interaction with DNA (Fig. 3E and Supplementary Fig. 7H). We then assessed the recruitment of these GFP-tagged deletion mutants to DNA damage 405 laser micro-irradiation in Hoechst-sensitized *ZNF384* KO U2OS. Core histone H2B fused to photoactivatable PTagRFP (PTR) was co-expressed to define the damaged area. We found that Δ C2H2 dramatically impaired ZNF384 recruitment, while Δ N-terminus and Δ C-terminus had no major effect on recruitment (Fig. 3F). Collectively, these findings suggests that the C2H2 motif is important for DNA binding and recruitment of ZNF384 at DNA damage sites.

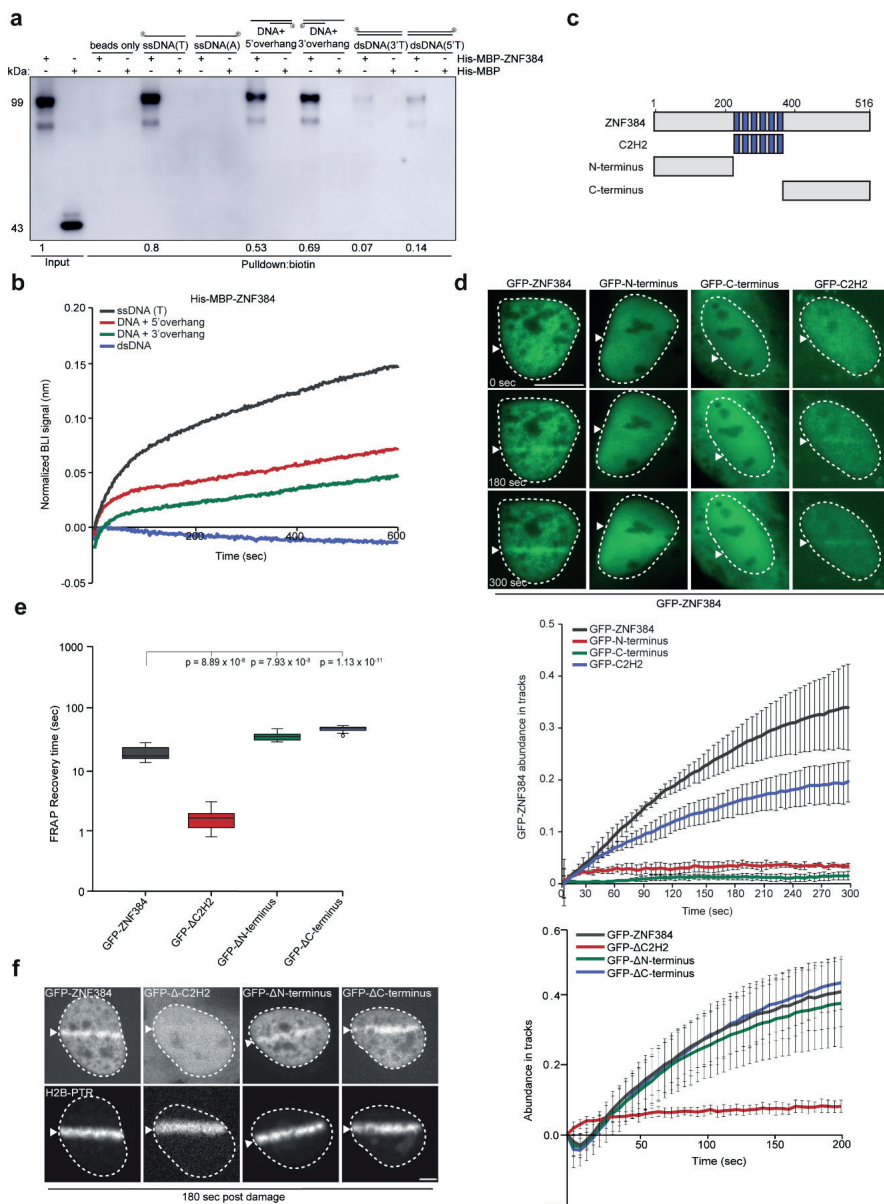


Figure. 3. ZNF384 is recruited to sites of DNA damage via its C2H2 DNA binding motif. (A) DNA pull-downs of the indicated biotinylated DNA substrates in the presence of His-MBP-C2H2 or His-MBP (control). Blots were probed for MBP. His-MBP-ZNF384 pull-down signals were normalized to the Input signal, which was set to 1. The mean from 4 independent experiments is indicated below the blot. His-MBP was not detectable in pull-downs. A representative experiment is

shown. (B) DNA binding of His-MBP-ZNF384 to the indicated biotinylated DNA substrated as measured by BLI. Quantified data is plotted on a time scale and normalized to His-MBP (control). (C) Schematic representation of full-length ZNF384 protein and its domains (C2H2, N-terminus and C-terminus). (D) Live cell imaging of the recruitment of the indicated GFP-ZNF384 proteins to DNA damage tracks generated by 365 nm UV-A tracks in BrdU-sensitized *ZNF384* KO U2OS Flp-In/T-Rex cells. mCherry-NBS1, which was co-expressed with GFP-ZNF384 proteins, served as a DNA damage marker. Representative images are shown. White triangles indicate irradiated regions. Scale bars: 10 μ m (upper panel). Quantification of the data is shown as mean \pm SEM from 30–40 cells (lower panel). (E) Quantification of FRAP measurements to assess the local dynamics of the indicated GFP-ZNF384 constructs. 12 cells per condition were analyzed. Boxplot limits correspond to the 25th and 75th percentiles and the center line in the box indicates the median value. The whiskers extend 1.5 times the interquartile range. P-values were calculated using an unpaired Student's t test, assuming unequal variances. (F) Live cell imaging of the recruitment of the indicated GFP-ZNF384 proteins to DNA damage tracks generated by 405 nm laser micro-irradiation in Hoechst sensitized ZNF384 KO U2OS Flp-In/T-Rex cells. White triangles and photoactivatable H2B-PTR, which was co-expressed with the indicated GFP-ZNF384 proteins, indicate irradiated regions. Representative images are shown Scale bars: 4 μ m (left panel). Data are presented as mean values \pm SEM. P-values were calculated using an unpaired Student's t test, assuming unequal variances (right panel). Source data are provided as a Source Data file.

ZNF384 modulates KU70/KU80 dynamics at DNA damage sites

The repair of DSBs by cNHEJ depends on the binding of the KU70/KU80 heterodimer to broken DNA ends, followed by the recruitment of the DNA-PKcs kinase (Mari, Florea et al. 2006). This in turn leads to the recruitment of the XRCC4-LIG4 complex, which ultimately seals the broken ends (Frit, Ropars et al. 2019). Given the interaction between ZNF384 and KU70/KU80, we sought to address if ZNF384 is involved in the loading of KU70/KU80 at DNA. To this end, we first monitored the levels of KU70 in chromatin-enriched extracts from cells depleted of ZNF384 and KU80 (Supplementary Fig. 8A). While *KU80* knockdown reduced KU70 levels on chromatin, depletion of ZNF384 had no impact (Supplementary Fig. 8A). Next, we monitored the impact of ZNF384 on KU70 dynamics at DNA by FRAP. Within two seconds after photobleaching we observed a small increase in fluorescence recovery of GFP-KU70 in *ZNF384*-depleted cells compared to that in control cells (Supplementary Fig. 8B), suggesting that ZNF384 has a modest effect on KU70's DNA binding. To further investigate this finding, we assessed the DNA binding affinities of both ZNF384 and KU70 by comparing their relative residence times as measured by Fluorescence Correlation Spectroscopy (FCS) (Supplementary Fig. 8C). Interestingly, we observed that ZNF384 has a higher residence time compared to KU70 (Supplementary Fig. 8D), suggesting that ZNF384 is more tightly bound to DNA, thereby impacting the association of KU70/KU80 with DNA.

Based on these findings, we next examined whether ZNF384 has a potential stimulatory role on KU70/KU80's binding to dsDNA with a 3' overhang, a common DSB repair substrate,

in vitro. To this end, we performed DNA-pulldown assays using purified ZNF384 and KU70/KU80. Importantly, while KU70/KU80 bound dsDNA with a 3' overhang in the absence of ZNF384 [31] their binding was enhanced in the presence of increasing amounts of ZNF384 (Fig. 4A and Supplementary Fig. 8E). To examine whether ZNF384 also affects the loading of KU70/KU80 at damaged DNA *in vivo*, we depleted ZNF384 in cells expressing endogenously GFP-tagged KU70 (Britton, Coates et al. 2013), and subjected these cells to multiphoton laser micro-irradiation. Importantly, ZNF384 depletion reduced GFP-KU70 accumulation at sites of DNA damage as compared to that in control cells (Fig. 4B-C). Given that ZNF384 is recruited to DNA breaks in a PAR-dependent manner (Fig. 2A) and regulates the loading of KU70/KU80, we asked whether KU70/KU80 is also recruited to sites of DNA damage in a PAR-dependent manner. Indeed, we found PARPi treatment to impair the recruitment of KU70 to DNA break sites (Supplementary Fig. 8F), while the accumulation of the DNA damage marker NBS1 remained unaffected (Supplementary Fig. 8G-H). To better understand the impact of ZNF384 on the dynamics of KU70, we assessed its turnover at DNA lesions by FRAP (Fig. 4D-E). Within 10 seconds after photobleaching, we observed a faster fluorescence recovery of GFP-KU70 in ZNF384-depleted cells compared to that in control cells (Fig. 4E), suggesting that ZNF384 contributes to the association of KU70 with DNA lesions. To be able to extract quantitative characteristics from the FRAP data, we first tried to fit the recovery curves with single-population models (Sprague, Pego et al. 2004). However, none of them could accurately fit the experimental curves (Supplementary Fig. 9A), indicating that KU displays a more complex behavior. We then examined KU dynamics by FCS as this method is able to assess fast protein turnover more accurately. The fit of the correlation curves showed that KU follows a two-population dynamics at DNA damage sites (Supplementary Fig. 9B). We infer that the fast population refers to KU molecules diffusing through the nucleus and displaying only very transient interactions with chromatin, while the slow population corresponds to KU molecules that bind DNA lesions more stably. To characterize specifically the behavior of this slow population, we restricted the fitting of the FRAP curves to the timepoints after 3 seconds post photobleaching, which could be well adjusted by a reaction-limited model (Supplementary Fig. 9C). Using this model, we were able to estimate binding (k'_{on}) and unbinding (k_{off}) rates of KU at sites of DNA damage by FRAP. The k'_{on} is a pseudo first-order association rate corresponding to the product of the actual binding rate k_{on} and the local density of DNA damage sites dictated by the irradiation conditions, which was similar between the different conditions. To confirm the applicability of this model, we also verified that the k_{off} parameter estimated with this model was independent of the size of the

bleached area (Supplementary Fig. 9D). Based on these fits, we observed a reduction in the k_{on} in ZNF384-depleted cells, suggesting a decreased KU70 binding rate (Fig. 4F). In contrast, no significant impact of ZNF384 depletion on the estimated k_{off} was observed (Fig. 4G). Together these results imply that ZNF384 facilitates the recruitment and subsequent binding, rather than the retention of KU70/KU80, at sites of DNA damage.

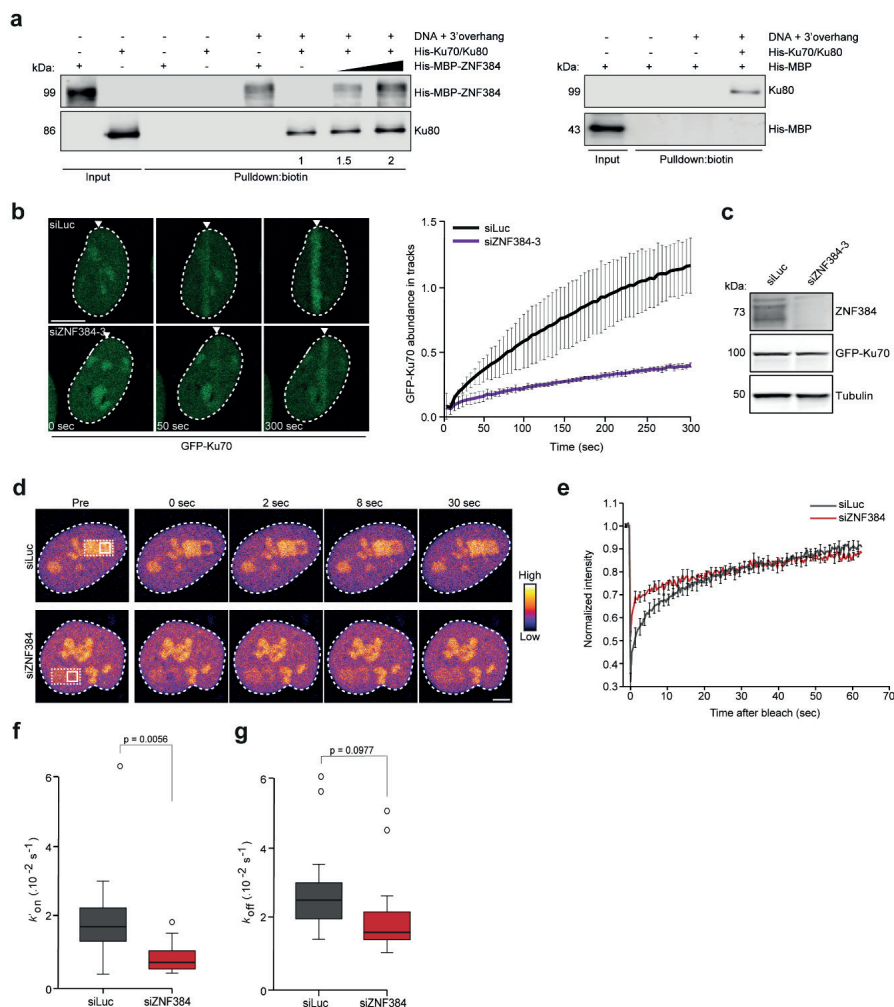


Figure 4. ZNF384 modulates KU70/KU80 dynamics at DNA damage sites. (A) DNA pulldowns of biotinylated DNA with a 3'overhang in the presence of His-KU70/KU80, His-MBP-ZNF384 or His-MBP alone or His-KU70/KU80 in combination with His-MBP-ZNF384 or His-MBP. Blots were probed for MBP and KU80. KU80 pulldown signals were normalized to that in the pulldown lacking His-MBP-ZNF384, which was set to 1. The mean from 4 independent experiments is indicated below the blot. His-MBP was not detectable in pulldowns. (B) GFP-KU70

recruitment to 800 nm multiphoton tracks in RPE1-hTERT cells transfected with the indicated siRNAs (left panel). White triangles indicate irradiated regions. Quantification of the data is presented as the mean \pm SD from >60 cells acquired in 2 independent experiments. Scale bar: 5 μ m (C) Western blot analysis of ZNF384 expression in cells from B. Tubulin is a loading control. Data shown represent 2 independent experiments. (D) Representative images of RPE1-hTERT cells transfected with the indicated siRNAs in which FRAP measurements were performed to assess the local turnover of GFP-KU70 at the sites of DNA damage. DNA damage was induced in the region indicated with a dashed line. Subsequent FRAP was induced in a subarea within the DNA damage region, as indicated with an unbroken line. Images are pseudocolored according to the look-up table displayed on the right. Scale bar: 4 μ m. (E) Normalized FRAP curves from D. (F) Association (k'_{on}) rates of GFP-KU70 measured by FRAP after fitting of the curves from E. (G) Dissociation (k'_{off}) rates of GFP-KU70 after fitting of the curves from E. Data from E-G was collected from 15 cells per condition. Boxplot limits correspond to the 25th and 75th percentiles and the center line in the box indicates the median value from a representative of 2 independent replicates. Statistical significance was calculated using the unpaired Student's *t* test, assuming unequal variances. Source data are provided as a Source Data file.

The C2H2 and N-terminal domains of ZNF384 are critical for loading KU70/KU80 at DSBs

Having shown that ZNF384 promotes the loading of KU70/KU80 at DNA breaks and considering that ZNF384 and KU70/KU80 physically interact, we next sought to investigate whether the interaction between these proteins is important for the efficient recruitment of KU70/KU80 to DNA breaks. We therefore set out to map the region in ZNF384 that is required for the interaction with KU70/KU80, making use of our set of ZNF384 deletion mutants (Supplementary Fig. 7G). Using GFP-pulldown assays we found that GFP-tagged ZNF384, Δ C2H2 ZNF384 and Δ C-terminus ZNF384 associated with endogenous KU70 and KU80 with equal efficiency (Fig. 5A), suggesting that the C2H2 motifs and C-terminus are dispensable for the interaction. On the contrary, Δ N-terminus ZNF384 showed an almost complete loss of KU70/KU80 binding, indicating that the N-terminus of ZNF384 mediates its interaction with KU70 and KU80 (Fig. 5A). In agreement with our *in vivo* pulldown results, we found that recombinant Δ N-terminus ZNF384 bound less efficiently to KU70/KU80 when compared to recombinant ZNF384 (Figure 5B).

We next asked if this domain has any functional relevance for KU70/KU80 recruitment. To this end, we used the Flp-In/T-rex system to establish U2OS cells stably expressing inducible siRNA-resistant GFP-tagged versions of either ZNF384, Δ C2H2 ZNF384 or Δ N-terminus ZNF384. U2OS cells stably expressing GFP-NLS served as a control (Fig. 5C). While expression of GFP-ZNF384 fully restored KU80 accumulation at UV-A laser micro-irradiation inflicted damage, expression of Δ N-terminus ZNF384 only partially rescued this KU80 defect (Fig. 5D). In contrast, expression of Δ C2H2

ZNF384 completely failed to rescue the KU80 accumulation defect (Fig. 5D). DNA damage induction was similar in all conditions based on equal PAR levels in laser tracks (Fig. 5E). These results suggest that the binding of ZNF384 at DNA breaks via its C2H2 motif, as well as the interaction between its N-terminus and KU70/KU80 contribute to efficient KU80 recruitment.

Finally, we asked if ZNF384 is responsible for KU70/KU80 complex formation. To this end, we performed GFP-pulldowns on cells expressing endogenously GFP-tagged KU70 (Britton, Coates et al. 2013) that were depleted for ZNF384 and left untreated or exposed to ionizing radiation (IR). While we observed that GFP-KU70 and endogenous KU80 interact, as expected, loss of ZNF384 did not impact this interaction, neither in untreated nor in IR-exposed cells (Supplementary Fig. 10A). This suggests that ZNF384 is not involved in KU70/KU80 complex formation, but rather the loading of this complex directly at sites of DNA damage.

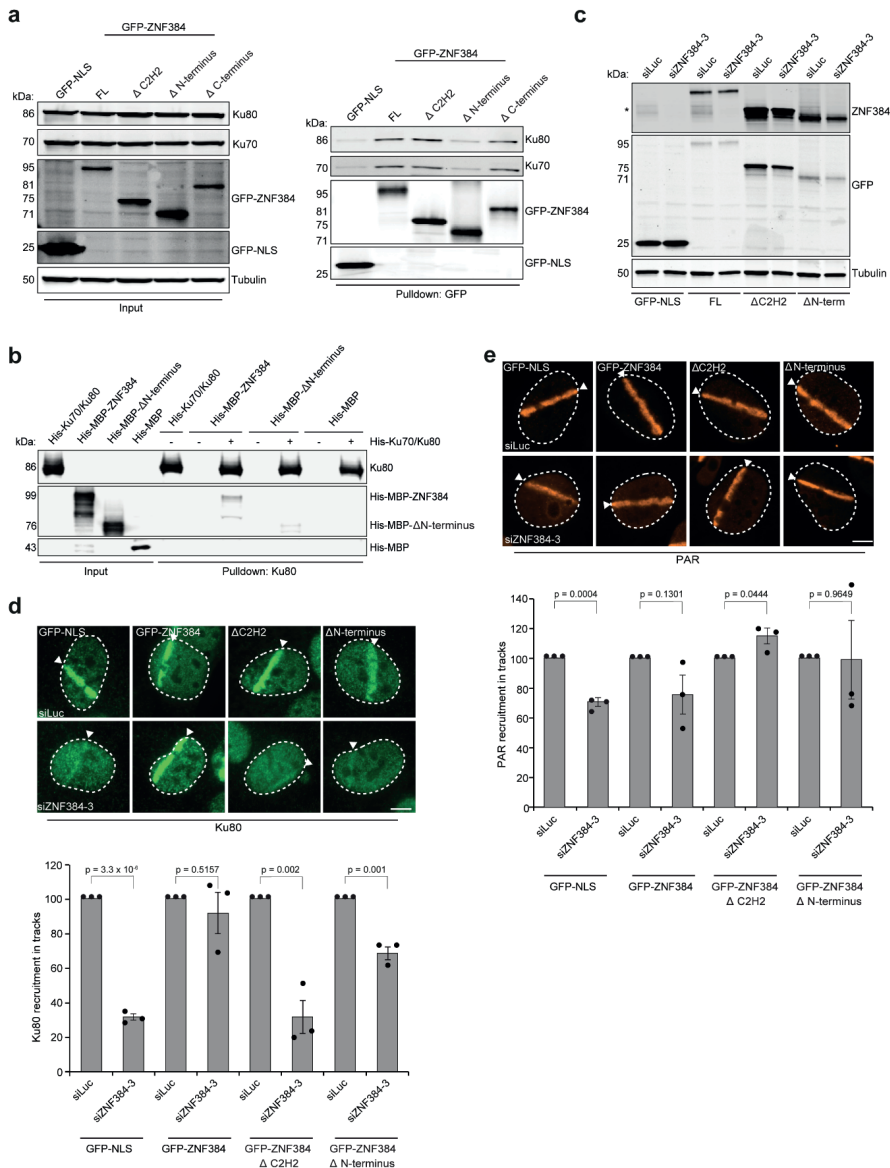


Figure 5. The C2H2 motifs and N-terminus of ZNF384 are required K70/Ku80 loading at DSBs. (A) Pulldowns of the indicated GFP fusion proteins in U2OS Flp-In/T-Rex cells. Blots were probed for Ku70, Ku80, Tubulin and GFP. Data shown represent 3 independent experiments. (B) *In vitro* KU80 pulldown in the presence or absence of His-KU70/KU80 and His-MBP, His-MBP-ZNF384 or His-MBP-ΔN-terminus. Control IP contained beads only. Blots were probed for KU80 and MBP. Data shown represent 2 independent experiments. (C) Western blot analysis of the expression of endogenous ZNF384 and ectopic GFP-ZNF384 full-length and deletion mutants. Tubulin is a loading control. The asterisk (*) indicates endogenous ZNF384. Data shown

represent 3 independent experiments. (D) Accumulation of endogenous KU80 at 365 nm UV-A tracks in BrdU-sensitized U2OS Flp-In/T-Rex cells expressing siRNA-resistant doxycycline (dox)-inducible GFP-ZNF384, GFP-ZNF384 Δ C2H2 and GFP-ZNF384 Δ N-terminus following transfection with the indicated siRNAs. Cells were subjected to laser micro-irradiation and 10 minutes later fixed and immunostained. White triangles indicate irradiated regions (upper panel). Quantification of endogenous Ku80 levels in laser tracks is presented as \pm SEM of >150 cells acquired in 3 independent experiments (lower panel). (E) As in D, except for PAR (upper panel). Quantification of endogenous PAR levels in laser tracks from is presented as the mean \pm SEM from 3 independent experiments. Data were normalized to siLuc, which was set to 100% (lower panel). Statistical significance was calculated using the unpaired Student's *t* test, assuming unequal variances. Scale bar: 5 μ m. Source data are provided as a Source Data file.

ZNF384 promotes KU-dependent loading of APLF and XRCC4/LIG4 at DSBs

Next, we asked if ZNF384 affects the accumulation of factors that act downstream of Ku70/Ku80. We first measured the recruitment of APLF, which physically interacts with Ku80 at DSBs via its conserved Ku-binding motif (KBM) [32]. To this end, YFP-tagged APLF and mCherry-NBS1 were co-expressed in ZNF384-, KU80- and ZNF384/KU80-depleted U2OS cells, and examined for their localization at sites of DNA damage. ZNF384 and KU80 depletion impaired APLF recruitment to sites of DNA damage, while the DNA damage marker NBS1 remained unaffected (Fig. 6A-B and [32]. KU80 depletion also reduced nuclear retention of APLF [33], which we validated in KU80 knockdown cells (Supplementary Fig. 10B-C), as well as in *Ku80*^{-/-} mouse embryonic stem cells (Supplementary Fig. 10D). Interestingly, double knockdown of ZNF384 and KU80 did not further impair APLF accumulation, suggesting that these proteins function epistatically to recruit APLF (Fig. 6A-B).

The fact that ZNF384 promotes the consecutive accumulation of KU70/KU80 and APLF made us wonder if ZNF384 could be involved in Ku-APLF complex formation. To assess this, we performed GFP-pulldowns after transient expression of YFP-APLF in wild-type and ZNF384-depleted U2OS cells. Endogenous KU80 was co-precipitated in both conditions (Supplementary Fig. 10E). Moreover, ZNF384 and Ku70 showed comparable recruitment kinetics (Fig. S10F-G), while APLF was recruited earlier (Supplementary Fig. 10H). This suggests that ZNF384 does not impact Ku-APLF complex stability, but rather promotes the loading of these factors at sites of DNA damage.

The Ku-APLF interaction is critical for recruitment of the XRCC4/LIG4 complex to DNA breaks [3, 32, 34, 35]. Given that ZNF384 promotes both Ku-APLF loading at sites of DNA damage, we next examined if ZNF384 also affects XRCC4 recruitment. To this

end, we measured the levels of endogenous XRCC4 at *bona fide* DSBs induced by tethering of a Lactose repressor (LacR)-tagged FokI nuclease at a stably integrated Lactose operator (LacO) array in U2OS cells [36] (Fig. 6C). While we detected XRCC4 accumulation at FokI-induced DSBs in control cells, as expected, its levels were dramatically reduced in ZNF384-depleted cells (Fig. 6D-E). This indicates that ZNF384 acts at *bona fide* DSBs to facilitate the Ku-APLF-dependent accumulation of XRCC4/LIG4 complexes.

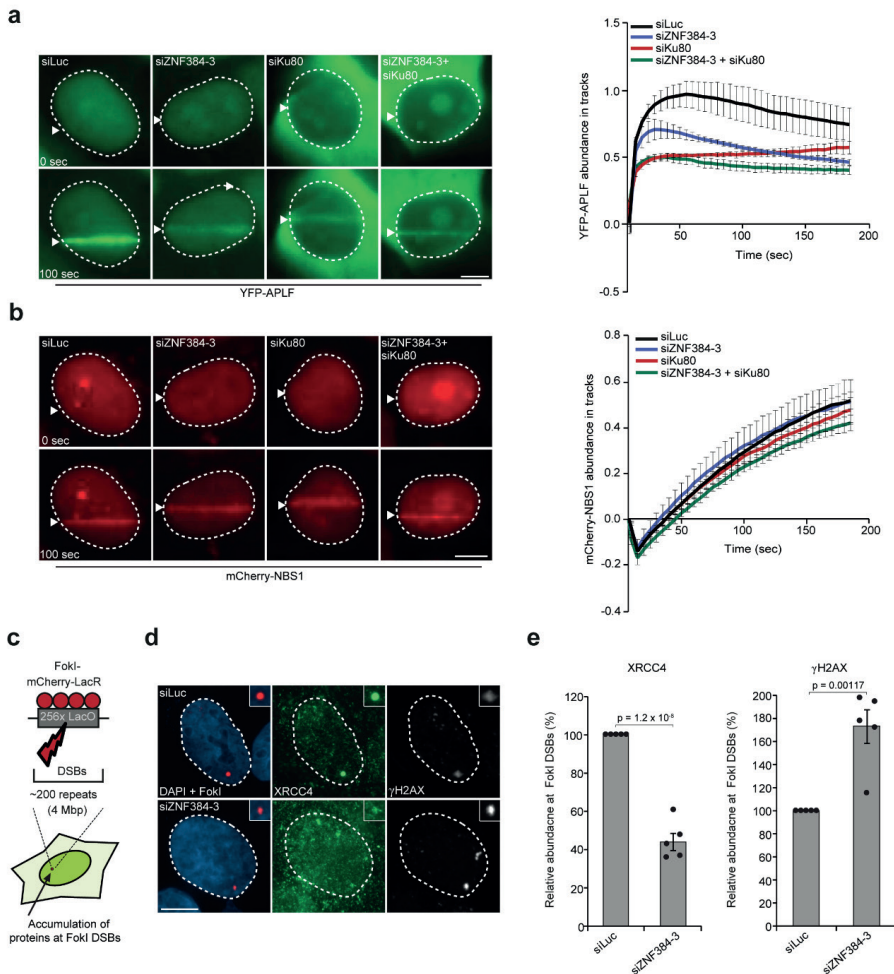


Fig. 6. ZNF384 promotes KU-dependent loading of APLF and XRCC4/LIG4 at DSBs. (A) Live cell imaging of the recruitment of YFP-APLF to 365 nm UV-A tracks in BrdU-sensitized U2OS cells transfected with the indicated siRNAs. mCherry-NBS1, which was co-expressed with YFP-APLF, served as a DNA damage marker. Representative images are shown. White triangles indicate irradiated regions (left panel). Quantification of data is presented as the mean values \pm SEM from 60

cells acquired in 3 independent experiments (right panel). (B) As in A, except for mCherry-NBS1 (left panel). Quantification of data is presented as the mean values \pm SEM from 60 cells acquired in 3 independent experiments (right panel) (C) Schematic of the system in U2OS 2-6-3 cells used to locally induce multiple DSBs upon tethering of the FokI endonuclease. (D) Accumulation of XRCC4 (green) to γ H2AX-marked (white) DSBs induced by FokI-mCherry-LacR at a LacO array (red) in cells transfected with the indicated siRNAs. (E) Quantification of XRCC4 and γ H2AX in cells from D is presented as the mean \pm SEM of >200 cells acquired in 5 independent experiments. Data were normalized to siLuc control which was set to 100%. Statistical significance was calculated using the two-tailed unpaired Student's *t* test, assuming unequal variances. Scale bar: 5 μ m. Source data are provided as a Source Data file.

ZNF384 promotes recruitment of cNHEJ proteins independently of DNA-PKcs

Given that ZNF384 promotes the accumulation of XRCC4/LIG4 in a Ku70/Ku80-dependent manner, we wondered how this is linked to DNA-PKcs, which is recruited and activated by DSB-bound Ku to promote the loading of XRCC4/LIG4 [37, 38]. Western-blot analysis detected an induction of phosphorylated (p)-DNA-PKcs (S2056) after IR (Supplementary Fig. 11A). Surprisingly, neither KU80 nor ZNF384 depletion affected p-DNA-PKcs (S2056) activation in U2OS cells (Supplementary Fig. 11A). Moreover, normal levels of p-DNA-PKcs (S2056) activation were observed in *Ku80*^{-/-} mouse embryonic stem cells, ruling out that the lack of phenotype in KU80-depleted cells was due to incomplete knockdown (Supplementary Fig. 11B and [39]). To corroborate these findings, we examined the interplay between ZNF384, KU and DNA-PKcs during the loading of XRCC4 at sites of DNA damage (Supplementary Fig. 11C). We found that ZNF384, KU80 and DNA-PKcs depletion impaired XRCC4 accumulation (Supplementary Fig. 11D), which is in line with previous results [37, 40]. Double knockdown of ZNF384 and KU80 did not result in an additive effect on XRCC4 accumulation when compared to that in ZNF384- or KU80-depleted cells (Supplementary Fig. 11D-F). This suggest that these proteins act epistatically to recruit XRCC4, which is in line with their epistatic role in recruiting APLF to DNA breaks (Fig. 6A-B). In contrast, double knockdown of ZNF384 and DNA-PKcs resulted in a larger effect on XRCC4 accumulation when compared to that of ZNF384 or DNA-PKcs depletion alone (Supplementary Fig. 11C-E), suggesting redundant functions for these proteins in XRCC4 recruitment.

Given that ZNF384 and Ku were recruited to sites of DNA damage via PAR-driven processes (Fig. 2A and Supplementary Fig. 8F), and that ZNF384 and DNA-PKcs function redundantly, we next asked whether DNA-PKcs is also recruited to DNA breaks in a PAR dependent manner. Indeed, PARPi treatment impaired the recruitment of

DNA-PKcs (Supplementary Fig. 11G), while the accumulation of the DNA damage marker NBS1 remained unaffected (Supplementary Fig. 11H-I). To further understand the interplay between ZNF384, KU and DNA-PKcs with PARP1 epistasis analysis were performed. We found that ZNF384, DNA-PKcs and PARP1 depletion impaired XRCC4 accumulation, which is in line with our previous results (Supplementary Fig. 12A-B and [9]). However, double knockdown of either ZNF384 or DNA-PKcs with PARP1 did not result in an additive effect on XRCC4 accumulation (Supplementary Fig. 12C-D). Together these results suggest that PARP activity drives two parallel pathways for DSB repair by NHEJ, one of which relies on the ZNF384-mediated ligation of broken ends via KU-APLF-XRCC4, the other on DNA-PKcs-XRCC4.

ZNF384 promotes DSB repair via cNHEJ

The interaction of ZNF384 with cNHEJ factors (Fig. 1D), its PARP/PAR-dependent recruitment (Fig. 2A), as well as its ability to load Ku (Fig. 4B), APLF (Fig. 6A) and XRCC4/LIG4 (Fig. 6E) at DSBs, encouraged us to assess whether ZNF384 supports DSB repair via NHEJ. To this end, we first used the well-established EJ5-GFP reporter assay, which relies on the restoration of GFP expression following repair of *I-SceI* endonuclease-induced DSBs that flank a puromycin gene that separates a GFP gene from a CMV promoter (Fig. 7A). Flow cytometric analysis of GFP fluorescence revealed that NHEJ was reduced following ZNF384 knockdown, which was comparable to the effect observed upon XRCC4 knockdown (Fig. 7A). Cell cycle profiles remained unaffected in these cells, ruling out effects of cell cycle mis-regulation (Supplementary Fig. 13A-B). Importantly, knockdown of ZNF384 did not affect the steady-state levels of several factors involved in NHEJ (Supplementary Fig. 13C), albeit that the expression of XRCC4 was slightly reduced (Supplementary Fig. 13C). However, a semi-quantitative analysis revealed that this effect was not consistent, neither in U2OS (Supplementary Fig. 13D) nor in HeLa Flp-In cells (Supplementary Fig. 13E), suggesting that indirect effects due to transcriptional misregulation are unlikely. Furthermore, ZNF384 depletion did not have a major impact on the steady state levels of the checkpoint kinases ATM and CHK1 (Supplementary Fig. 13F-H), nor affected the IR-induced phosphorylation of ATM (at S1981) and CHK1 (at S345) (Supplementary Fig. 13I-J), the latter of which was used as a readout for ATR activation [41]. This suggest that ZNF384 does not contribute to DSB repair by regulating ATM or ATR activation.

The EJ5-GFP reporter provides a readout for total NHEJ activity, including both cNHEJ and aNHEJ [42]. To address if ZNF384 specifically plays a role in KU70/80-, APLF- and XRCC4/LIG4-dependent cNHEJ, we measured random plasmid integration into the genome via cNHEJ (Fig. 7B and [9, 43]). Indeed, ZNF384 knockdown, similar to that of KU80 depletion, impaired random plasmid integration, indicating an important role for ZNF384 in cNHEJ (Fig. 7B).

Next, we asked whether ZNF384 plays a unique role in cNHEJ or also affects HR. Interestingly, loss of ZNF384 only very moderately impaired HR in the well-established DR-GFP reporter (Supplementary Fig. 14A), and rendered cells only mildly sensitive to treatment with PARPi (Supplementary Fig. 14B-C), in contrast to HR-deficient cells depleted of BRCA1 [44]. Given that ZNF384 is critical for KU70/KU80 loading at DSBs and loss of KU70/KU80 has been linked to increased DNA end resection and HR levels [45, 46], we assessed whether ZNF384 affects DNA end resection. Cells depleted of ZNF384 did not show a significant difference in RPA foci number and foci intensity (Supplementary Fig. 14D-G), which is consistent with the fact that ZNF384 loss did not impact HR (Supplementary Fig. 14A). KU80-depleted cells also did not show changes in DNA end resection (Supplementary Fig. 14D-G), which is in agreement with another report showing that end-resection remained unaffected in *Ku70/Ku80* double KO MEF cells [47]. Corroborating these findings, we observed that the accumulation of the core HR protein RAD51 into DSB-containing foci induced by IR was not affected in ZNF384-depleted S-phase cells (Supplementary Fig. 14H). Together these results suggest that ZNF384 does not play a major role in DSB repair via HR, but rather promotes cNHEJ.

When cNHEJ is compromised, DSB repair mostly occurs via aNHEJ, causing a loss of accurate end-joining and a switch to error-prone repair due to deletion formation and microhomology usage [48]. To test whether impaired cNHEJ in ZNF384-depleted cells impacts the mutational signature at repair junctions, we used a previously published NHEJ reporter in GC92 cells [49]. This reporter consists of a CD4 gene separated from a CMV promoter by an H2Kd-CD8 cassette that is flanked by *I-SceI* cleavage sites. DSB induction by *I-SceI* expression leads to re-ligation of the CMV promoter to the CD4 gene after which repair junctions can be amplified and Sanger-sequenced (Supplementary Fig. 15A). Indeed, depletion of the cNHEJ factor KU80 resulted in an increase in the formation of larger deletions and usage of larger stretches of microhomology (Supplementary Fig. 15B-C). Moreover, although ZNF384 depletion only caused a modest effect on the total deletion frequency, among these events the proportion of larger deletions and use of

microhomology during repair was increased and resembled that observed after KU80 depletion (Supplementary Fig. 15B-C), corroborating a role for ZNF384 in cNHEJ.

In further support of these findings, we found that ZNF384 loss impaired clonogenic survival of U2OS cells and VH10-SV40-immortalized fibroblasts following exposure to IR-induced DSBs similar to that observed after XRCC4 depletion (Fig. 7C-D and Supplementary Fig. 15D-E). Interestingly, double depletion of ZNF384 and XRCC4 did not result in an increased sensitivity to IR (Fig. 7C-D), again indicating that these proteins function epistatically to promote cNHEJ-dependent repair DSBs. Finally, we employed the Flp-In/T-Rex system to establish HeLa cells stably expressing inducible siRNA-resistant GFP-tagged ZNF384 or GFP-NLS (Fig. 7E). We found that expression of siRNA-resistant GFP-ZNF384, but not that of GFP-NLS, almost fully rescued the IR-sensitivity observed after ZNF384 loss, the latter of which being comparable to that observed after XRCC4 loss (Fig. 7F). This indicates that the IR sensitivity and underlying cNHEJ defect are not caused by off-targets of the siRNAs against ZNF384. The increase in IR sensitivity likely resulted from an accumulation of unresolved DSBs, as indicated by the increase in γ H2AX foci following IR-exposure of ZNF384-depleted G1 cells, which resembled the phenotype of KU80-depleted cells (Supplementary Fig. 15F-H and [50]). Interestingly, KU80 has been implicated in telomere length maintenance (Jaco, Muñoz et al. 2004). To study whether ZNF384 is similarly involved in this process, we performed Fluorescence *in situ* hybridization (FISH) using a PNA probe to label all telomeres and use their intensity as a proxy for telomere length (Fig. 7G) [51]. Strikingly, knockdown of ZNF384, similar to that of KU80 [52], significantly reduced telomere length in metaphase spreads when compared to that in control cells (Fig. 7H-I). Collectively, our results demonstrate that ZNF384 promotes efficient DSB repair via cNHEJ and is involved in telomere length maintenance (Fig. 7J).

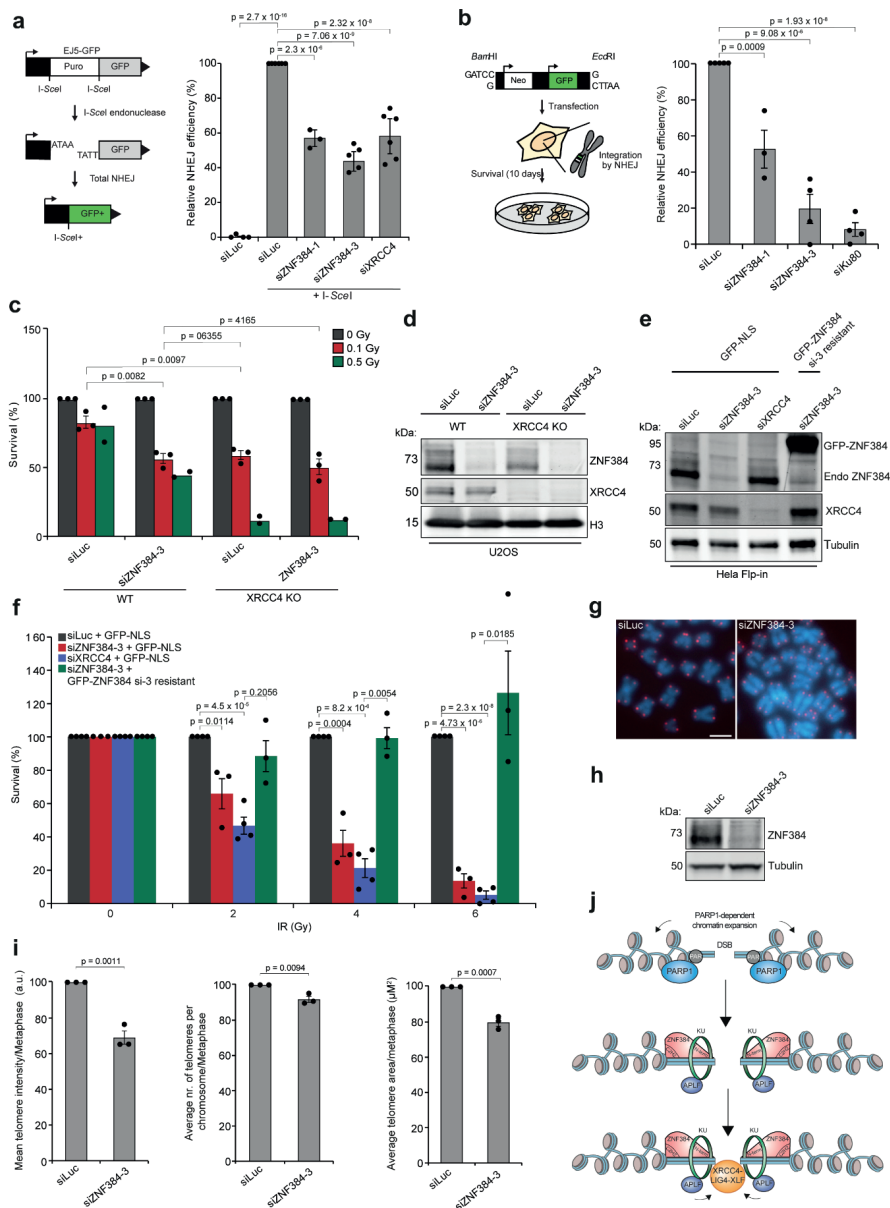


Fig. 7. ZNF384 promotes DSB repair via cNHEJ. (A) Schematic of the EJ5-GFP reporter for NHEJ (left panel). Quantification of the EJ5-GFP-positive U2OS cells transfected with the indicated siRNAs and I-SceI expression vector. I-SceI transfection was corrected by co-transfection with mCherry expression vector. The mean \pm SEM of 3-5 independent experiments is shown (right panel). Data was normalized to the siLuc control which was set to 100%. (B) Schematic of the random plasmid integration assay (left panel). Quantification of plasmid integration efficiencies in

U2OS cells transfected with the indicated siRNAs (right panel). The mean \pm SEM of 3-6 independent experiments is shown. Data were normalized to siLuc control which was set to 100%. (C) Relative survival efficiency in WT and XRCC4 KO U2OS cells transfected with the indicated siRNAs and exposed to the indicated doses of IR. The mean \pm SEM of 2-3 independent experiments is shown. Data were normalized to un-irradiated conditions and set to 100%. (D) Western blot analysis of the expression of endogenous ZNF384 from cells in C. Tubulin is a loading control. (E) Expression levels of endogenous ZNF384 and dox-inducible siRNA-resistant GFP-ZNF384 in Hela Flp-In/TRex cells. Tubulin is a loading control. (F) Effect of inducible expression of GFP-NLS and siRNA resistant GFP-tagged ZNF384 on the survival of stable Hela Flp-In/TRex after transfection with indicated siRNAs and IR treatment. The mean \pm SEM of 3-4 independent experiments is shown. Data was normalized to siLuc control which was set to 100%. (G) Representative FISH images of metaphases from HCT116 cells transfected with the indicated siRNAs. Scale bar: 5 μ m (H) Western blot analysis of the expression of endogenous ZNF384 from cells in G. Tubulin is a loading control. (I) Quantifications per metaphase from H are presented as the mean \pm SEM of 75 chromosomes acquired in 3 independent experiments. Data were normalized to siLuc control, which was set to 100%. (J) Model for how ZNF384 works as an adaptor of KU to DNA during DSB repair by cNHEJ (see text for details). Source data are provided as a Source Data file. All P-values were calculated using the two-tailed unpaired Student's *t* test, assuming unequal variances.

DISCUSSION

In this study, we uncover an important role of the poorly characterized ZnF protein ZNF384 in DSB repair via cNHEJ (Fig. 7J). First, we demonstrate that ZNF384 is recruited to sites of DNA damage and interacts with KU70/KU80 and PARP1. Second, we show that ZNF384 recruitment requires PARP1/PAR-dependent chromatin remodeling, which promotes binding of ZNF384 to the exposed DNA via its C2H2 motifs. Third, ZNF384 stimulates the binding of KU70/KU80 at DNA breaks, on the one hand through physical interaction with this complex, and on the other hand through its affinity for DNA. This way, it promotes the assembly of a functional cNHEJ complex that includes APLF and the XRCC4/LIG4 complex. Finally, ZNF384 promotes NHEJ in EJ5-GFP reporter assays and random plasmid integration assays, and functions epistatically with both Ku and XRCC4 during this repair process. Thus, ZNF384 functions as an 'adaptor station' for the proper assembly of repair proteins at DSBs, thereby promoting efficient repair by cNHEJ (Fig. 7J).

PARP1/PAR-dependent chromatin unfolding allows ZNF384 binding to damaged DNA

Our findings reveal that ZNF384 is recruited to sites of DNA damage following chromatin unfolding driven by the activity of PARP1, but not PARP2 or PARP3. Several other cNHEJ repair proteins, including KU70/KU80 and XRCC4, are also recruited in a manner dependent on the activity of PARP1. This may involve their binding to PARP1-associated PAR chains or to the damaged DNA itself [9, 53]. Using three independent

approaches we confirmed that ZNF384 does not bind to PARP1-associated PAR chains at sites of DNA damage. Instead ZNF384 recruitment occurs in a manner dependent on the PARP1-induced relaxation of the damaged chromatin, making the DNA available for ZNF384 to bind via its C2H2 DNA binding motif. This is consistent with other reports showing that ZNF384 directly binds to DNA, particularly to homopolymeric dA:dT consensus sequences *in vitro* [30, 54]. We confirmed and extended this finding by showing that ZNF384, through its C2H2 domain, also efficiently binds dsDNA substrates containing 5' or 3' overhangs as opposed to dsDNA with blunt ends. DSBs with such protruding ends have been shown to be preferentially repaired by cNHEJ, while blunt ends are mostly subjected to polymerase theta-mediated end-joining [39]. Thus, the preferential binding of ZNF384 to dsDNA with 5' or 3' overhangs is consistent with its role in cNHEJ. However, it is important to note that the DNA substrates used in our study also contain T-rich consensus sequences. These sequences are considered the most abundant simple repetitive motifs in the human genome that are frequently expanded due to DNA replication slippage [55]. The fact that DSBs can occur throughout the genome, including at homopolymeric dA:dT repeats, raises the question whether the C2H2 DNA binding domain of ZNF384 binds to a specific DNA context or binds to lesions in any given sequence context, the latter of which would be in line with a more general role of ZNF384 in cNHEJ. Elucidating the nature of its DNA sequence-specific binding mode will be key in further unraveling how ZNF384 acts at DSBs to promote cNHEJ

ZNF384 serves as a 'KU-adapter' at sites of DNA damage

ZNF384 promotes the accumulation of KU70/KU80, but not their retention at sites of damage. This raises the question as to how the recruitment of these proteins is regulated at the level of DNA binding. FCS analysis revealed that ZNF384 had a significantly higher residence time compared to KU70, suggesting that ZNF384 binds stronger to DNA as compared to KU70. Moreover, ZNF384 stimulates the binding of KU70/KU80 on DNA *in vitro*, suggesting that ZNF384 is the dominant binding force within the ZNF384-KU complex, in which it serves as a platform that assists in the positioning of KU70/KU80 on DNA. Indeed, we identified two regions in ZNF384 that contribute to KU70/KU80 recruitment at sites of DNA damage: the N-terminus, which mediates the interaction with KU70/KU80, and the internal C2H2 motifs, which ensure DNA binding. The region in KU70/KU80 that is responsible for the KU-ZNF384 interaction, as well as its relevance for cNHEJ, remain to be established. Collectively, these findings

suggest that ZNF384 may act as a 'KU-adaptor' that 1) senses DNA damage, 2) binds to DNA upon PARP/PAR-induced chromatin relaxation, and 3) guides KU70/KU80 for efficient loading at DNA breaks. To further support this model, which suggests a co-operative mode of action between ZNF384 and KU70/KU80, future studies may focus on understanding the spatio-temporal dynamics of these proteins at individual DSBs.

ZNF384 and DNA-PKcs act redundantly during cNHEJ protein assembly

How does ZNF384 promote the proper KU-dependent build-up of downstream NHEJ proteins at sites of DNA damage? ZNF384 and KU80 act epistatically to promote APLF recruitment to sites of DNA damage. Moreover, a direct interaction between APLF and KU's conserved KBM region has previously been shown to promote XRCC4 recruitment [32]. Our data reveal that ZNF384 is not implicated in KU-APLF complex formation, instead suggesting that ZNF384 loads XRCC4 at DSBs by promoting the recruitment of KU70/KU80 and thereby also APLF. Although our mass spectrometry analysis for ZNF384 -interacting proteins did not detect APLF, we cannot exclude the possibility that physical interactions between these proteins also contributes to XRCC4/LIG4-dependent cNHEJ.

Previous work suggested that XRCC4/LIG4 assembly also depends on the recruitment and activation of DNA-PKcs by KU-bound DNA ends [56]. However, DNA-PKcs activity remained unaffected in ZNF384- or KU80-depleted human cells, as well as in *Ku80^{-/-}* mouse embryonic stem cells. This raises the question whether ZNF384 and KU70/KU80 promote XRCC4/LIG4 accumulation independently of DNA-PKcs. Our epistasis analysis suggests that ZNF384 cooperates with KU70/KU80, but functions independently of DNA-PKcs to promote XRCC4 accumulation at DNA breaks. This is in line with a recent report showing that KU and XRCC4/LIG4 are sufficient for DNA end synapsis independently of DNA-PKcs *in vitro* [57]. Furthermore, it may be possible that APLF dictates the functional redundancy between ZNF384 and DNA-PKcs, as APLF is recruited to sites of DNA damage via KU, PARP3 [34, 35], and ZNF384 to promote the loading of XRCC4. Finally, DNA-PKcs has been reported to have additional roles beyond NHEJ such as during mitosis, in which DNA-PKcs autophosphorylation appears to be largely independent of KU [58, 59]. This suggests the existence of KU and DNA-PKcs independent mechanisms and may explain the redundancy of ZNF384 and DNA-PKcs during cNHEJ. Future work may not only provide more insight into how

ZNF384 functions independently of DNA-PKcs during the assembly of a functional cNHEJ repairosome, but would also help to deepen our understanding of how DNA-PKcs function is linked to cNHEJ driven by ZNF384-KU70/KU80.

ZNF384 and other ZnF proteins in cNHEJ

We reveal a critical role for ZNF384 in stimulating efficient cNHEJ in human cells. However, ZNF384 is not the only ZnF protein involved in cNHEJ. For instance, APLF and ZBTB24 possess distinct ZnF domains (PBZ in APLF and C2H2 in ZBTB24) that are required for the build-up of a functional NHEJ complex by binding to auto-mono(ADP-ribosyl)ated (MAR) PARP3, PARylated PARP1, or DNA, respectively, at DSBs [18, 32, 60]. This suggests that the versatile substrate recognition ability by distinct domains in ZnF proteins may play an important role in the cNHEJ process. To this end, it is interesting to note that several other ZnF proteins are recruited to sites of DNA damage in a PAR-dependent manner [12]. Although it remains to be established whether this involves direct PAR-binding or binding to damaged DNA, these findings suggest that ZnF proteins may play a more important role in DNA repair than previously anticipated. Future mechanistic studies will undoubtedly improve our understanding of their crucial role in diverse biological process, including DNA damage repair, thereby increasing our understanding of genome stability maintenance.

METHODS

Cell lines

U2OS, HeLa, VH10-SV40 and SV40 T-transformed GM639 human fibroblasts cells were cultured in 5% CO₂ at 37°C in DMEM (Dulbecco's modified Eagle's medium), and DMEM and DMEM F-12 (Ham) supplemented with 10% fetal calf serum and antibiotics. RPE1-hTERT cells expressing endogenous GFP-Ku70 were a gift from Steve Jackson [61]. U2OS cells with stably integrated EJ5-GFP or DR-GFP reporters were a gift from Jeremy Stark and Maria Jasin [42, 62]. SV40 large T-transformed GM639 human fibroblasts with a stably integrated GC92 reporter were a gift from Bernard Lopez [49]. U2OS cells stably expressing cell cycle marker mKO-Cdt1 were previously generated [9]. U2OS *AsiSI*-ER- cells were a gift from Gaelle Legube [63]. U2OS 2-6-5 cells stably expressing ER-mCherry-LacR-FokI-DD were a gift from Roger Greenberg [36]. HeLa and stable GFP-Ku80 expressing HeLa cells were a gift from Dik van Gent (Erasmus Medical Center, Rotterdam, the Netherlands). 129/Ola-derived IB10 mouse

embryonic stem cells WT and Ku80^{-/-} were a kind gift from Marcel Tijsterman [39]. PARP1, PARP2 and PARP1/PARP2 knockout U2OS cells were a kind gift from Nicholas Lakin [64]. XRCC4 knockout U2OS cells were generated by co-transfection of pKLV-U6gRNA-EF(BbsI)-PGKpuro2ABFP (Addgene) containing XRCC4 gRNA (5'-GATGACATGGCAATGGAAA-3') with pSpCas9(BB)-2A-GFP (PX458) containing Cas9 (Addgene). ZNF384 knockout U2OS Flp-In/T-rex cells were generated by co-transfection of pKLV-U6gRNA-EF(BbsI)-PGKpuro2ABFP (Addgene) containing ZNF384 gRNA (5'-CCACCTCTGAGAACAGGAGACTC-3') with pSpCas9(BB)-2A-GFP (PX458) containing Cas9 (Addgene). HeLa Flp-In/T-Rex and U2OS Flp-In/T-Rex cells, which were generated using the Flp-In/T-REx system (Thermo Fisher Scientific), were a gift of Geert Kops (University Medical Center Utrecht, the Netherlands) and Stephen Taylor (University of Manchester, UK). These cells were used to stably express inducible versions of GFP-NLS and GFP-APLF as well as siRNA-resistant GFP-ZNF384^{WT}, GFP-ZNF384^{ΔN-terminus(1-209)}, GFP-ZNF384^{ΔC2H2(205-410)}, GFP-ZNF384^{ΔC-terminus(401-516)} by co-transfection of pCDNA5/FRT/TO-Puro plasmid encoding GFP or GFP-tagged ZNF384 (WT or deletion mutants) (5 μg), together with pOG44 plasmid encoding the Flp recombinase (1 μg). After selection on 1 μg/mL puromycin, single clones were isolated and expanded. Both HeLa Flp-In/T-REx clones and U2OS Flp-In/T-Rex were incubated with 2 μg/mL doxycycline for 24h to induce expression of cDNAs. All cells were authenticated by STR profiling and tested negative in routinely performed mycoplasma tests.

Chemicals

Cells were treated with Phleomycin (InvivoGen) at the indicated concentrations for 1 hour and collected for further analysis. The PARP inhibitor olaparib (Selleck Chemicals) and DNA-PK inhibitor NU-7441 (Selleck Chemicals) were both used at a final concentration of 10 μM, whereas PARGi (PDD00017273, Sigma) inhibitor was used at a concentration of 25 mM. H₂O₂ was used at a concentration of 0.5 mM.

Transfections, siRNAs and plasmids

Cells were transfected with siRNAs using RNAiMAX (Invitrogen) according to the manufacturer's instructions. Cells were transfected twice with siRNAs at 0 and 24 hours at a concentration of 40 nM and analyzed 48 hours after the second transfection unless otherwise indicated. siRNA sequences are listed in Supplementary Table 2. Cells

were transfected with plasmid DNA using Lipofectamine 2000 (Invitrogen) according to the manufacturer's instructions and analyzed 24-48 hours after transfection. The expression vector for full length human ZNF384 (pCDNA3.1-FLAG-ZNF384-WT, isoform 2 with 6 C2H2 motifs), which was a gift from Myriam Alcalay (Bajpai, Chen et al. 2010), was amplified and cloned into pCDNA5/FRT/TO-Puro as a *HindIII/KpnI* fragment (Supplementary Table 3). Deletion constructs were generated by site-directed mutagenesis PCR (Supplementary Table 3). siZNF384-3-resistant ZNF384 cDNA was generated by introducing the underlined mutations CGACAGCATAATAAGGACAAG by overlap PCR and cloned as *HindIII/KpnI* fragment into pCDNA5/FRT/TO-Puro-ZNF384-WT (Supplementary Table 2). All ZNF384 expression constructs were verified using Sanger sequencing. All other plasmids were described previously: pmCherry-PARP1 [65], pmEGFP-macroH2A1.1 macrodomain [11], GFP-WWE (from RNF146) [8], H2B-PTR, GFP-BZIP [11], GFP-CHD4 and YFP-APLF [66].

Generation of DSBs by ionizing radiation (IR)

IR was delivered to cells by an YXlon X-ray generator machine (200 KV, 4 mA, dose rate 1 Gy/minute) or a Faxitron Cabinet X-ray System Model RX-650 (130 kVp, dose rate 1.85 Gy/minute).

365 nm UV-A laser micro-irradiation

Cells were grown on 18 mm coverslips and sensitized with 10 μ M 5'-bromo-2-deoxyuridine (BrdU) for 24 hours as described [9]. For micro-irradiation, the cells were placed in a ChamSlide TC-A live-cell imaging chamber that was mounted on the stage of a Leica DM IRBE widefield microscope stand (Leica) integrated with a pulsed nitrogen laser (Micropoint Ablation Laser System; Andor). The pulsed nitrogen laser (16 Hz, 364 nm) was directly coupled to the epifluorescence path of the microscope and focused through a Leica 40x HCX PLAN APO 1.25–0.75 oil-immersion objective. The growth medium was replaced by CO₂-independent Leibovitz's L15 medium supplemented with 10% FCS and cells were kept at 37°C. The laser output power was set to 72-80 to generate strictly localized sub-nuclear DNA damage. Cells were micro-irradiated (two iterations per pixel) within 5 minutes using Andor IQ software (version 3.6). Following micro-irradiation, cells were incubated for the indicated time points at 37°C in Leibovitz's L15 and subsequently fixed with 4% formaldehyde before immunostaining. Images of fixed samples were acquired on a Zeiss AxioImager M2 or D2 widefield fluorescence

microscope equipped with 40x, 63x and 100x PLAN APO (1.4 NA) oil-immersion objectives (Zeiss), an HXP 120 metal-halide lamp used for excitation and the following filters: DAPI (excitation filter: 350/50 nm, dichroic mirror: 400 nm, emission filter: 460/50 nm), GFP/Alexa 488 (excitation filter: 470/40 nm, dichroic mirror: 495 nm, emission filter: 525/50 nm), mCherry (excitation filter: 560/40 nm, dichroic mirror: 585 nm, emission filter: 630/75 nm), Alexa 555 (excitation filter: 545/25 nm, dichroic mirror: 565 nm, emission filter: 605/70 nm), Alexa 647 (excitation filter: 640/30 nm, dichroic mirror: 660 nm, emission filter: 690/50 nm). Images were recorded using ZEN 2012 software (blue edition, version 1.1.0.0) and analyzed in Image J (version 1.48) as described previously (Luijsterburg, de Krijger et al. 2016). Briefly, the average pixel intensity of laser tracks was measured within the locally irradiated area (Idamage), in the nucleoplasm outside the locally irradiated area (Inucleoplasm), and in a region not containing cells in the same field of view (Ibackground). The level of protein accumulation relative to the protein level in the nucleoplasm was calculated as follows: $((Idamage - Ibackground)/(Inucleoplasm - Ibackground) - 1)$.

405 nm laser micro-irradiation

Laser micro-irradiation for local photoactivation and DNA damage induction at 405 nm was performed using a single-point scanning head (iLas2 from Roper Scientific) coupled to the epifluorescence backboard of a Nikon Ti-E inverted microscope equipped with a spinning-disk scan head CSU-X1 from Yokogawa at a rotation speed of 5000 rpm, a Plan APO 60x/1.4 N.A oil-immersion objective lens and a sCMOS ORCA Flash 4.0 camera. The fluorescence of EGFP and mCherry/activated PATagRFP were excited with lasers at 490 nm and 561 nm, respectively. Bandpass filters adapted to the fluorophore emission spectra were used for fluorescence detection. Images were acquired using Metamorph software (version 7.8.2.0). Cells were sensitized with media containing 0.3 μ g/mL Hoechst 33342 for 1 hour at 37°C. Prior to imaging, the medium was replaced with CO₂-independent phenol red-free Leibovitz's L15 medium (Life Technologies) supplemented with 20% FCS. Cells were irradiated with a 16 μ m line through the nucleus to simultaneously induce DNA damage and photoactivate PATagRFP. The 405 nm laser power was measured at the beginning of each experiment and set to 125 μ W at the sample level to ensure reproducibility. For PAR-3H experiments and ZNF384 recruitment experiments, images were collected every 5 seconds for 10 minutes. For ZNF384 and WWE recruitment with late PARP inhibitor treatment, Z-stacks (1

μm steps) of irradiated nuclei were collected every 30 seconds for 15 minutes. Image collection was paused 3 minutes post damage and olaparib was added to the imaging media to a final concentration of 30 μM . For protein recruitment analysis, a custom-made MATLAB (MathWorks) program R2014b (version 8.4.0.150421) (available upon request). For reviewing purposes the following link can be used: <https://github.com/sehuet/Singh-image-processing> was used to segment the site of damage (I_d) as determined by the photoactivated H2B area, the total nuclear fluorescence (I_{nd}), and an area of background outside of the cell (I_{bg}). Protein accumulation at sites of damage (A_d) was calculated as:

$$A_d = \frac{I_d - I_{bg}}{I_n - I_{bg}} \quad (1)$$

The intensity within the micro-irradiated area was then normalized to the intensity prior to damage induction. Chromatin relaxation was determined by measuring the change in thickness of the photoconverted H2B line [8].

Multiphoton laser micro-irradiation

Cells grown were grown on 18 mm coverslips. For micro-irradiation, cells were placed in a Chamlyde CMB magnetic chamber and the growth medium was replaced by CO_2 -independent Leibovitz's L15 medium supplemented with 10% FCS and antibiotics. Laser micro-irradiation was performed on a Leica SP5 confocal microscope equipped with an environmental chamber set to 37°C. DNA damage-containing tracks (1.5 μm width) were generated with a Mira mode locked titanium-sapphire (Ti:Sapphire) laser ($\lambda = 800$ nm, pulse length = 200 fs, repetition rate = 76 MHz, output power = 80 mW) using a UV-transmitting 63x 1.4 NA oil immersion objective (HCX PL APO; Leica). Confocal images were recorded before and after laser irradiation at 5 seconds time interval over a period of 3-5 minutes. Images after multi-photon micro-irradiation of living cells were recorded using LAS-AF software (Leica, light version 1.0.0) and analyzed with Image J (version 1.48) as described previously [9]. The average pixel intensity of laser tracks was measured within the locally irradiated area (I_{damage}), in the nucleoplasm outside the locally irradiated area ($I_{\text{nucleoplasm}}$) and in a region not containing cells in the same field of view ($I_{\text{background}}$). The level of protein accumulation relative to the protein level in the nucleoplasm was calculated as follows: $((I_{\text{damage}} - I_{\text{background}})/(I_{\text{nucleoplasm}} - I_{\text{background}}) - 1)$.

Ultra-soft X-ray irradiation and imaging

The U2OS Flp-In/T-Rex cells stably expressing inducible GFP-tagged ZNF384 were incubated with doxycycline (2 μ M) for 2.5 hours before being irradiated using the previously described ultra-soft X-ray system [19]. To obtain locally concentrated DSBs, a custom-designed irradiation mask with parallel apertures (2.5 μ m wide) was placed between the bottom of the cell culture dishes and the X-ray source. Cells were irradiated for 10 seconds at 40 mA emission current and 6 KeV acceleration voltage, resulting in approximately 1,000 DSBs per irradiated area. Images of cells and of the irradiation mask were collected five minutes after exposure. For experiments involving immunofluorescence imaging, cells were exposed as described above, without doxycycline preincubation. Five minutes after irradiation, cells were fixed and immunostained. Wide-field 3D images were acquired using a Leica DMI8 microscope (63x/1.4 NA) and deconvolved using Huygens Professional (version 19.10). Confocal images of immunostained cells were captured using a Leica SP8-X SMD (63x/1.4 NA).

Proximity Ligation Assay (PLA)

U2OS AsiSI-ER cells were seeded on 12-mm coverslips and after 24 hours treated with 1 μ M 4-Hydroxytamoxifen (4-OHT, Sigma) for 5h to induce DSBs. Subsequently, cells were fixed in 4% paraformaldehyde and permeabilized in 0.5% TritonX-100. Primary antibodies rabbit anti-53BP1 (NOVUS Biologicals NB100-304), mouse anti- γ H2AX (Millipore clone JBW301), and rabbit anti-ZNF384 (ATLAS antibodies HPA004051) were used to stain selected proteins. Proximity Ligation Assay was performed with Duolink In Situ PLA Probe Anti-Mouse Plus (Sigma) and Anti-Rabbit Minus (Sigma), and with Duolink In Situ Detection Reagents Orange (Sigma) according to manufacturer's instructions. Finally, secondary antibodies anti-rabbit coupled to Alexa488 (Invitrogen) and anti-mouse coupled to Alexa 647 (Invitrogen) were used to stain selected proteins in immunofluorescence. Number and intensity of PLA foci per cell were analysed by the imaging software ImageJ version 1.48.

Fluorescence Recovery After Photobleaching of ZNF384

FRAP of GFP-tagged ZNF384 constructs was performed on performed on a Nikon Ti-E inverted microscope equipped with a spinning-disk scan head CSU-X1 from Yokogawa at a rotation speed of 5000 rpm, a Plan APO 60x/1.4 N.A oil-immersion objective lens and a sCMOS ORCA Flash 4.0 camera. The fluorescence of EGFP was excited with lasers at 490

nm. Bandpass filters adapted to the fluorophore emission spectra were used for fluorescence detection. Local bleaching within a 4 μm diameter circular area in the cell nucleus was performed using a dedicated single-point scanning head (iLas2 from Roper Scientific) coupled to the epifluorescence backboard of the microscope. Images were collected at 2 images/second. To estimate fluorescence recovery kinetics, the mean fluorescence intensity inside the bleached area was measured by automatic segmentation using a custom-made custom-made MATLAB (MathWorks) program R2014b (version 8.4.0.150421) (available upon request). This routine allowed for background subtraction from the intensity measurements and correction for photobleaching due to imaging by dividing the intensity in the bleached area with the one measured for the whole nucleus. The recovery time was the time required to recover half of the fluorescence signal lost upon photobleaching.

Fluorescence Recovery After Photobleaching of Ku70

Fluorescence Recovery After Photobleaching (FRAP) of Ku70 was performed on a Zeiss LSM880 confocal setup equipped with a Plan APO 63x/1.2 N.A. water immersion objective. Samples were maintained at 37°C using a heating chamber. GFP fluorescence was excited at 488 nm and emission was detected at 500-590 nm. DNA damage was induced in a 6x2 μm area of the cell nucleus with a pulsed infrared laser set at 800 nm (Mai Tai, Spectra-Physics). Regions of interest of sizes ranging between 1 and 4 μm^2 located inside the previously irradiated area were bleached using a 488 nm laser. Images of the subsequent fluorescence recovery were collected at 4 frames per second using Zen Black (version 14.0.9.201). After background subtraction, the fluorescence recovery kinetics were obtained by dividing the signal within the bleached area to the one measured in the unbleached part of the damaged region.

Fluorescence correlation spectroscopy of Ku70

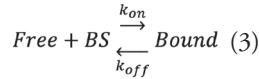
Fluorescence correlation spectroscopy (FCS) of Ku70 was performed on a Zeiss LSM880 confocal microscope equipped with a C-Apo 40x/1.2 N.A water immersion lens. GFP fluorescence was excited with a 488 nm laser and single emitted photons at wavelengths ranging between 500 and 550 nm were detected and counted on the GaAsP spectral detector. The laser power used for FCS measurements was adjusted to minimize photobleaching. FCS acquisition lasted 30 seconds to reduce the noise in the autocorrelation curves. Samples were maintained at 37°C using a heating chamber. FCS curves were detrended for slow fluctuations using Fluctuation Analyzer 4G [67].

Mathematical models for fitting of the FRAP and FCS data

The diffusion-limited model used to fit the FRAP curves is expressed as,

$$frap(t) = e^{-\frac{T_D}{2t}} \left[I_0 \left(\frac{T_D}{2t} \right) + I_1 \left(\frac{T_D}{2t} \right) \right] \quad (2)$$

where T_D is the characteristic diffusion time within the bleached area and I_0 and I_1 are modified Bessel functions of the first kind. The parameter T_D varies with the diffusion coefficient of Ku70 but also, in case of transient interactions with DNA, it depends on the K_d of this interaction [68]. The reaction-limited model assumes that Ku70 interacts with the DNA breaks according to the following reaction:



with *Free* and *Bound* referring to the binding state of Ku and *BS* to the break site. The mathematical expression of the reaction-limited model is then as follows:

$$frap(t) = 1 - \frac{k'_{on}}{k'_{on} + k_{off}} e^{-k_{off}t} \quad (4)$$

where k'_{on} is the pseudo first-order association rate corresponding to the product of the association rate k_{on} by the local concentration of break sites $[BS]$ and k_{off} is the dissociation rate. The one-population model used to fit the correlation curves is expressed as

$$G(t) = \frac{1}{2^{3/2}N} \left(1 + \frac{t}{T} \right)^{-1} \left(1 + \frac{t}{\omega^2 T} \right)^{-1/2} \quad (5)$$

where N is the number of tagged molecules in the focal volume, T is the residence time in the focal volume, and ω is the structural parameter of the focal volume, which was fixed to 6. Similarly, the two-population model used to fit the correlation curves is expressed as

$$G(t) = \frac{1}{2^{3/2}N} \left[f_1 \left(1 + \frac{t}{T_1} \right)^{-1} \left(1 + \frac{t}{\omega^2 T_1} \right)^{-1/2} + (1 - f_1) \left(1 + \frac{t}{T_2} \right)^{-1} \left(1 + \frac{t}{\omega^2 T_2} \right)^{-1/2} \right] \quad (6)$$

where T_1 and T_2 are the residence times of the two populations in the focal volume and f_i is the fraction of the molecules belonging to the population displaying a residence time T_i .

Fluorescence three-hybrid assay

Fluorescence three-hybrid/PAR-3H assays were performed as described [26]. Briefly, GFP-tagged proteins were tethered to a genomically integrated LacO array using a LacI-GFP trap in U2OS-2B2 cells [69] expressing mCherry-PARP1. Cells were sensitized with Hoechst and micro-irradiated with 405 nm light to induce DNA damage. If the GFP-tagged protein of interest is able to bind PAR, PARylated mCherry-PARP1, which

is generated at sites of DNA damage, will enrich at the LacO array after DNA damage induction. The mCherry-PARP1 signal intensity at the LacO array was quantified pre and 30, 60 and 120 seconds post DNA damage induction. The average intensity at the lacO array was normalized to the average intensity of the nucleus and corrected for background signal.

Immunofluorescence analysis

Cells were either directly fixed with 2% formaldehyde in PBS for 20 minutes at room temperature (RT), or pre-extracted with 0.5% Triton-X100 (Serva) in PBS on ice for 2 minutes prior to fixation. Alternatively, cells were fixed, post-extracted with 0.25% Triton-X100 (Serva) in PBS and treated with 100 mM glycine in PBS for 20 minutes to block unreacted aldehyde groups. Cells were then rinsed with PBS and equilibrated in wash buffer (PBS containing 0.5% BSA). Antibody incubation steps and washes were in wash buffer. Primary antibodies were incubated for 1-2 hours at room temperature. Detection was done using goat anti-mouse or goat anti-rabbit Ig coupled to Alexa 488, 555 or 647 (1:1500; Invitrogen Molecular probes) or Cy3-conjugated goat anti-mouse secondary antibody (1:100; Jackson Immuno research). All antibodies are listed in Supplementary Table 4. Samples were incubated with 0.1 $\mu\text{g}/\text{mL}$ 4',6-Diamidino-2-Phenylindole Dihydrochloride (DAPI) and mounted in Polymount.

DSB reporter assay

U2OS 2-6-5 cells stably expressing ER-mCherry-LacR-FokI-DD [36] were treated for 5 hours with 1 μM Shield-1 (Clontech Laboratories UK Ltd) and 1 μM 4-hydroxytamoxifen (4-OHT, Sigma-Aldrich) to induce DSBs.

Pulldown and co-immunoprecipitation assays

GFP-pulldowns were performed on U2OS Flp-In/T-Rex cells expressing GFP-NLS, GFP-ZNF384^{WT} or the indicated mutants and on HeLa and GFP-Ku80-expressing HeLa cells, while untransfected U2OS cells were used for co-immunoprecipitation assays. Cells were lysed in EBC buffer (50 mM Tris, pH 7.5, 150 mM NaCl, 0.5% NP-40, 2 mM MgCl_2 , protease inhibitor cocktail tablets) with 500 units benzonase. Samples were incubated for 1 hour at 4°C under constant mixing. 50 μL input sample was collected in a separate tube and mixed with 2x Laemmli buffer. The cleared lysates were subjected to GFP pulldown with GFP-Trap

beads (Chromotek) or immunoprecipitation using a specific antibody (or corresponding IgG control) that was conjugated to Protein G-coupled agarose beads (Millipore 16-201). The beads were then washed 6 times with EBC buffer and boiled in 2x Laemmli buffer along with the input samples. Samples were subjected to western blot analysis.

Sample preparation and mass spectrometry

For mass spectrometry, U2OS Flp-In/T-Rex cells expressing GFP-NLS and GFP-ZNF384^{WT} were treated with 0.5 mM Phleomycin for 1 hour or left untreated. Cell pellets were lysed in EBC-1 buffer (50 mM Tris, pH 7.5, 150 mM NaCl, 0.5% NP-40, 2 mM MgCl₂, protease inhibitor cocktail tablets) with 500 units benzonase. Samples were incubated for 1 hour at 4°C under constant mixing followed by high speed centrifugation for 10 minutes at 4°C. Protein concentration was measured by Qubit in the cleared lysates, equalized and transferred to tubes containing GFP-Trap beads (Chromotek). After 90 minutes of incubation at 4°C under rotating condition, the beads were washed 4 times with EBC-2 buffer (50 mM Tris pH 7.5, 150 mM NaCl, 1 mM EDTA, and protease inhibitor cocktail tablets) and 3 times with 50 mM ammonium bicarbonate followed by overnight digestion using 2.5 µg trypsin at 37°C under constant shaking. Digestion was terminated with 1% trifluoroacetic acid and centrifuged for 5 minutes at high speed to precipitate insoluble fractions. Consequently, C18 cartridges were prepared by washing 2 times with acetonitrile followed by 2 times with 0.1% Acetic acid. Peptides were loaded on the cartridge, while bound peptides were washed 2 times with 0.1% acetic acid and eluted with 1 mL 80% acetonitrile / 0.1% acetic acid and lyophilized.

Mass spectrometry was performed essentially as previously described [70]. Samples were analyzed on a Q-Exactive Orbitrap mass spectrometer (Thermo Scientific, Germany) coupled to an EASY-nanoLC 1000 system (Proxeon, Odense, Denmark). Digested peptides were separated using a 15 cm fused silica capillary (ID: 75 µm, OD: 375 µm, Polymicro Technologies, California, US) in-house packed with 1.9 µm C18-AQ beads (ReproSpher-DE, Pur, Dr. Maisch, Ammerburch-Entringen, Germany). Peptides were separated by liquid chromatography using a gradient from 2% to 95% acetonitrile with 0.1% formic acid at a flow rate of 200 nl/minute for 65 minutes. The mass spectrometer was operated in positive-ion mode at 2.8 kV with the capillary heated to 250°C, and in a Data-Dependent Acquisition (DDA) mode with a top 7 method. Full scan MS spectra were obtained with a resolution of 70,000, a target value of

3×10^6 and a scan range from 400 to 2,000 m/z . Maximum Injection Time (IT) was set to 50 ms. Higher-Collisional Dissociation (HCD) tandem mass spectra (MS/MS) were recorded with a resolution of 35,000, a maximum IT of 20 ms, a target value of 1×10^5 and a normalized collision energy of 25%. The precursor ion masses selected for MS/MS analysis were subsequently dynamically excluded from MS/MS analysis for 60 seconds. Precursor ions with a charge state of 1 and greater than 6 were excluded from triggering MS/MS events. Three replicates were included per condition with two technical repeats each.

Mass spectrometry data analysis

Raw mass spectrometry files were analysed with MaxQuant software (v1.5.5.1) as described [71] with the following modifications from default settings: the maximum number of miscleavages by trypsin/p was set to 3, Label Free Quantification (LFQ) was enabled disabling the Fast LFQ feature. Match-between-runs feature was enabled with a match time window of 0.7 minutes and an alignment time window of 20 minutes. We performed the search against an *in silico* digested UniProt reference proteome for Homo sapiens (8th June 2020). Analysis output from MaxQuant was further processed in the Perseus computational platform (version 1.5.5.3) [71]. Proteins identified as common contaminants, only identified by site and reverse peptide, were filtered out, and then all the LFQ intensities were log₂ transformed. Different biological repeats of each condition were grouped and only protein groups identified in all three biological replicates in at least one condition were included for further analysis. Missing values were imputed using Perseus software by normally distributed values with a 1.8 downshift (log₂) and a randomized 0.3 width (log₂) considering total matrix values. Volcano plots were generated, and Student's T-tests were performed to compare the different conditions. Spreadsheets from the statistical analysis output from Perseus were further processed in Microsoft Excel for comprehensive visualization and analysis of the data (Supplementary Table 1).

Western blot analysis

Cells were lysed in 2x Laemmli buffer and proteins were separated by Sodium Dodecyl Sulfate PolyAcrylamide Gel Electrophoresis (SDS-PAGE) using 4-12% pre-cast polyacrylamide gels (BioRad or Invitrogen) and MOPS running buffer (Invitrogen). Next, proteins were transferred onto nitrocellulose membranes (Millipore). Protein expression was analyzed by immunoblotting with the indicated primary antibodies

(Table 3) and secondary CF680 goat anti-rabbit or CF770 goat anti-mouse Ig antibodies (1:5000, Biotium). Membranes were scanned and analyzed using an Odyssey Infrared Imaging System (Licor; V3.0) and Image Studio Lite (version 5.2). Uncropped blots are provided in the source data file.

Chromatin fractionation

Chromatin fractionation was performed using a previously published protocol [72] with few modifications. Briefly, 100.000-150.000 cells were grown per 6-cm dish for 24 h and then transfected with siRNAs. Next, the cells were treated with 500 μ M phleomycin for 1 hour, washed three times with PBS, and incubated in NETN extraction buffer (100mM NaCl, 1mM EDTA, 20mM Tris-Cl pH8, 0,5% NP-40 + Proteasome inhibitors). After 15 minutes of incubation on ice, samples were taken for the chromatin-unbound fraction and mixed with the same amount of 2x Laemmli buffer. Cells were washed with PBS, lysed, and incubated in Laemmli buffer with benzonase for 15 minutes to obtain the chromatin-bound fraction. Samples were heated for 7 minutes at 80°C and subjected to Western blot analysis.

MBP-based protein purifications

For MBP-based purification, cultures of *Escherichia Coli* BL21-CodonPlus (DE3)-RIL cells containing pET-His6-MBP, pET-His6-MBP-ZNF384, pET-His6-MBP-C2H2, pET-His6-MBP-N-terminus and pET-His6-MBP-C-terminus plasmids were grown to an OD₆₀₀ of 0.3 absorbance units. To start induction of protein expression, 0.3 mM IPTG was added to the culture followed by incubation overnight at 20 °C. After centrifugation, cell pellets from were frozen and stored at -80 °C. For protein purification, cell pellets were lysed in 5 ml B-per™ Bacterial Protein Extraction Reagent (Thermo Fisher Scientific) supplemented with protease inhibitors (Sigma) and 15 kU rLysozyme (Merck) until the lysates were clear. Viscosity of the lysate was decreased by the addition of 125 units benzonase or sonication. The lysate was centrifuged for centrifuge for 10 min at 21000 g at 4°C in a table centrifuge 21000 g. For the ZNF384 FL, N-terminus and C- terminus fragments, the supernatant was loaded on a column packed with 0.75 ml Amylose Resin High Flow (NEB) installed in ÄKTA pure protein purification system (Cytiva). The column was washed with buffer A (20 mM Tris pH 7.4, 200 mM NaCl, 1 mM EDTA, 10 mM β -ME) and the proteins were eluted with buffer B (buffer A + 10 mM maltose). For the ZNF384 C2H2 fragment, two purification steps were performed. First, the supernatant was loaded on HiTrap SP

HP Strong Cation Exchange column (Cytiva) and proteins were eluted using a linear gradient from 50 to 1000 mM NaCl in 20 mM Tris pH 7.4, 10 mM β -ME collecting 2 ml fractions. Second, the fractions containing C2H2 were loaded on to the Amylose column, followed by washing and elution with buffer A and B, respectively.

Biotinylated DNA substrates

Biotinylated DNA substrates (Supplementary Table 5) were used at a concentration of 1 pmol/ μ l. dsDNA substrates were made by annealing complementary oligo's (Table 2 and 4) in reaction buffer (10 mM Tris pH 7.5, 150 mM KCl, 5 mM MgCl_2 , 0.25% Tween-20, 3.5 mM DTT, 5 % glycerol). Annealing was done in a PCR machine heating for 2 minutes to 95 °C, then gradually cooling over a period of 45 minutes to 25 °C.

DNA pulldown assay

DNA binding reactions were done at 4 °C in 40 μ l reaction buffer containing 0.1% BSA, 10 pmol biotinylated DNA substrate (Supplementary Table 5), and ~50 fmol of purified MBP or the different MBP-tagged ZNF384 proteins. After 30 minutes, reaction buffer containing 10 μ l Dynabeads M-280 Streptavidin suspension and 0.1% BSA was added and samples were incubated for 15 minutes at 4 °C. After this incubation, beads were washed 3 times using 200 μ l reaction buffer and loaded on 4-12% polyacrylamide Bis-Tris gel. After electrophoresis, proteins were blotted onto PVDF membranes for one hour at 50 Volt. Membranes were incubated at room temperature for 1 hour with mouse monoclonal anti-MBP antibody (NEB), followed by 1 hour incubation with goat anti-mouse HRP antibody (Bethyl Laboratories), and imaged by AI680 imager (GE) with ECL. For Ku70/Ku80 DNA binding reactions to 3'overhang DNA, His-MBP-ZNF384 or His-MBP, 100 fmol Ku70/Ku80 heterodimer and 10 pmol 3'-overhang biotinylated oligo was incubated in 40 μ l reaction buffer (10 mM Tris pH 7.5, 150 mM KCl, 5 mM MgCl_2 , 0.25% Tween-20, 3.5 mM DTT, 5 % glycerol) with 0.1% BSA for 30 minutes at 4 °C. After 30 minutes, reaction buffer containing 10 μ l Dynabeads M-280 Streptavidin suspension and 0.1% BSA was added and samples were incubated for 30 minutes at 4 °C. After this incubation, beads were washed three times with 200 μ l reaction buffer, Laemmli sample buffer was added and samples were incubated for 10 minutes at 95 °C. For separation by electrophoresis samples were loaded on Bolt 4-12% polyacrylamide Bis-Tris Mini Protein gel (ThermoFisher). After electrophoresis, western blotting was performed and the blots were stained using mouse anti-MBP (NEB) and rabbit anti-

Ku80 (Santa Cruz) as primary antibodies and goat anti-Rabbit^{CF680} and goat anti-Mouse^{CF770} (Biotium) as secondary antibodies for detection with an Odyssey Infrared Imaging System (Licor; V3.0).

In vitro pulldown assay

Protein reactions and washing steps were all done at room temperature. 15 μ l DynabeadsTM M-280 Sheep anti-Mouse IgG (Thermo Scientific) were incubated with 2 μ g mouse anti-Ku80 antibody (Santa Cruz) in 40 μ l PBS containing 0.1% BSA for 30 minutes. Beads were collected using a magnetic rack. After discarding the supernatant, beads were washed with 200 μ l PBS containing 0.1% BSA and incubated for 30 minutes with 6 pmol recombinant His-Ku70/Ku80 (Sino Biological) in 10 μ l reaction buffer (10 mM Tris pH 7.5, 150 mM KCl, 5 mM MgCl₂, 0.25% Tween-20, 3.5 mM DTT, 5 % glycerol). Beads were collected and supernatant was discarded. Beads were then washed with 200 μ l reaction buffer and 10 μ l of 0.2% BSA was added to the reaction buffer. After 15 minutes, 10 μ l reaction buffer with 1 pmol of purified His-MBP-tagged protein was added and samples were incubated for 30 minutes. Beads were collected and the supernatant was removed. Beads were subsequently washed 4 times with 200 μ l reaction buffer. Samples were heated in Laemmli sample buffer for 10 minutes at 95 °C. For electrophoresis, samples were loaded on Bolt 4-12% polyacrylamide Bis-Tris Mini Protein gel (ThermoFisher). After electrophoresis, Western blotting was performed and the blots were stained using mouse anti-MBP (NEB) and rabbit anti-Ku80 (Santa Cruz) as primary antibodies and goat anti-Rabbit^{CF680} and goat anti-Mouse^{CF770} (Biotium) as secondary antibodies for detection with an Odyssey Infrared Imaging System (Licor; V3.0).

Biolayer interferometry (BLI) measurements

BLI measurements were done on an OctedRed System (Sartorius), shaking the assay plate (1000 rpm) at 298K. All steps were performed in BLI buffer (10 mM Tris PH7.5, 150 mM KCl, 5 mM MgCl₂, 0.05% (v/v) Tween-20, 0.1% (w/v) BSA, 1 mM DTT). Biotinylated DNA substrates (Supplementary Table 5) were immobilised on streptavidin sensors pre-equilibrated in BLI buffer, after which a washout in BLI buffer was done. Then, 400 nM of purified MBP or the different MBP-tagged ZNF384 proteins was used to measure the association of the analyte. Resulting data were processed using the ForteBio Data Analysis software (version 7.1.0.38).

Quantitative Fluorescence *In Situ* Hybridization (FISH) of telomeres

Telomere FISH was based on a previously published protocol [51]. Briefly, HCT116 cells were harvested following 2 hours of colcemid (Sigma) incubation. After hypotonic swelling, cells were fixed in methanol/acetic acid, dropped on slides and dried at 37°C overnight. The next day slides were treated with RNaseA (R4642; Sigma), pepsin (P7000; Sigma) at pH 2, followed by formaldehyde fixation, washes in PBS, dehydration in ethanol and air drying. Hybridization mixture containing 70% formamide, 0.3 mg/ml Cy-3-conjugated (C3TA2)₃ peptide nucleic acid (PNA) probe in 10 mM Tris (pH 7.5) was added to the slide, after which a coverslip was added followed by DNA denaturation for 1.5 minute at 80°C. After hybridization for 2 hours at room temperature, slides were washed with 70% formamide / 10 mM Tris / pH 7.2, and 0.05 M Tris / 0.15 M NaCl containing 0.05% Tween-20. Slides were stained with DAPI, dehydrated with ethanol, air dried, and mounted in Aquapoly-mount (Polysciences). Images were acquired on a Zeiss AxioImager M2 widefield fluorescence microscope with 63x PLAN APO (1.4 NA) oil-immersion objectives (Zeiss). Integrated density and area of single telomeres was measured with ImageJ (version 1.48) by using Threshold, Polygon and Analyze Particles functions, subsequently. While obtaining images we noticed variation of telomere signals between metaphases and less so within one metaphase spread. Therefore, after subtraction of background values the average integrated density per telomere of each metaphase was calculated and plotted.

DR-GFP and EJ5-GFP reporter assays

U2OS cells containing either a stably integrated copy of the DR-GFP or EJ5-GFP reporter were used to measure the repair of I-*SceI*-induced DSBs by HR or NHEJ [42, 62]. Briefly, DR-GFP U2OS cells or EJ5-GFP U2OS cells treated with siRNA for 48 hours were co-transfected with an mCherry expression vector and the I-*SceI* expression vector pCBASceI [62]. 48 hours later the percentage of GFP-positive cells among the mCherry-positive cells was determined by FACS on a BD LSRII flow cytometer (BD Bioscience) using FACSDiva software version 5.0.3. An example of the gating strategy can be found Fig S15I. Quantifications were performed with FACSDiva™ (BD Biosciences).

Random plasmid integration assay

U2OS cells were seeded (day 1) and transfected with siRNAs the following day (day 2). Later at day 2, the cells were transfected with 2 μ g gel-purified *Bam*HI/*Eco*RI-linearized pEGFP-C1 plasmid. The cells were subsequently transfected twice with siRNAs at 24 and 36 hours after the first transfection (day 3 and day 4, respectively). On day 5, cells were collected, counted, seeded and grown in medium without or with 0.5 mg/mL G418. The transfection efficiency was determined on the same day by FACS analysis using GFP fluorescence as a measure. The cells were incubated at 37°C to allow colony formation and medium was refreshed on day 8 and 12. On day 15, the cells were washed with 0.9% NaCl and stained with methylene blue (2.5 g/L in 5% ethanol, Sigma-Aldrich). Colonies of more than 50 cells were scored. Random plasmid integration efficiency was scored as the number of G418-resistant colonies normalized by the plating efficiency, which was determined by the number of colonies formed on plates without G418 and corrected for the transfection efficiency.

Analysis of repair junctions in the GC92 reporter

Sequence analysis of repair junctions in the GC92 reporter was performed as described [49]. Briefly, GC92 fibroblasts were first transfected with siRNAs and 48 hours later with the *I-Sce*I expression vector pCBASce [62]. 48 hours later, genomic DNA was extracted using phenol:chloroform:isoamyl alcohol (25:24:1 v/v, Invitrogen). PCR was performed on the genomic DNA using the CMV1 and CD4int primers (Supplementary Table 3) to amplify repair junctions. PCR products were cloned into pGEM-T easy vector (Promega). Colony PCR was performed using M13 primers (Supplementary Table 3) on individual bacterial colonies to amplify repair junctions, which were subjected to Sanger sequencing using the M13 FW primer (Supplementary Table 3). Sequences were analyzed using a custom Sanger sequence analyzer as described previously [39].

Cell survival assays

VH10-SV40 cells were transfected with siRNAs, trypsinized, seeded at low density and exposed to IR. For HeLa Flp-In/T-Rex, cDNAs were expressed by adding Dox for 24 hours after siRNA transfection. U2OS cells were seeded at low densities and exposed to increasing doses of olaparib. After 7 days, the cells were washed with 0.9% NaCl and stained with methylene blue (2.5 g/L in 5% ethanol, Sigma-Aldrich). Colonies of more than 20 cells were scored.

Cell cycle profiling

Cells were fixed in 70% ethanol, followed by DNA staining with 50 $\mu\text{g/mL}$ propidium iodide in the presence of RNase A (0.1 mg/mL; Sigma). Cell acquisition and quantification was performed on a BD LSRII flow cytometer (BD Bioscience) using FACSDiva software version 5.0.3.

Statistics and reproducibility

Results were confirmed in multiple cell lines or by using complementary approaches. All experiments yielding micrographs, pull-down experiments and western blot analysis were performed independently at least twice, but often three times. The MS experiments were performed in triplicate. Statistical analysis was carried out using the two-tailed Student's *t* test ($P < 0.05$). Boxplots were generated using R (version 4.0.5) and R Studio (version 1.4.1106).

DATA AVAILABILITY

The mass spectrometry proteomics data generated in this study and shown in Fig. 1D and Table S1 have been deposited to the ProteomeXchange Consortium via the PRIDE partner repository (<https://www.ebi.ac.uk/pride/>). Access can be obtained with the dataset identifier PDX020417 [73]. Additionally, publicly available reference datasets for Homo sapiens (8th June 2020) was used to search against an in silico digested UniProt reference proteome. Source data are provided with this paper.

CODE AVAILABILITY

The code used in this work is available at <https://github.com/sehuet/Singh-image-processing> [74].

ACKNOWLEDGEMENTS

We thank Robin van Schendel and Marcel Tijsterman for the custom Sanger Sequence analyzer and help with the sequence analysis, and Dik van Gent, Stephen Taylor, Geert Kopps, Bernard Lopez, Roger Greenberg, Maria Jasin, Jeremy Stark, Nicholas Lakin and Sylvia Gelpke-Vermeulen and Karoly Szuhai for kindly providing valuable reagents. We also thank the Microscopy-Rennes Imaging Center (BIOSIT, Université Rennes 1), member of the national infrastructure France-BioImaging supported by the French

National Research Agency (ANR-10-INBS-04), for providing access to their imaging setups, as well as S. Dutertre and X. Pinson for technical assistance with the microscopes. This research was financially supported by the European Research Council (ERC) under the European Union's Horizon 2020 research and innovation program (ERC-StG 310913 to A.C.O.V.; ERC-CoG 50364 to H.v.A), the Ligue contre le Cancer du Grand-Ouest (committees 22 and 35), the Fondation ARC pour la recherche sur le cancer (20161204883), the Agence Nationale de la Recherche (PRC-2018 REPAIRCHROM) and the Institut Universitaire de France (all grants to S.H.). R.S. is supported by the Fondation ARC pour la recherche sur le cancer (PDF20181208405).

AUTHOR CONTRIBUTION

J.S. generated partial ZNF384 knockout cells, ZNF384 plasmids and performed laser micro-irradiation, cell cycle profiling, pulldown and co-immunoprecipitation experiments, as well as plasmid integration, EJ5-GFP reporter assay and clonogenic survivals. R.S., O.D. and S.H. performed laser micro-irradiation, fluorescence three-hybrid assay, fluorescence correlation spectroscopy and FRAP. W.W.W. performed DR-GFP, immunofluorescence, FISH, and clonogenic survivals. K.V. generated all ZNF384 deletion constructs. M.B.R. performed GC92 reporter assays, pulldown experiments and generated ZNF384 plasmids. A.J.L.G prepared mass-spectrometry samples, purified recombinant proteins and performed *in vitro* DNA pulldown experiments. H.Q. and P.M.K. performed Ultra-soft X-ray irradiation experiments. R.Q.K. and M.L. performed BLI experiments. R.P. and A.C.O.V. performed mass-spectrometry experiments and data-analysis. H.v.A. conceived and supervised the project. J.S. and H.v.A. wrote the manuscript with input and edits from all authors.

COMPETING INTERESTS

The authors declare no competing interests.

REFERENCES

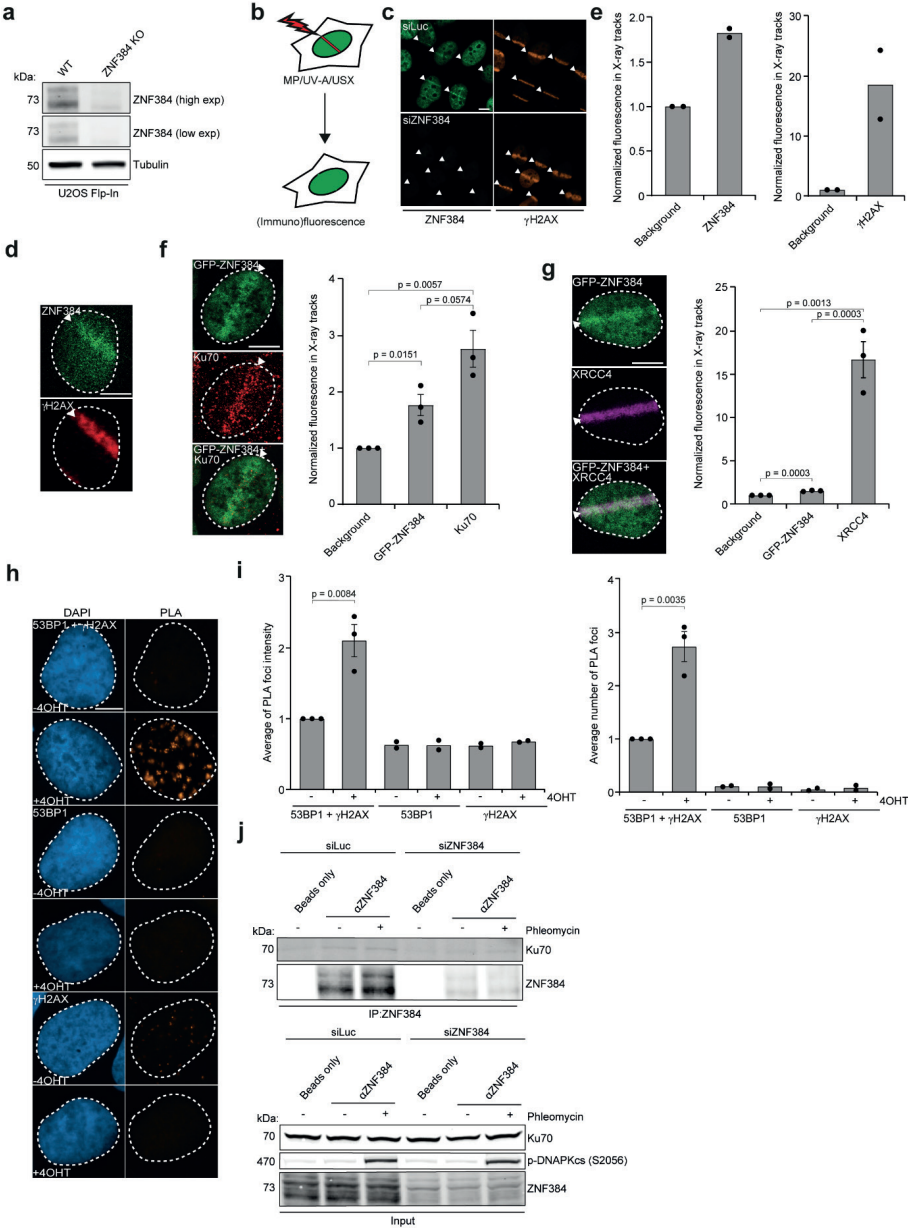
1. Jackson, S.P. and J. Bartek, *The DNA-damage response in human biology and disease*. Nature, 2009. **461**(7267): p. 1071-8.
2. Symington, L.S. and J. Gautier, *Double-strand break end resection and repair pathway choice*. Annu Rev Genet, 2011. **45**: p. 247-71.
3. Chang, H.H.Y., et al., *Non-homologous DNA end joining and alternative pathways to double-strand break repair*. Nat Rev Mol Cell Biol, 2017. **18**(8): p. 495-506.
4. Bhargava, R., D.O. Onyango, and J.M. Stark, *Regulation of Single-Strand Annealing and its Role in Genome Maintenance*. Trends Genet, 2016. **32**(9): p. 566-575.
5. Khurana, S., et al., *A macrohistone variant links dynamic chromatin compaction to BRCA1-dependent genome maintenance*. Cell Rep, 2014. **8**(4): p. 1049-62.
6. Dantuma, N.P. and H. van Attikum, *Spatiotemporal regulation of posttranslational modifications in the DNA damage response*. Embo j, 2016. **35**(1): p. 6-23.
7. Caron, P., et al., *WWP2 ubiquitylates RNA polymerase II for DNA-PK-dependent transcription arrest and repair at DNA breaks*. Genes Dev, 2019. **33**(11-12): p. 684-704.
8. Sellou, H., et al., *The poly(ADP-ribose)-dependent chromatin remodeler Alc1 induces local chromatin relaxation upon DNA damage*. Mol Biol Cell, 2016. **27**(24): p. 3791-3799.
9. Luijsterburg, M.S., et al., *PARP1 Links CHD2-Mediated Chromatin Expansion and H3.3 Deposition to DNA Repair by Non-homologous End-Joining*. Mol Cell, 2016. **61**(4): p. 547-562.
10. Gibbs-Seymour, I., et al., *HPF1/C4orf27 Is a PARP-1-Interacting Protein that Regulates PARP-1 ADP-Ribosylation Activity*. Mol Cell, 2016. **62**(3): p. 432-442.
11. Smith, R., et al., *Poly(ADP-ribose)-dependent chromatin unfolding facilitates the association of DNA-binding proteins with DNA at sites of damage*. Nucleic Acids Res, 2019. **47**(21): p. 11250-11267.
12. Izhar, L., et al., *A Systematic Analysis of Factors Localized to Damaged Chromatin Reveals PARP-Dependent Recruitment of Transcription Factors*. Cell Rep, 2015. **11**(9): p. 1486-500.
13. Vilas, C.K., et al., *Caught with One's Zinc Fingers in the Genome Integrity Cookie Jar*. Trends Genet, 2018. **34**(4): p. 313-325.
14. Singh, J.K. and H. van Attikum, *DNA double-strand break repair: Putting zinc fingers on the sore spot*. Semin Cell Dev Biol, 2020.
15. Cassandri, M., et al., *Zinc-finger proteins in health and disease*. Cell Death Discov, 2017. **3**: p. 17071.
16. Gong, F., et al., *Screen identifies bromodomain protein ZMYND8 in chromatin recognition of transcription-associated DNA damage that promotes homologous recombination*. Genes Dev, 2015. **29**(2): p. 197-211.
17. Chen, G., et al., *ZNF830 mediates cancer chemoresistance through promoting homologous-recombination repair*. Nucleic Acids Res, 2018. **46**(3): p. 1266-1279.
18. Nicolai, S., et al., *ZNF281 is recruited on DNA breaks to facilitate DNA repair by non-homologous end joining*. Oncogene, 2020. **39**(4): p. 754-766.
19. Kochan, J.A., et al., *Ultra-soft X-ray system for imaging the early cellular responses to X-ray induced DNA damage*. Nucleic Acids Research, 2019. **47**(17): p. e100-e100.

20. Galbiati, A., C. Beauséjour, and F. d'Adda di Fagagna, *A novel single-cell method provides direct evidence of persistent DNA damage in senescent cells and aged mammalian tissues*. Aging Cell, 2017. **16**(2): p. 422-427.
21. Fell, V.L. and C. Schild-Poulter, *The Ku heterodimer: function in DNA repair and beyond*. Mutat Res Rev Mutat Res, 2015. **763**: p. 15-29.
22. Davis, A.J., B.P. Chen, and D.J. Chen, *DNA-PK: a dynamic enzyme in a versatile DSB repair pathway*. DNA Repair (Amst), 2014. **17**: p. 21-9.
23. Beck, C., et al., *PARP3 affects the relative contribution of homologous recombination and nonhomologous end-joining pathways*. Nucleic Acids Res, 2014. **42**(9): p. 5616-32.
24. Gogola, E., et al., *Selective Loss of PARG Restores PARylation and Counteracts PARP Inhibitor-Mediated Synthetic Lethality*. Cancer Cell, 2018. **33**(6): p. 1078-1093.e12.
25. Jungmichel, S., et al., *Proteome-wide identification of poly(ADP-Ribosyl)ation targets in different genotoxic stress responses*. Mol Cell, 2013. **52**(2): p. 272-85.
26. Smith, R., et al., *CHD3 and CHD4 recruitment and chromatin remodeling activity at DNA breaks is promoted by early poly(ADP-ribose)-dependent chromatin relaxation*. Nucleic Acids Res, 2018. **46**(12): p. 6087-6098.
27. Kustatscher, G., et al., *Splicing regulates NAD metabolite binding to histone macroH2A*. Nat Struct Mol Biol, 2005. **12**(7): p. 624-5.
28. Smeenk, G., et al., *Poly(ADP-ribosyl)ation links the chromatin remodeler SMARCA5/SNF2H to RNF168-dependent DNA damage signaling*. J Cell Sci, 2013. **126**(Pt 4): p. 889-903.
29. Wang, Z., et al., *Recognition of the iso-ADP-ribose moiety in poly(ADP-ribose) by WWE domains suggests a general mechanism for poly(ADP-ribosyl)ation-dependent ubiquitination*. Genes Dev, 2012. **26**(3): p. 235-40.
30. Torrungruang, K., et al., *DNA binding and gene activation properties of the Nmp4 nuclear matrix transcription factors*. J Biol Chem, 2002. **277**(18): p. 16153-9.
31. Krasner, D.S., et al., *Interplay between Ku and Replication Protein A in the Restriction of Exo1-mediated DNA Break End Resection*. J Biol Chem, 2015. **290**(30): p. 18806-16.
32. Grundy, G.J., et al., *APLF promotes the assembly and activity of non-homologous end joining protein complexes*. Embo j, 2013. **32**(1): p. 112-25.
33. Shirodkar, P., et al., *Identification and functional characterization of a Ku-binding motif in aprataxin polynucleotide kinase/phosphatase-like factor (APLF)*. J Biol Chem, 2013. **288**(27): p. 19604-13.
34. Rulten, S.L., et al., *PARP-3 and APLF function together to accelerate nonhomologous end-joining*. Mol Cell, 2011. **41**(1): p. 33-45.
35. Nemoz, C., et al., *XLF and APLF bind Ku80 at two remote sites to ensure DNA repair by non-homologous end joining*. Nat Struct Mol Biol, 2018. **25**(10): p. 971-980.
36. Tang, J., et al., *Acetylation limits 53BP1 association with damaged chromatin to promote homologous recombination*. Nat Struct Mol Biol, 2013. **20**(3): p. 317-25.
37. Lu, H., et al., *DNA-PKcs promotes chromatin decondensation to facilitate initiation of the DNA damage response*. Nucleic Acids Res, 2019. **47**(18): p. 9467-9479.
38. Blackford, A.N. and S.P. Jackson, *ATM, ATR, and DNA-PK: The Trinity at the Heart of the DNA Damage Response*. Mol Cell, 2017. **66**(6): p. 801-817.

39. Schimmel, J., et al., *Mutational signatures of non-homologous and polymerase theta-mediated end-joining in embryonic stem cells*. *Embo j*, 2017. **36**(24): p. 3634-3649.
40. Drouet, J., et al., *DNA-dependent protein kinase and XRCC4-DNA ligase IV mobilization in the cell in response to DNA double strand breaks*. *J Biol Chem*, 2005. **280**(8): p. 7060-9.
41. Brown, E.J. and D. Baltimore, *Essential and dispensable roles of ATR in cell cycle arrest and genome maintenance*. *Genes Dev*, 2003. **17**(5): p. 615-28.
42. Bennardo, N., et al., *Alternative-NHEJ is a mechanistically distinct pathway of mammalian chromosome break repair*. *PLoS Genet*, 2008. **4**(6): p. e1000110.
43. Galanty, Y., et al., *Mammalian SUMO E3-ligases PIAS1 and PIAS4 promote responses to DNA double-strand breaks*. *Nature*, 2009. **462**(7275): p. 935-9.
44. McCabe, N., et al., *Deficiency in the repair of DNA damage by homologous recombination and sensitivity to poly(ADP-ribose) polymerase inhibition*. *Cancer Res*, 2006. **66**(16): p. 8109-15.
45. Ronato, D.A., et al., *Limiting the DNA Double-Strand Break Resectosome for Genome Protection*. *Trends Biochem Sci*, 2020. **45**(9): p. 779-793.
46. Lee, K.J., et al., *Phosphorylation of Ku dictates DNA double-strand break (DSB) repair pathway choice in S phase*. *Nucleic Acids Res*, 2016. **44**(4): p. 1732-45.
47. Shao, Z., et al., *Persistently bound Ku at DNA ends attenuates DNA end resection and homologous recombination*. *DNA Repair*, 2012. **11**(3): p. 310-316.
48. Kabotyanski, E.B., et al., *Double-strand break repair in Ku86- and XRCC4-deficient cells*. *Nucleic Acids Res*, 1998. **26**(23): p. 5333-42.
49. Taty-Taty, G.C., et al., *Control of alternative end joining by the chromatin remodeler p400 ATPase*. *Nucleic Acids Res*, 2016. **44**(4): p. 1657-68.
50. Rother, M.B., et al., *CHD7 and 53BP1 regulate distinct pathways for the re-ligation of DNA double-strand breaks*. *Nature Communications*, 2020. **11**(1): p. 5775.
51. Lansdorp, P.M., et al., *Heterogeneity in Telomere Length of Human Chromosomes*. *Human Molecular Genetics*, 1996. **5**(5): p. 685-691.
52. Jaco, I., P. Muñoz, and M.A. Blasco, *Role of human Ku86 in telomere length maintenance and telomere capping*. *Cancer Res*, 2004. **64**(20): p. 7271-8.
53. Caron, M.C., et al., *Poly(ADP-ribose) polymerase-1 antagonizes DNA resection at double-strand breaks*. *Nat Commun*, 2019. **10**(1): p. 2954.
54. Nakamoto, T., et al., *CIZ, a zinc finger protein that interacts with p130(cas) and activates the expression of matrix metalloproteinases*. *Mol Cell Biol*, 2000. **20**(5): p. 1649-58.
55. Dechering, K.J., et al., *Distinct frequency-distributions of homopolymeric DNA tracts in different genomes*. *Nucleic Acids Research*, 1998. **26**(17): p. 4056-4062.
56. Costantini, S., et al., *Interaction of the Ku heterodimer with the DNA ligase IV/Xrcc4 complex and its regulation by DNA-PK*. *DNA Repair (Amst)*, 2007. **6**(6): p. 712-22.
57. Zhao, B., et al., *The essential elements for the noncovalent association of two DNA ends during NHEJ synapsis*. *Nat Commun*, 2019. **10**(1): p. 3588.
58. Jette, N. and S.P. Lees-Miller, *The DNA-dependent protein kinase: A multifunctional protein kinase with roles in DNA double strand break repair and mitosis*. *Progress in Biophysics and Molecular Biology*, 2015. **117**(2): p. 194-205.

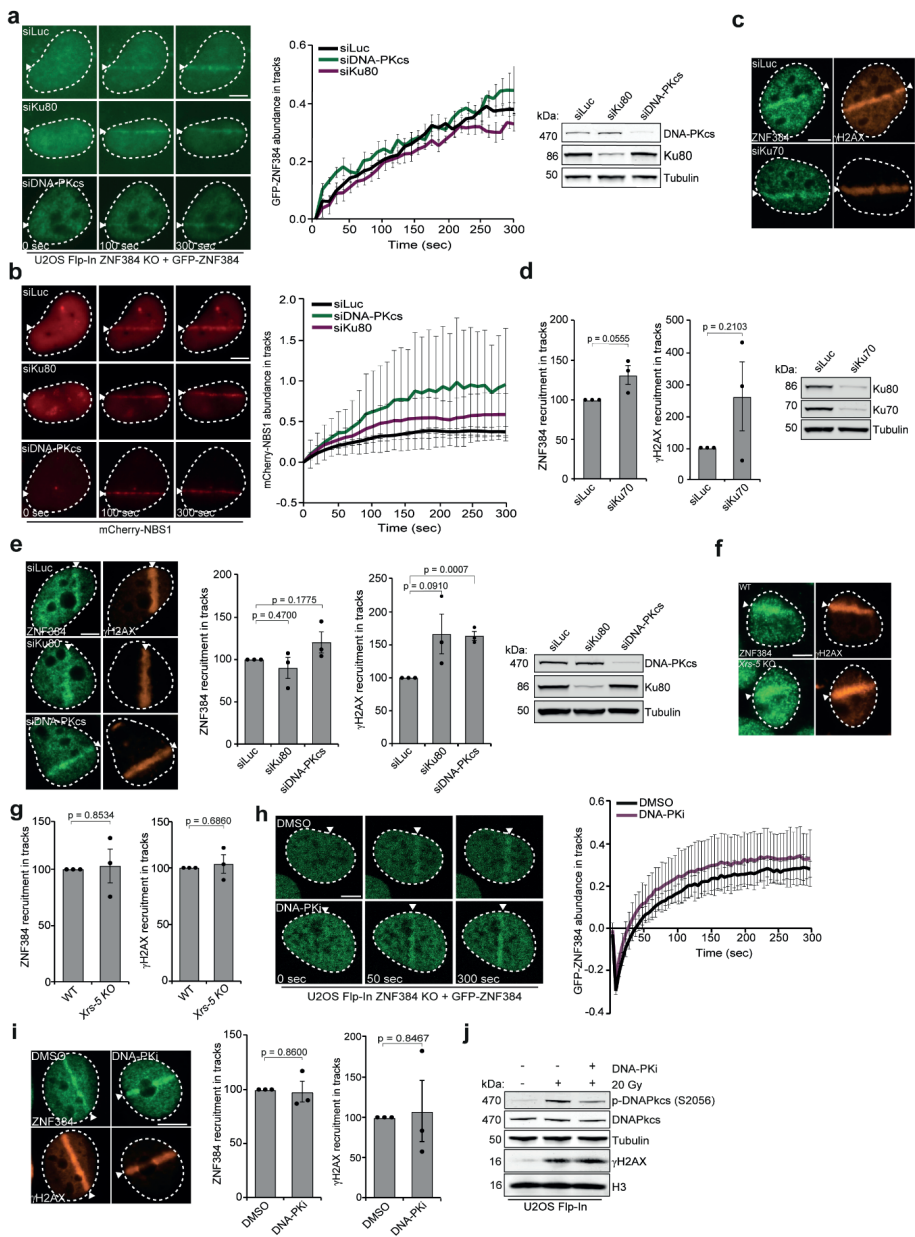
59. Douglas, P., et al., *Polo-like kinase 1 (PLK1) and protein phosphatase 6 (PP6) regulate DNA-dependent protein kinase catalytic subunit (DNA-PKcs) phosphorylation in mitosis*. Biosci Rep, 2014. **34**(3).
60. Helfricht, A., et al., *Loss of ZBTB24 impairs non-homologous end-joining and class-switch recombination in patients with ICF syndrome*. Journal of Experimental Medicine, 2020.
61. Britton, S., J. Coates, and S.P. Jackson, *A new method for high-resolution imaging of Ku foci to decipher mechanisms of DNA double-strand break repair*. J Cell Biol, 2013. **202**(3): p. 579-95.
62. Pierce, A.J., et al., *XRCC3 promotes homology-directed repair of DNA damage in mammalian cells*. Genes Dev, 1999. **13**(20): p. 2633-8.
63. Iacovoni, J.S., et al., *High-resolution profiling of gammaH2AX around DNA double strand breaks in the mammalian genome*. The EMBO journal, 2010. **29**(8): p. 1446-1457.
64. Ronson, G.E., et al., *PARP1 and PARP2 stabilise replication forks at base excision repair intermediates through Fbh1-dependent Rad51 regulation*. Nature Communications, 2018. **9**(1): p. 746.
65. Gottschalk, A.J., et al., *Poly(ADP-ribosyl)ation directs recruitment and activation of an ATP-dependent chromatin remodeler*. Proc Natl Acad Sci U S A, 2009. **106**(33): p. 13770-4.
66. Mehrotra, P.V., et al., *DNA repair factor APLF is a histone chaperone*. Mol Cell, 2011. **41**(1): p. 46-55.
67. Wachsmuth, M., et al., *High-throughput fluorescence correlation spectroscopy enables analysis of proteome dynamics in living cells*. Nat Biotechnol, 2015. **33**(4): p. 384-9.
68. Sprague, B.L., et al., *Analysis of binding reactions by fluorescence recovery after photobleaching*. Biophys J, 2004. **86**(6): p. 3473-95.
69. Czarna, A., et al., *Structures of Drosophila cryptochrome and mouse cryptochrome1 provide insight into circadian function*. Cell, 2013. **153**(6): p. 1394-405.
70. Kumar, R., et al., *The STUbL RNF4 regulates protein group SUMOylation by targeting the SUMO conjugation machinery*. Nat Commun, 2017. **8**(1): p. 1809.
71. Tyanova, S., T. Temu, and J. Cox, *The MaxQuant computational platform for mass spectrometry-based shotgun proteomics*. Nat Protoc, 2016. **11**(12): p. 2301-2319.
72. Feng, W., et al., *TRAP regulates replication fork recovery and progression via PCNA*. Cell Discov, 2016. **2**: p. 16016.
73. Perez-Riverol, Y., et al., *The PRIDE database and related tools and resources in 2019: improving support for quantification data*. Nucleic Acids Res, 2019. **47**(D1): p. D442-d450.
74. Singh J.K., R.S., M.B. Rother, A.J.L. de Groot, W.W. Wiegant, K. Vreeken, O. D'Augustin, R.Q. Kim, P.M. Krawczyk, R. González-Prieto, A.C.O. Vertegaal, M. Lamers, S. Huet and H. van Attikum., *Zinc finger protein ZNF384 is an adaptor of KU to DNA during classical non-homologous end-joining, Singh-image-processing*. 2021.

SUPPLEMENTARY FIGURES, LEGENDS AND TABLES

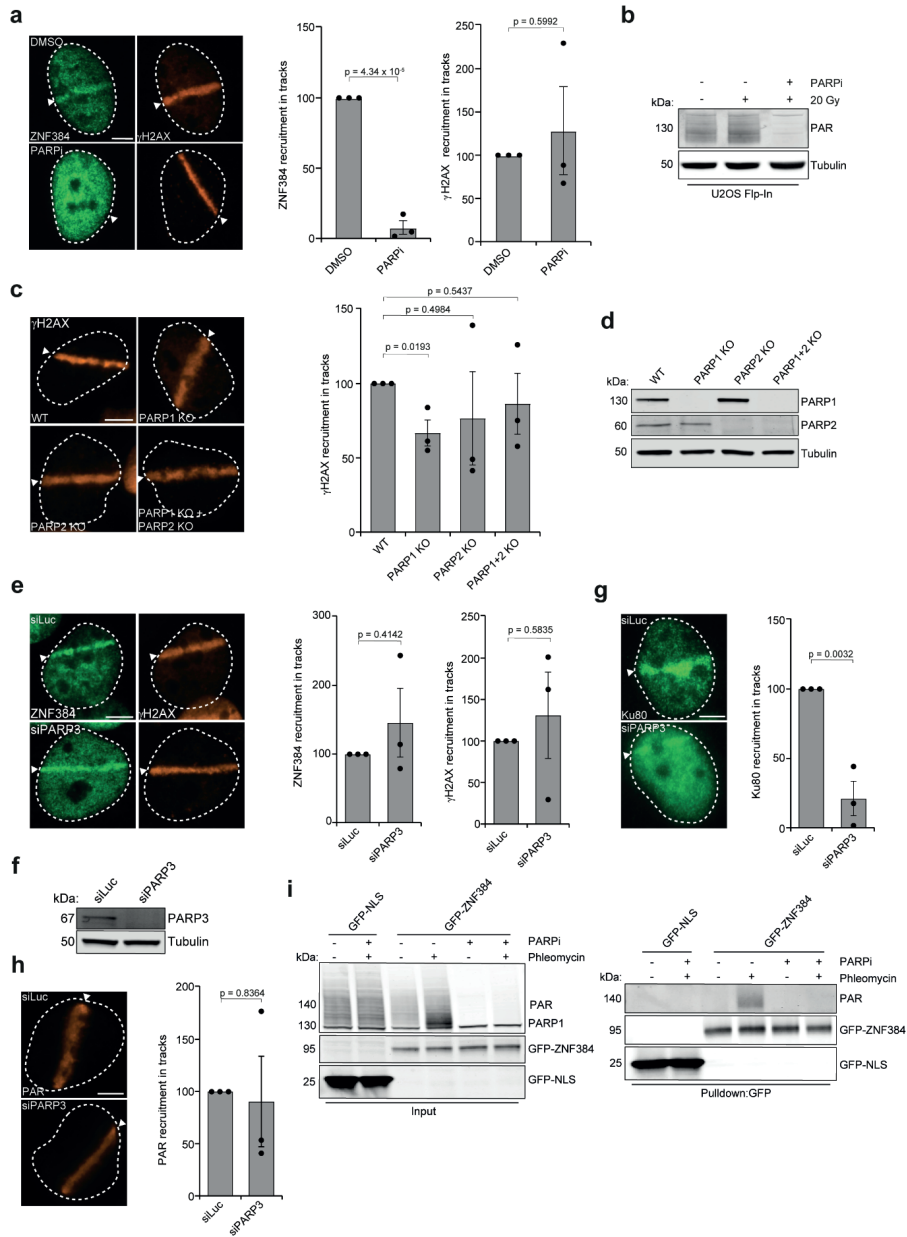


► **Supplementary Figure. 1 – related to Figure. 1. ZNF384 is recruited to DNA damage sites.**

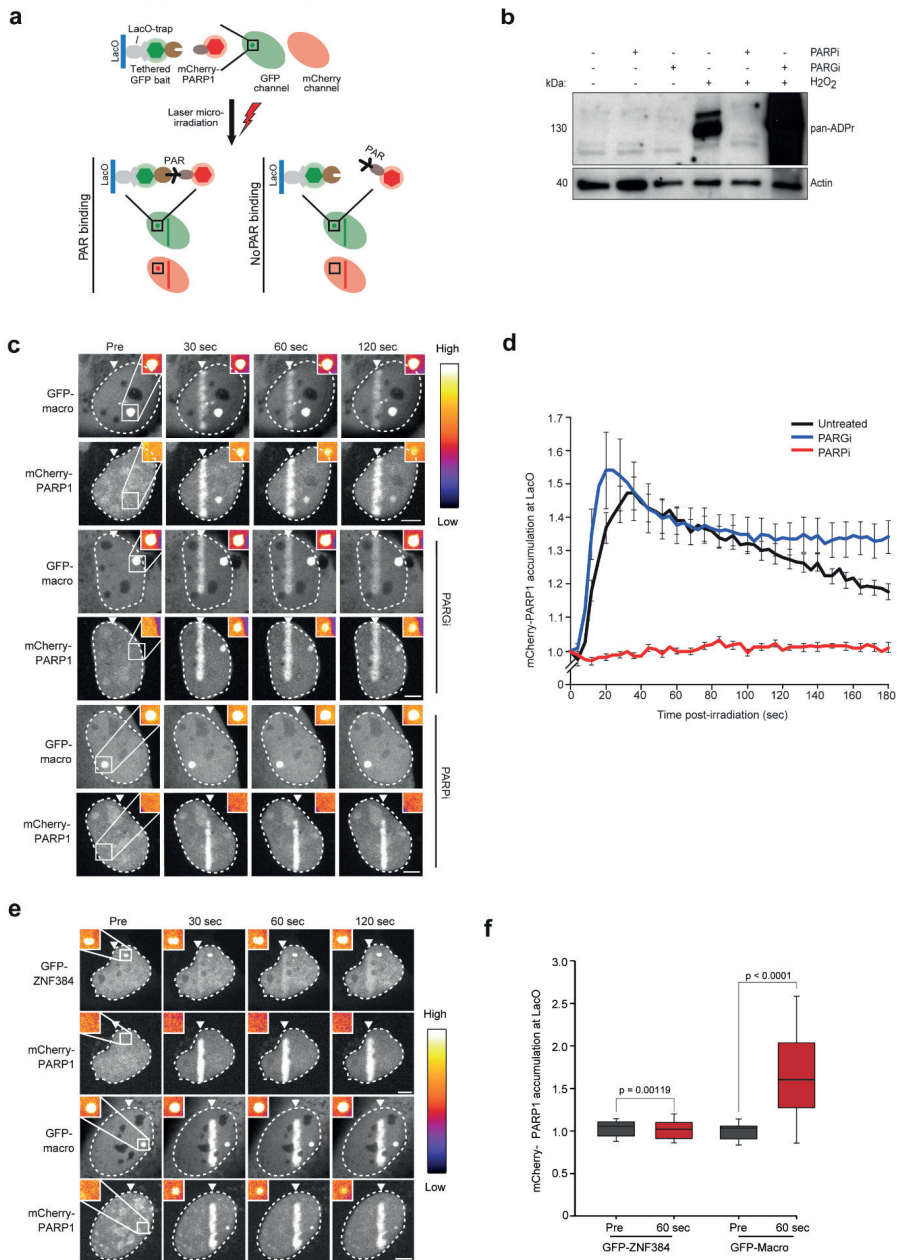
(A) Western blot analysis of ZNF384 expression in cells from Figure 1A. Tubulin is a loading control. Data shown represent 2 independent experiments. (B) Schematic representation of the laser micro-irradiation approach to study protein accumulation at sites of DNA damage. An 800 nm multiphoton (MP) laser, 365 nm UV-A laser or Ultra-soft X-ray (USX) irradiation was used. (C) Representative images of two independent experiments of the accumulation of ZNF384 at γ H2AX-marked 365 nm UV-A tracks in cells transfected with the indicated siRNAs. Cells were fixed and immunostained 10 minutes after laser micro-irradiation. White triangles indicate irradiated regions. (D) Accumulation of endogenous ZNF384 at γ H2AX-marked DNA damage inflicted by USX irradiation in U2OS Flp-In/T-Rex cells expressing doxycycline (dox)-inducible GFP-ZNF384. Cells were fixed and immunostained 5 minutes after USX irradiation. White triangles indicate irradiated regions. (E) Quantification of ZNF384 and γ H2AX accumulation in cells from D. The mean of at least 40 cells acquired in 2 independent experiments is shown. Data were normalized to the nuclear background outside the irradiated area, which was set to 1. (F) Accumulation of GFP-ZNF384 at sites of KU70-marked DNA damage inflicted by USX irradiation in U2OS Flp-In/T-Rex cells expressing doxycycline (dox)-inducible GFP-ZNF384. Cells were fixed and immunostained 5 minutes after laser micro-irradiation. White triangles indicate irradiated regions. (left panel). Quantification of ZNF384 and KU70 is presented as the \pm SEM of >45 cells acquired in 3 independent experiments. Data were normalized to the nuclear background outside the irradiated area, which was set to 1 (right panel). P-values were calculated using the two-tailed unpaired Student's *t* test. (G) As in F, but for GFP-ZNF384 and XRCC4. Quantification of ZNF384 and XRCC4 is presented as the \pm SEM of 60 cells acquired in 3 independent experiments. P-values were calculated using the two-tailed unpaired Student's *t* test, assuming unequal variances. (H) PLA of 53BP1 and ZNF384 and γ H2AX in *Asi*SI-ER-U2OS cells treated with 4-OHT for DSB induction. PLA foci were scored after 5 hours of DSB induction. (I) Quantification of H. PLA foci formation and foci intensity from >200 cells acquired in 2-3 independent experiments are shown. Statistical significance was calculated with the two-tailed Student's *t* test, assuming unequal variances. (J) Immunoprecipitation (IP) of endogenous ZNF384 from 500 μ M Phleomycin treated U2OS cells transfected with the indicated siRNAs. Control IP contained beads only. Blots were probed for ZNF384 and KU70. Data shown represent 2 independent experiments. Scale bar 5 μ m, except for C in which scale bar is 10 μ m. Source data are provided as Source Data file.



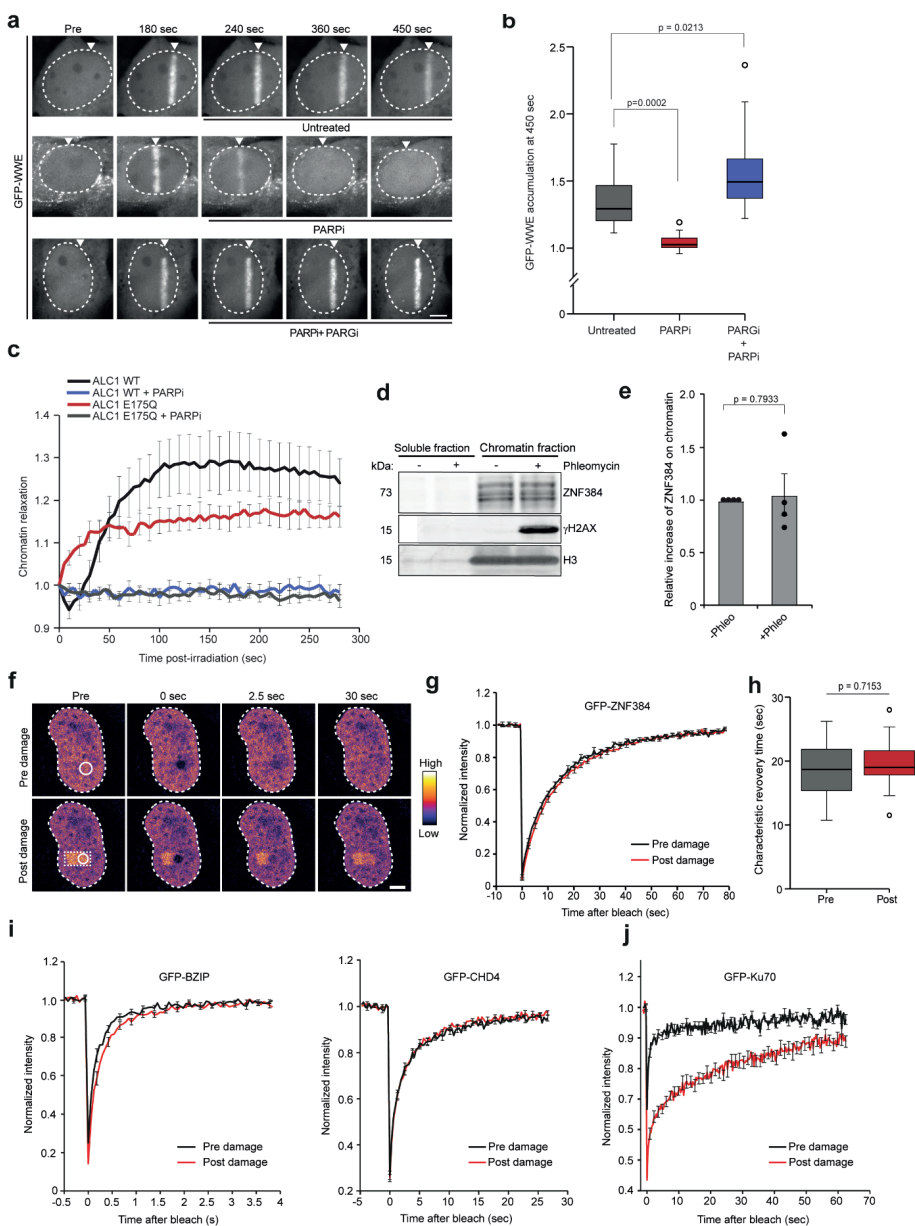
► **Supplementary Figure. 2 – related to Figure. 1. ZNF384 is recruited to DNA damage sites independent of KU70/KU80 and DNA-PKcs.** (A) Recruitment of GFP-ZNF384 to 365 nm UV-A tracks in BrdU-sensitized U2OS Flp-In/T-Rex ZNF384 KO cells. White triangles indicate irradiated regions (left panel). Quantification of the data is plotted on a time scale as relative abundance in tracks. The graph represents the mean \pm SEM of >40 cells acquired in 3 independent experiments (middle panel). Western blot analysis of KU80 and DNA-PKcs expression. Tubulin is a loading control. Data shown represent 2 independent experiments (right panel). (B) As in A, except for mCherry-NBS1. (C) Accumulation of endogenous ZNF384 at 365 nm UV-A tracks in BrdU-sensitized U2OS cells following transfection with siLuc and siKU70. Cells were fixed and immunostained 10 minutes after laser micro-irradiation. White triangles indicate irradiated regions. γ H2AX was used as a DNA damage marker. (D) Quantification of endogenous ZNF384 and γ H2AX levels in laser tracks in cells from D is presented as the mean \pm SEM of >180 cells acquired in 3 independent experiments (left panel). Western blot analysis of KU70 and K80 expression in cells. Tubulin is a loading control. Data shown represent 2 independent experiments (right panel). (E) Accumulation of endogenous ZNF384 at 365 nm UV-A tracks in BrdU-sensitized U2OS cells following transfection with siLuc, siKU80 and siDNA-PKcs. Cells were fixed and immunostained 10 minutes after laser micro-irradiation. White triangles indicate irradiated regions. γ H2AX was used as a DNA damage marker (left panel). Quantification of endogenous ZNF384 and γ H2AX levels in laser tracks is presented as the mean \pm SEM of >180 cells acquired in 3 independent experiments (middle panel). Western blot analysis of KU80 and DNA-PKcs expression. Tubulin is a loading control. Data shown represent 2 independent experiments (right panel). (F) Accumulation of endogenous ZNF384 at 365 nm UV-A tracks in BrdU-sensitized wildtype (WT) and xrs-5 KO hamster cells. Cells were fixed and immunostained 10 minutes after laser micro-irradiation. White triangles indicate irradiated regions. γ H2AX was used as a DNA damage marker. (G) Quantification of F. Endogenous ZNF384 and γ H2AX levels in laser tracks are presented as the mean \pm SEM of >150 cells acquired in 3 independent experiments. (H) Kinetics of GFP-ZNF384 recruitment to 800 nm laser tracks in U2OS Flp-In/T-Rex ZNF384 KO cells treated for 1 hour with DNA-PKcs inhibitor prior to laser micro-irradiation. White triangles indicate irradiated regions (left panel). Quantification of GFP-ZNF384 in laser tracks is presented as the mean \pm SD from 2 independent experiments (right panel). (I) Accumulation of endogenous ZNF384 at 365 nm UV-A tracks in BrdU-sensitized U2OS cells treated for 1 hour with DNA-PKcs inhibitor prior to laser micro-irradiation. Cells were fixed and immunostained 10 minutes after laser micro-irradiation. White triangles indicate irradiated regions. γ H2AX was used as a DNA damage marker (left panel). Quantification of endogenous ZNF384 and γ H2AX levels in laser tracks is presented as the mean \pm SEM of >180 cells acquired in 3 independent experiments (right panel). Statistical significance was calculated with the two-tailed Student's t test, assuming unequal variances. Scale bar 5 μ m. (J) Western blot analysis of p-DNA-PKcs (S2056) levels in IR- and DNA-PKcs inhibitor-treated cells used in I. Cells were treated with DNA-PKi 1 hour before IR exposure. Blots were probed for p-DNA-PKcs (S2056), DNA-PKcs, γ H2AX. Tubulin and H3 are loading controls. Source data are provided as Source Data file.



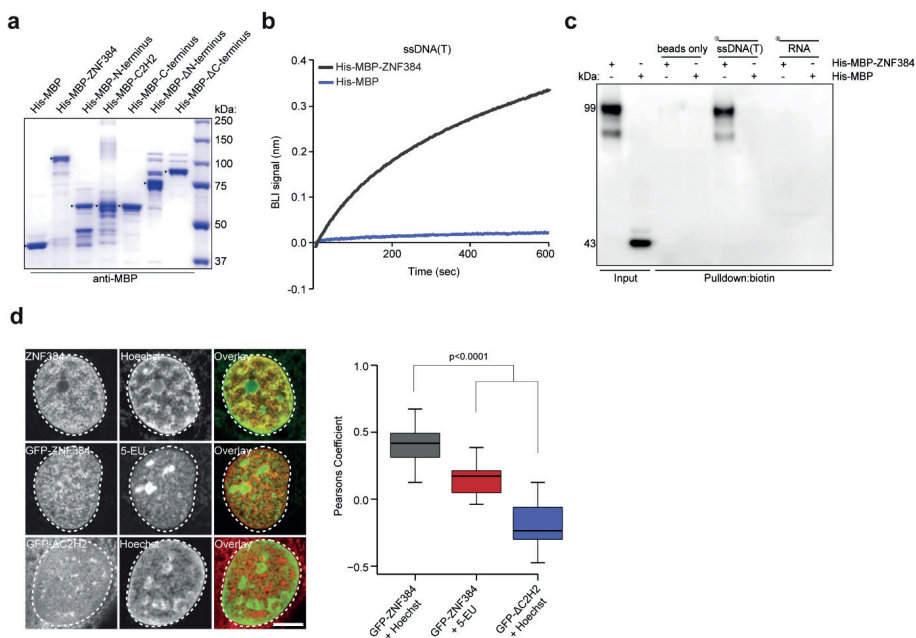
► **Supplementary Figure. 3 – related to Figure. 1. ZNF384 is recruited to DNA damage sites via PARP1/PAR.** (A) Accumulation of endogenous ZNF384 at 365 nm UV-A tracks in BrdU-sensitized U2OS cells treated for 1 hour with PARPi prior to laser micro-irradiation. Cells were fixed and immunostained 10 minutes after laser micro-irradiation. White triangles indicate irradiated regions. γ H2AX was used as a damage marker (left panel). Quantification of endogenous ZNF384 and γ H2AX levels in laser tracks is presented as the mean \pm SEM of >200 cells acquired in 3 independent experiments (right panel). (B) Western blot analysis of PAR levels in IR treated and PARPi treated cells used in Figure 2A and Figure S3A. Cells were treated with PARPi 1hr before the IR treatment. Tubulin is a loading control. Data shown represent 2 independent experiments. (C) γ H2AX accumulation at 365 nm UV-A tracks 10 minutes after DNA damage induction in BrdU-sensitized wildtype, PARP1 KO, PARP2 KO and PARP1/PARP2 KO U2OS cells. White triangles indicate irradiated regions (left panel). The mean \pm SEM of >180 cells from 3 independent experiments is shown (right panel). (D) Western blot analysis of PARP1 and PARP2 expression in cells from Figure 2B and Figure S3C. Tubulin is a loading control. Data shown represent 2 independent experiments. (E) Accumulation of endogenous ZNF384 at 365 nm UV-A tracks in BrdU-sensitized U2OS cells transfected with the indicated siRNAs. Cells were fixed and immunostained 10 minutes after laser micro-irradiation. White triangles indicate irradiated regions. γ H2AX was used as a damage marker (left panel). Quantification of endogenous ZNF384 and γ H2AX levels in laser tracks is presented as the mean \pm SEM of > 200 cells acquired in 3 independent experiments (right panel). (F) Western blot analysis of PARP3 expression in cells from Figure S3E. Tubulin is a loading control. Data shown represent 2 independent experiments. (G) Accumulation of endogenous KU80 at 365 nm UV-A tracks in BrdU-sensitized U2OS cells transfected with the indicated siRNAs. Cells were fixed and immunostained 10 minutes after laser micro-irradiation. White triangles indicate irradiated regions (left panel). Quantification of endogenous KU80 levels in laser tracks is presented as the mean \pm SEM of >120 cells acquired in 3 independent experiments (right panel). (H) As in G, except for PAR. (I) Pull-downs of GFP-ZNF384 and GFP-NLS under denaturing conditions in untreated and phleomycin (Phleo)-treated U2OS Flp-In/T-Rex cells expressing doxycycline (dox)-inducible GFP-ZNF384 or GFP-NLS. Cells were also treated with PARPi (Olaparib) for 1 hour prior to the phleomycin treatment. Blots were probed for PAR, PARP1 and GFP. Data shown represent 2 independent experiments. Statistical significance was calculated with the two-tailed Student's *t* test, assuming unequal variances. Scale bar 5 μ m. Source data are provided as Source Data file.



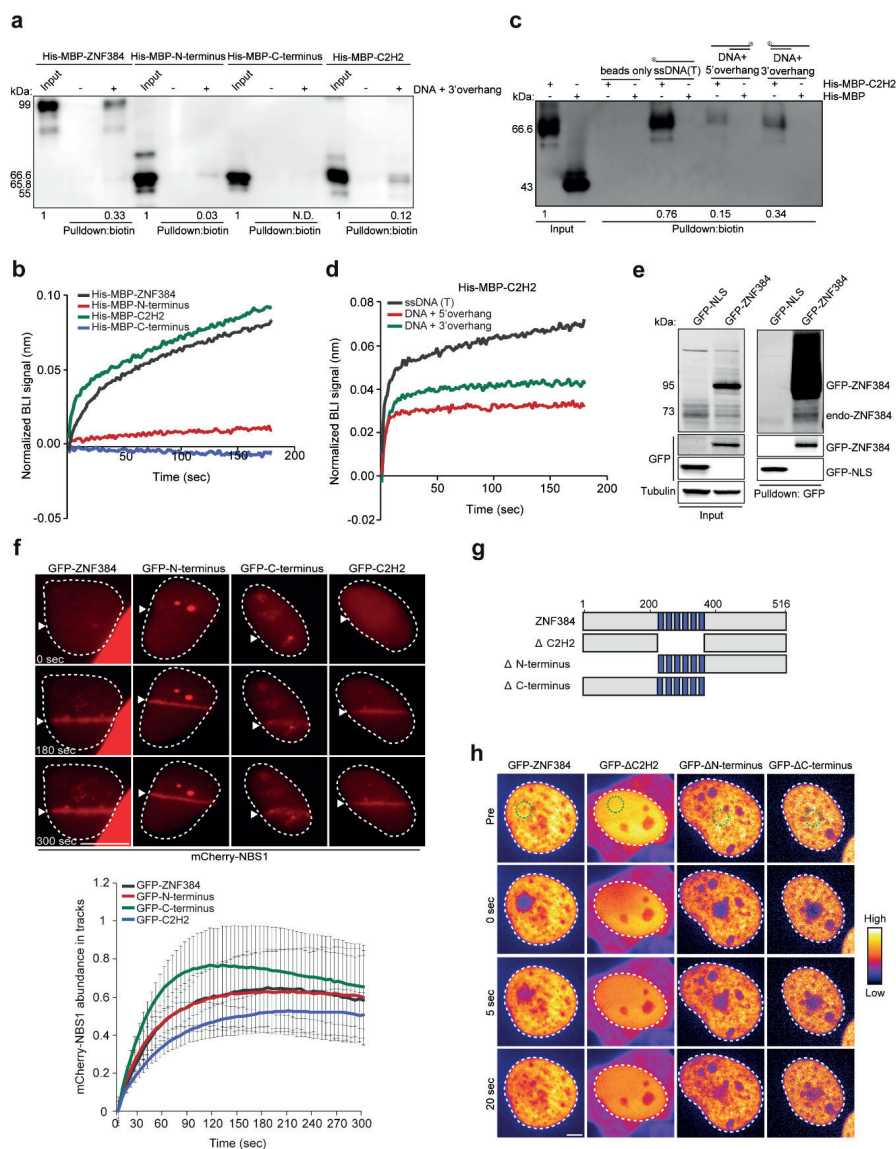
► **Supplementary Figure. 4 – related to Figure. 2. ZNF384 is recruited to DNA damage sites via PARP1/PAR dependent chromatin unfolding.** (A) Schematic of the fluorescence three-hybrid assay (F3H). Prior to laser irradiation, a GFP-tagged bait protein which is tethered to a genomically integrated LacO array through a LacI-GFP binding protein (LacO-trap) does not show enrichment of mCherry-PARP1 at the LacO array. After laser micro-irradiation, mCherry-PARP1 diffuses away from the site of damage in a PARylated state. If the tethered GFP-tagged bait protein can interact with PARylated PARP1 (bottom left), mCherry-PARP1 will enrich at the LacO array. If the tethered protein of interest does not interact with the tethered bait protein (bottom right), there is no enrichment of mCherry-PARP1 at the LacO array. (B) Western blot analysis of PAR levels in H_2O_2 and PARPi or PARGi treated cells used in Figure S4D. Cells were treated with 2 mM H_2O_2 for 10 min to induce PARylation. Blot was probed with panADPr. Actin is a loading control. Blots are representative of 3 independent replicates. (C) Fluorescence images of *in situ* PAR binding three-hybrid assays. LacI-GFP-macroH2A1.1 (GFP-macro) was tethered to a LacO array in Hoechst-sensitized cells co-expressing mCherry-PARP1 treated for 1 hour with PARPi or PARGi prior to 405 nm laser micro-irradiation. White triangles indicate irradiated regions. Inset shows the magnified LacO array. Insets are pseudocolored according to the look-up table displayed on the right. Scale bar 5 μ m. (D) The mean intensity of mCherry signal at the LacO array from 19-20 cells was quantified pre damage and 60 seconds post damage. Data shows mean intensity of the mCherry signal at the LacO array \pm SEM. Cells were treated for 1 hour with PARPi or PARGi prior to micro-irradiation. (E) Fluorescence images of *in situ* PAR binding three-hybrid assays. GFP-ZNF384 or GFP-macro was tethered to a LacO array in Hoechst-sensitized cells co-expressing mCherry-PARP1 prior to 405 nm laser micro-irradiation. White triangles indicate irradiated regions. Inset shows the magnified LacO array. Insets are pseudocolored according to the look-up table displayed on the right. (F) The mean intensity of mCherry signal at the LacO array from 12-15 cells was quantified pre damage and 60 seconds post damage. The boxplot limits correspond to the 25th and 75th percentiles and the center line in the box indicates the median value. The whiskers extend 1.5 times the interquartile range. P-values were calculated using the two-tailed Student's *t* test, assuming unequal variances. Scale bar 5 μ m. Source data are provided as Source Data file.



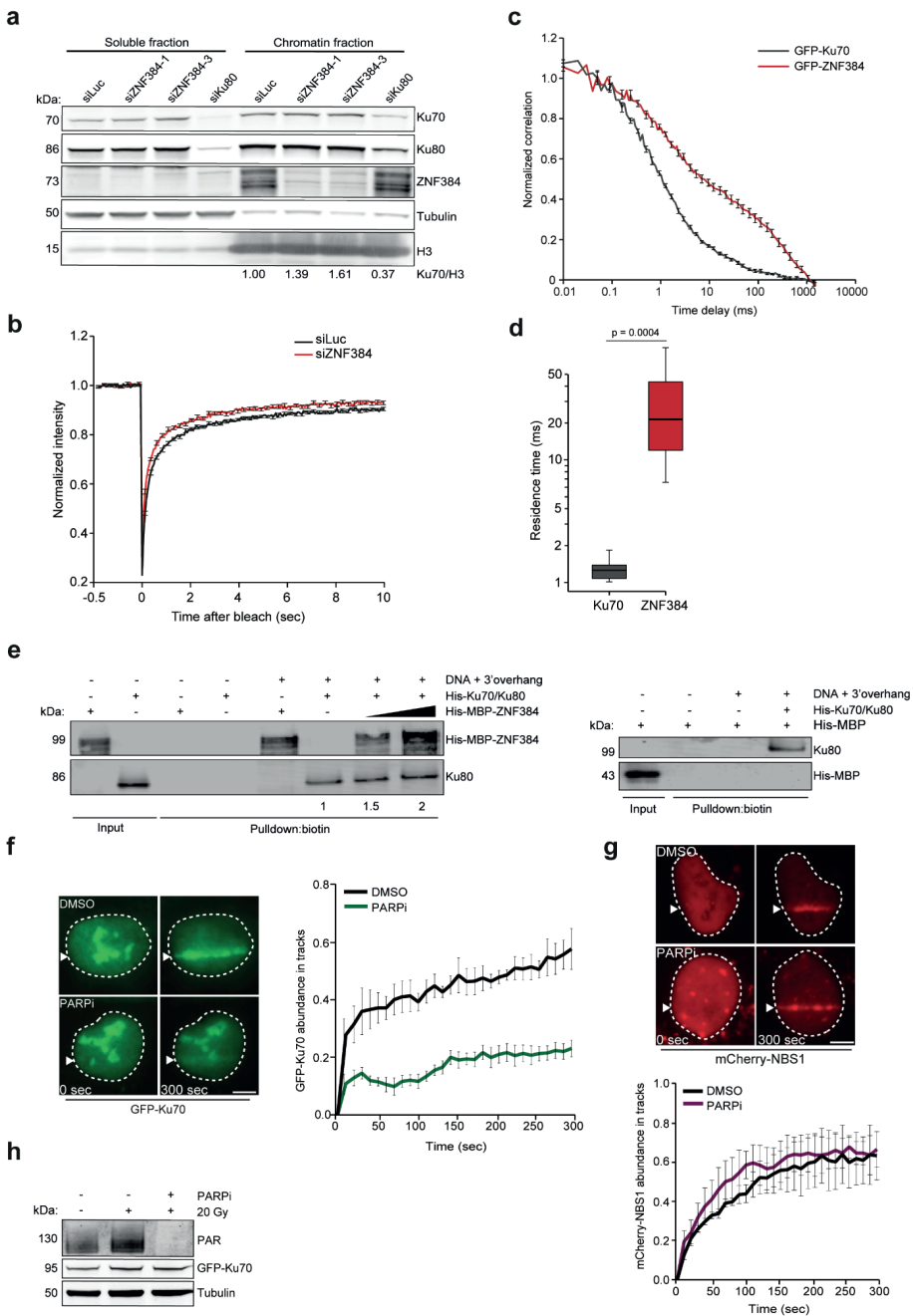
► **Supplementary Figure. 5 – related to Figure. 2. ZNF384 is recruited to DNA damage sites via PARP1/PAR dependent chromatin unfolding.** (A) Confocal images showing accumulation of GFP-WWE at sites of 405 nm laser micro-irradiation in Hoechst-sensitized U2OS cells. Cells were left untreated or treated with PARPi or PARPi and PARGi 240 seconds after DNA damage induction. White triangles indicate irradiated regions. Scale bar 5 μ m. (B) Boxplot showing the accumulation of GFP-WWE at 450 seconds post irradiation from cells in A. Boxplots show the first, median and third quartiles from a representative of 3 independent replicates. The whiskers extend 1.5 times the interquartile range. P-values were calculated using the two-tailed unpaired Student's *t* test, assuming unequal variances. (C) Chromatin relaxation was measured for each of the overexpression conditions from Figure 2G. The mean \pm SEM from 13-16 cells from a representative of 3 independent experiments is shown. (D) Western blot analysis of the indicated proteins in soluble and chromatin fractions from untreated and phleomycin treated U2OS cells. H3 is the loading control. γ H2AX is a DNA damage marker. A representative experiment is shown. (E) Quantification of ZNF384 levels on chromatin in cells from D. H3 is a loading control, which was used for normalization of ZNF384 levels on chromatin. The mean \pm SEM from 4 independent experiments is shown. P-values were calculated using the Student's *t* test, assuming unequal variances. (F) Representative images of Hoechst-sensitized U2OS Flp-In/T-Rex *ZNF384* KO cells in which FRAP measurements were performed to assess the local turnover of GFP-ZNF384 at DNA damage sites. DNA damage was induced in the region indicated with a dashed line using 405 laser micro-irradiation. Subsequent FRAP was induced in a subarea within the damaged region, as indicated with an unbroken line. Images are pseudocolored according to the look-up table displayed on the right. Scale bar 4 μ m. (G) Normalized FRAP curves from F. Data show mean \pm SEM from 14 cells per condition from a representative of 3 independent replicates (H) Boxplot showing the characteristic recovery times estimated from the FRAP curves shown in F. The boxplot limits correspond to the 25th and 75th percentiles and the center line in the box indicates the median value. The whiskers extend 1.5 times the interquartile range. P-values were calculated using the two-tailed paired Student's *t* test. (I) Normalized FRAP curves of the GFP-tagged DNA binding domain BZIP from the transcription factor C-EBPa and DNA damage induction in U2OS cells (left panel). Normalized FRAP curves of GFP-tagged CHD4 and DNA damage induction in U2OS cells (right panel). (J) Normalized FRAP curves of GFP-KU70 and DNA damage induction in RPE1-hTERT cells. The mean \pm SD is shown from 14 cells per condition from a representative of 2 independent replicates. Source data are provided as Source Data file.



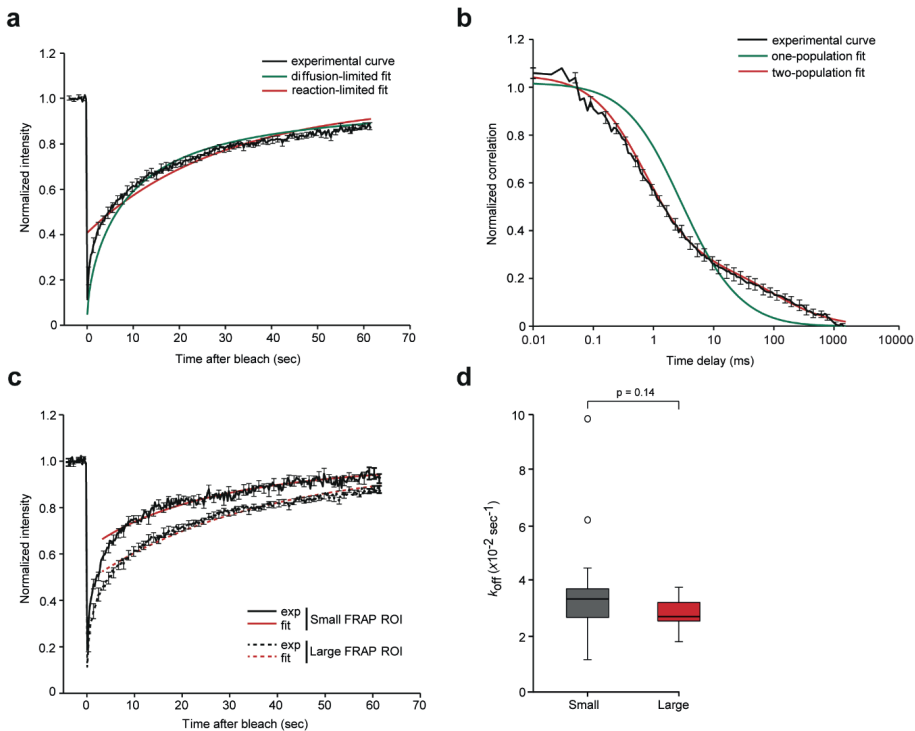
Supplementary Figure 6 – related to Figure 3. ZNF384 is recruited to sites of DNA damage in manner dependent on its ability to bind DNA. (A) SDS-PAGE analysis of the indicated purified His-MBP-tagged proteins. Data shown represent 2 independent experiments. (B) DNA binding by His-MBP-ZNF384 and His-MBP to biotinylated T-rich ssDNA (ssDNA(T)) by BLI. (C) Pull-downs of the indicated biotinylated DNA or RNA substrates in the presence of His-MBP-ZNF384 or His-MBP. Blots were probed for MBP. Data shown represent 2 independent experiments. (D) Representative images of U2OS Flp-In/T-Rex *ZNF384* KO cells expressing either GFP-tagged full-length ZNF384 or ΔC2H2. Cells were co-stained with Hoechst or 5-Ethynyl Uridine (5-EU) to assess their colocalization with DNA or RNA (left panel). The levels of colocalization between ZNF384 or ΔC2H2 and DNA or RNA were assessed using the Pearson coefficient (right panel). The mean \pm SD is shown from >23 cells per condition. The boxplot limits correspond to the 25th and 75th percentiles and the center line in the box indicates the median value. The whiskers extend 1.5 times the interquartile range. For GFP-ZNF384 + Hoechst vs GFP-ZNF384 + 5-EU, $p = 7.1156 \times 10^{-7}$. For GFP-ZNF384 + Hoechst vs GFP-ΔC2H2 + Hoechst, $p = 4.027 \times 10^{-12}$. P-values were calculated using the two-tailed unpaired Student's *t* test, assuming unequal variances. Source data are provided as Source Data file.



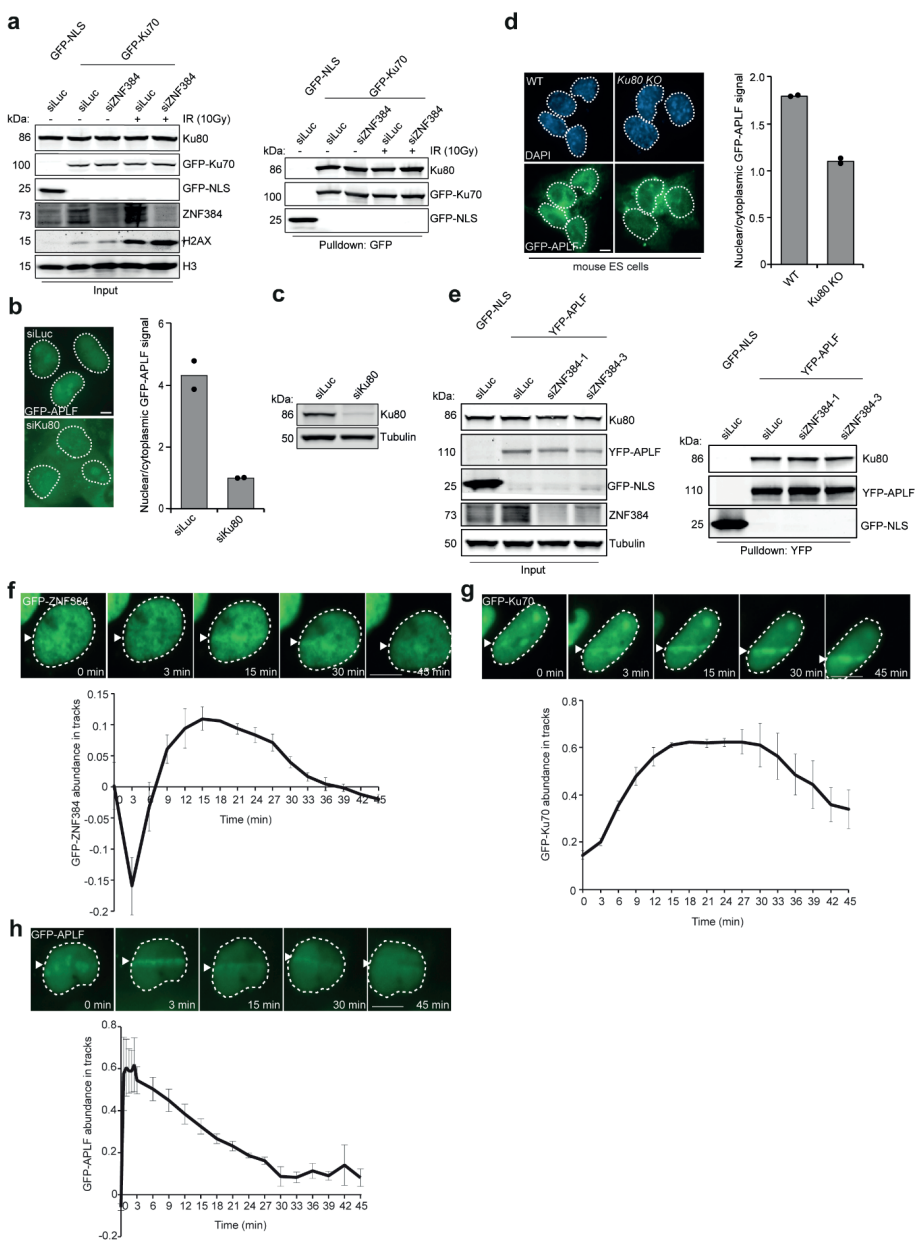
► **Supplementary Figure. 7 – related to Figure. 3. ZNF384 is recruited to sites of DNA damage via its C2H2 domain.** (A) DNA pulldowns of biotinylated DNA with a 3' overhang in the presence of the indicated ZNF384 proteins. Blots were probed for MBP. For each protein, input signals were used for normalization of the pulldown signals. The mean of 2 independent experiments is indicated below the blot. A representative experiment is shown. N.D. = not detectable. (B) DNA binding by the indicated ZNF384 proteins to DNA with a 3' overhang as measured by BLI. Quantification of the data is plotted on a time scale and normalized to His-MBP alone. (C) DNA pulldowns of biotinylated T-rich ssDNA (ssDNA(T)), biotinylated DNA with a 5' overhang or biotinylated DNA with a 3' overhang in the presence of His-MBP-C2H2 or His-MBP (control). Blots were probed for MBP. His-MBP-C2H2 pulldown signals were normalized to that in the input, which was set to 1. The mean from 3 independent experiments is indicated below the blot. His-MBP was not detectable in pulldowns. A representative experiment is shown. (D) DNA binding of His-MBP-C2H2 to biotinylated T-rich ssDNA (ssDNA(T)), biotinylated DNA with a 5' overhang or biotinylated DNA with a 3' overhang as measured by BLI. Quantification of the data is plotted on a time scale and normalized to His-MBP (control). (E) Pulldowns of the indicated GFP-fusion proteins in U2OS Flp-In/T-Rex cells. Blots were probed for GFP, ZNF384 and Tubulin. Data shown represent 2 independent experiments. (F) Live cell imaging of mCherry-NBS1 to 365 nm UV-A tracks in BrdU- sensitized *ZNF384* KO U2OS Flp-In/T-Rex cells. mCherry-NBS1, which was co-expressed with GFP-ZNF384 proteins, served as a DNA damage marker for Figure 3D. Representative images are shown. White triangles indicate irradiated regions. Scale bars 10 μ m (upper panel). Quantification of the data is shown as mean \pm SEM from 30-40 cells (lower panel). (G) Schematic representation of full-length ZNF384 and three deletion mutants (Δ C2H2, Δ N-terminus and Δ C-terminus). (H) Representative images of cells from Figure 3E in which the FRAP measurements are performed to assess the local dynamics of the indicated GFP-ZNF384 constructs. FRAP area is indicated with a dashed line. Images are pseudocolored according to the look-up table displayed on the bottom. Scale bar: 4 μ m. Source data are provided as Source Data file.



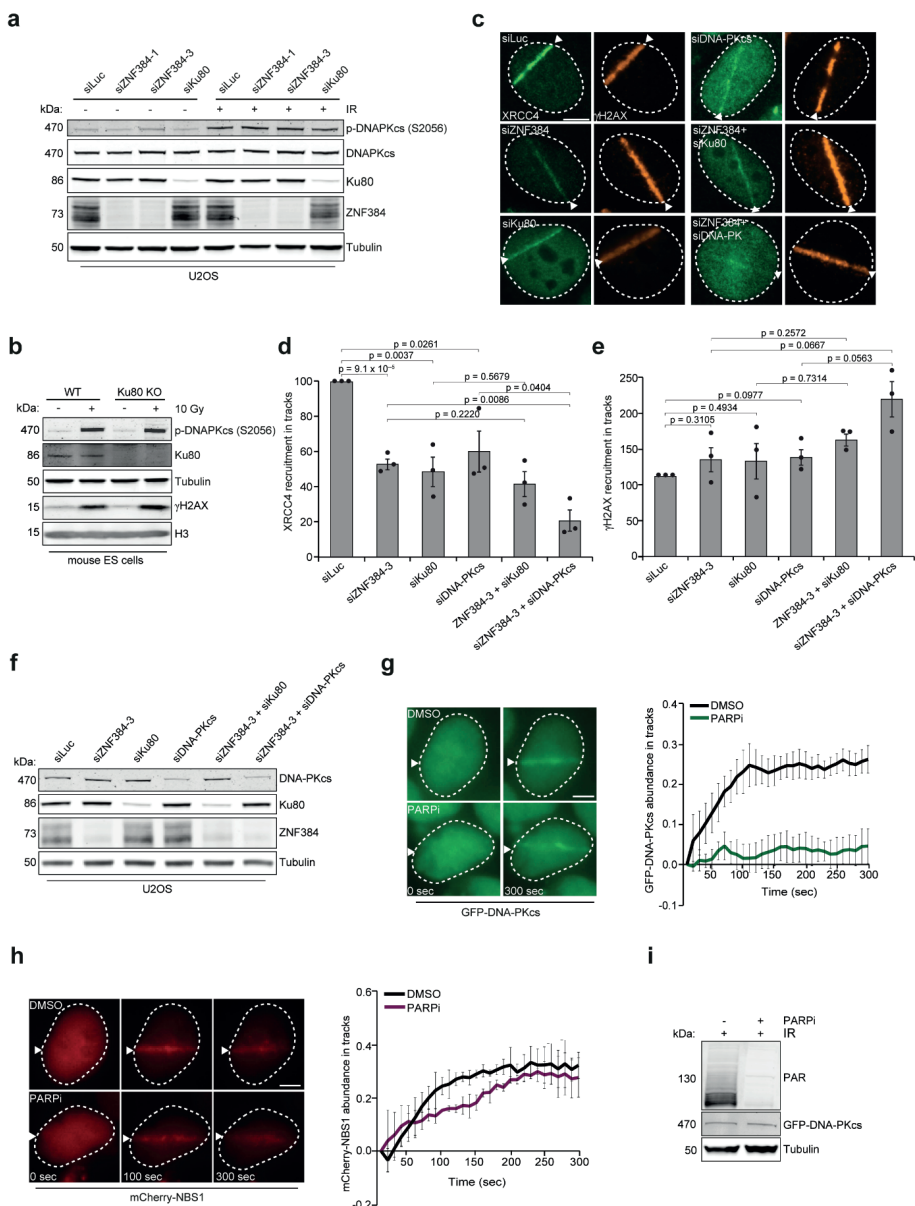
► **Supplementary Figure. 8 – related to Figure. 4. ZNF384 modulates the loading of KU70/KU80 at DNA damage sites.** (A) Western blot analysis of the indicated proteins in soluble and chromatin fractions from U2OS cells. Blots were probed for the indicated proteins. H3 and Tubulin are loading controls. A representative experiment is shown. KU70 levels in chromatin were first normalized to H3 levels. KU70/H3 ratios were then normalized to that for siLuc, which was set to 1. Quantifications are shown as the mean from 2 independent experiments. (B) Normalized FRAP curves of GFP-KU70 in RPE-hTERT cells transfected with the indicated siRNAs in the absence of DNA damage. The mean \pm SD is shown from 20-21 cells per condition. (C) Normalized FCS autocorrelation curves of GFP-KU70 in RPE1-hTERT cells and GFP-ZNF384 in U2OS cells in the absence of DNA damage. The mean \pm SEM is shown from 10-16 cells analyzed per condition. (D) Boxplot showing the residence times of GFP-KU70 and GFP-ZNF384 in RPE1-hTERT and U2OS cells, respectively, as measured by FCS. 10-15 cells were analyzed per condition. The boxplot limits correspond to the 25th and 75th percentiles and the center line in the box indicates the median value. The whiskers extend 1.5 times the interquartile range. P-values were calculated using the two-tailed unpaired Student's *t* test, assuming unequal variances. (E) DNA pulldowns of biotinylated DNA with a 3' overhang in the presence of His-KU70/KU80, His-MBP-ZNF384 or His-MBP (control) alone or His-KU70/KU80 in combination with His-MBP-ZNF384 or His-MBP (control). Blots were probed for MBP and KU80. KU80 pulldown signals were normalized to that in the pulldown lacking His-MBP-ZNF384, which was set to 1. The mean from 4 independent experiments is indicated below the blot. His-MBP was not detectable in pulldowns. (F) GFP-KU70 recruitment to 365 nm UV-A tracks in cells treated with PARPi for 1 hour before laser micro-irradiation. White triangles indicate irradiated regions (left panel). Quantification of the data is presented as the mean \pm SEM of >100 cells acquired in 3 independent experiments (right panel). (G) As in F, except for mCherry-NBS1. (H) Western blot analysis of PAR levels, which likely reflect PARP1 autoPARylation, in phleomycin- and PARPi-treated cells from F and G. Cells were treated with PARPi for 1 hour before IR treatment. Blots were probed for PAR, GFP and Tubulin. Tubulin is a loading control. Data shown represent 2 independent experiments. Statistical significance was calculated using the two-tailed unpaired Student's *t* test, assuming unequal variances. Scale bar 5 μ m. Source data are provided as Source Data file.



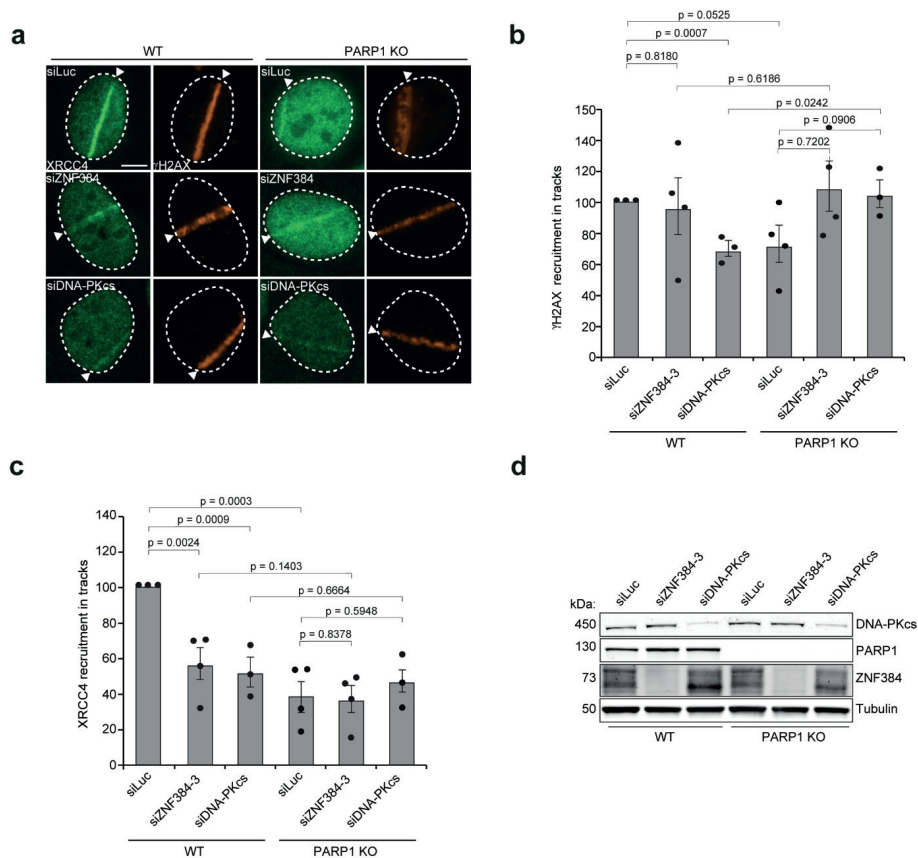
Supplementary Figure. 9 – related to Figure. 4. ZNF384 facilitates the recruitment rather than the retention of KU70/KU80 at sites of DNA damage. (A) FRAP curves of GFP-KU70 at the DNA lesions fitted with two alternative models: i) a diffusion-limited model which assumes that KU interacts only very transiently with DNA at the sites of damage, and ii) a reaction-limited model which is valid if the fluorescence recovery is limited by the long lifetime of the interaction between KU and the DNA lesions [1]. The mean \pm SEM is shown from 15 cells from a representative of 3 independent experiments is shown. (B) FCS curves of GFP-KU70 at the DNA lesions fitted with models assuming either one or two population dynamics. Based on the 2-population fit, the fast population displays a characteristic diffusion time of 590 ± 70 μ seconds within the confocal volume. Given that the molecular weight of the GFP-tagged KU70/KU80 complex (180 kDa) is ~ 6 times larger than GFP only, and that GFP shows a diffusion time of approximately 300 μ seconds when diffusing through the nucleus [2], the Stokes-Einstein equation predicts that the diffusion time on an unbound KU70/KU80 complex should be equal to $300 \times 6^{1/3} = 550$ μ seconds. Therefore, it seems reasonable to assume that the fast population of KU seen by FCS corresponds to freely diffusing KU complexes. The mean \pm SEM is shown from 10 cells from a representative of 3 independent experiments. (C) FRAP curves of GFP-KU70 at the DNA lesions obtained for two different bleaching area and fitted with a reaction-limited model for the timepoints at more than 3 seconds post photobleaching. The mean \pm SEM is shown from 15 cells from a representative of 3 independent experiments is shown. (D) k_{off} parameters estimated from the reaction-limited model for the two different sizes of bleached area from C. The mean \pm SEM is shown from 15 cells from a representative of 3 independent experiments is shown. The boxplot limits correspond to the 25th and 75th percentiles and the center line in the box indicates the median value. The whiskers extend 1.5 times the interquartile range. P-values were calculated using the two-tailed unpaired Student's *t* test, assuming unequal variances. Source data are provided as Source Data file.



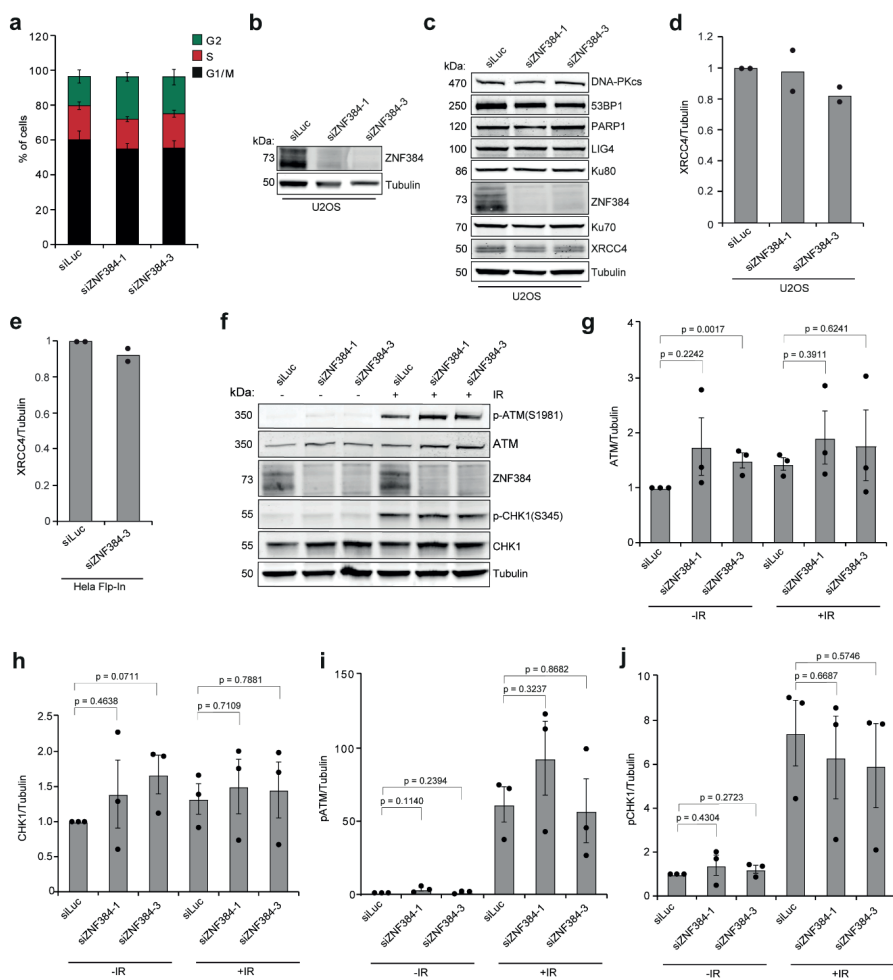
► **Supplementary Figure. 10 – related to Figure. 5 and 6. ZNF384 is dispensable for cNHEJ complex stability.** (A) Pull-downs of the indicated GFP fusion proteins in IR treated RPE-hTERT cells transfected with indicated siRNAs. Blots were probed for GFP, KU80, ZNF384, γ H2AX and H3. Data shown represent 2 independent experiments. (B) Nuclear localization of GFP-APLF in U2OS Flp-In/T-Rex cells expressing doxycycline (dox)-inducible GFP-APLF transfected with the indicated siRNAs (left panel). Quantification of the data is presented as the mean of >200 cells acquired in 2 independent experiments (right panel). (C) Western blot analysis of KU80 in cells from B. Tubulin is a loading control. Data shown represent 2 independent experiments. (D) Nuclear localization of GFP-APLF in wildtype and *Ku80*^{-/-} mouse embryonic stem (ES) cells (left panel). Quantification of the data is presented as the mean of >60 cells acquired in 2 independent experiments (right panel). (E) Pull-downs of the indicated GFP fusion proteins transfected with indicated siRNAs in U2OS cells. Blots were probed for GFP, KU80, ZNF384 and tubulin. Data shown represent 2 independent experiments. (F) Kinetics of GFP-ZNF384 recruitment to 365 nm UV-A tracks in BrdU-sensitized U2OS Flp-In/T-Rex *ZNF384* KO cells. White triangles indicate irradiated regions (left panel). Quantification of GFP-ZNF384 is presented as the mean \pm SD from >120 cells acquired in 2 independent experiments (right panel). (G) Kinetics of GFP-KU70 recruitment to 365 nm UV-A tracks in BrdU-sensitized RPE1-hTERT cells. White triangles indicate irradiated regions. (left panel). Quantification of GFP-KU70 is presented as the mean \pm SD from >120 cells acquired in 2 independent experiments (right panel). (H) Kinetics of GFP-APLF recruitment to 365 nm UV-A tracks in BrdU-sensitized U2OS Flp-In/T-Rex GFP-APLF cells. White triangles indicate irradiated regions (left panel). Quantification of GFP-APLF is presented as the mean \pm SD from <120 cells acquired in 2 independent experiments (right panel). Statistical significance was calculated with the two-tailed unpaired Student's *t* test, assuming unequal variances. Scale bar 5 μ m. Source data are provided as Source Data file.



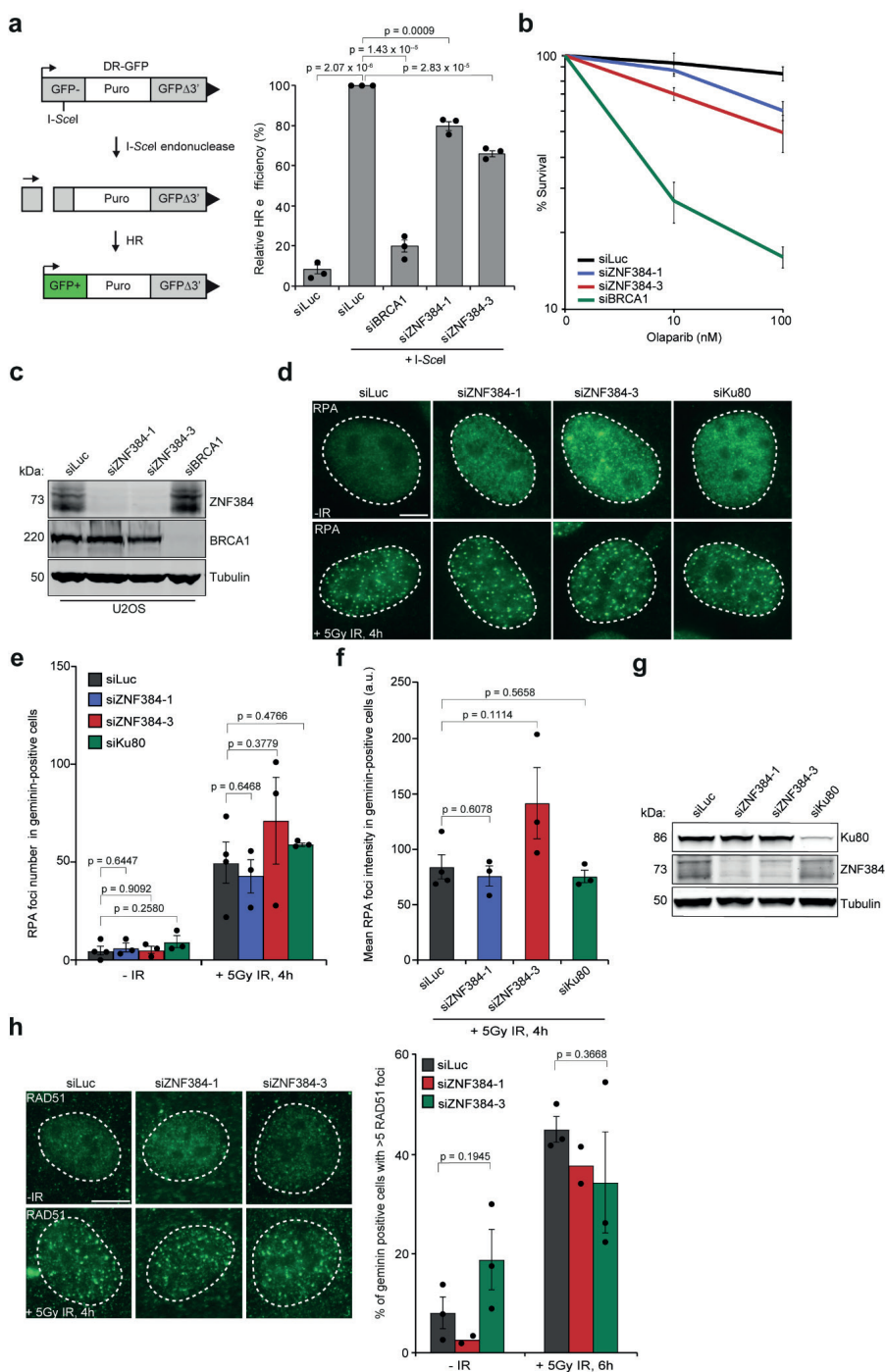
► **Supplementary Fig. 11 – related to Fig. 6. ZNF384 promotes recruitment of cNHEJ proteins independently of DNA-PKcs.** (A) Western blot analysis of DNA-PK activation 1 hour after 10 Gy of irradiation radiation (IR) in U2OS cells transfected with the indicated siRNAs. Blots were probed for p-DNA-PKcs (S2056), DNA-PKcs, KU80 and ZNF384. Tubulin is a loading control. Data shown represent 3 independent experiments. (B) Western blot analysis of DNA-PK activation 1 hour after 10 Gy of irradiation radiation (IR) in wildtype and *Ku80*^{-/-} mouse embryonic stem cells. Blots were probed for p-DNA-PKcs (S2056), KU80 and γ H2AX. H3 and tubulin are loading controls. Data shown represent 2 independent experiments. (C) Endogenous XRCC4 recruitment to 365 nm UV-A tracks 10 minutes after damage induction in U2OS cells transfected with the indicated siRNAs. γ H2AX is a damage marker. White triangles indicate irradiated regions. (D) XRCC4 quantification of C. Data shows the mean \pm SEM of >150 cells acquired in 3 independent experiments (E) γ H2AX quantification of C. The mean \pm SEM from 3 independent experiments is shown. Data were normalized to siLuc, which was set to 100%. (F) Western blot analysis of DNA-PKcs, KU80, ZNF384, γ H2AX and Tubulin in cells from C. Tubulin is a loading control. Data shown represent 2 independent experiments. (G) GFP-DNA-PKcs recruitment to 365 nm UV-A tracks in BrdU-sensitized HCT116 cells treated with PARPi for 1 hour before laser micro-irradiation. White triangles indicate irradiated regions (left panel). Quantification of the data is presented as the mean \pm SEM of >100 cells acquired in 3 independent experiments (right panel). (H) As in G, except for mCherry-NBS1. (I) Western blot analysis of PAR levels in IR- and PARPi -treated cells from G. Cells were treated with PARPi for 1 hour before IR treatment. Blots were probed for PAR, GFP and Tubulin. Tubulin is a loading control. Data shown represent 2 independent experiments. Statistical significance was calculated with the two-tailed unpaired Student's *t* test, assuming unequal variances. Scale bar 5 μ m. Source data are provided as Source Data file.



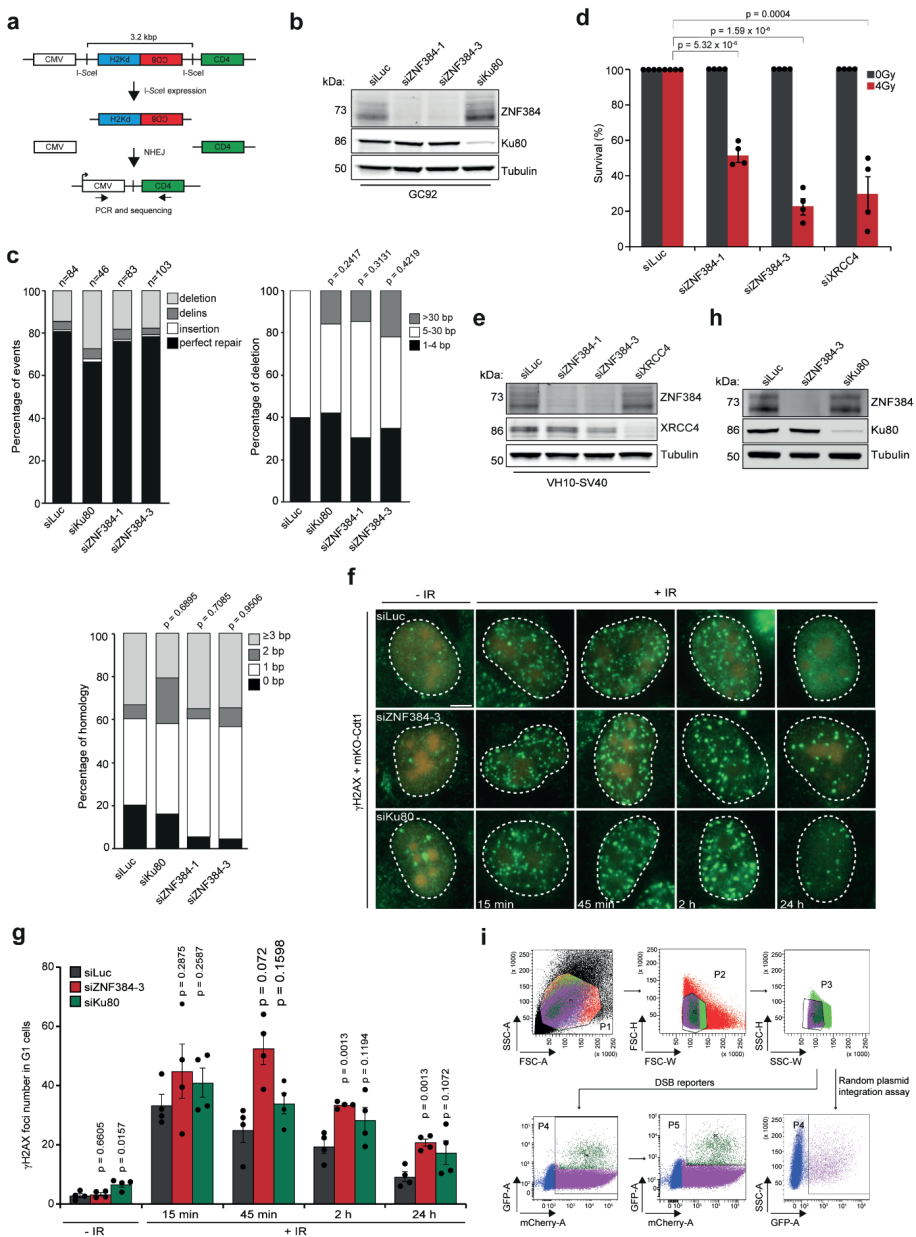
Supplementary Figure. 12 – related to Figure. 6. ZNF384 and PARP1, as well as DNA-PKcs and PARP1, function epistatically in cNHEJ. (A) Endogenous XRCC4 recruitment to 365 nm UV-A tracks in BrdU-sensitized U2OS cells transfected with the indicated siRNAs. Cells were fixed and immunostained 10 minutes after laser micro-irradiation. White triangles indicate irradiated regions. γ H2AX is a damage marker. (B) γ H2AX quantification of A. Data shows the mean \pm SEM of >240 cells acquired in 4 independent experiments. (C) XRCC4 quantification of A. The mean \pm SEM from 3 independent experiments is shown. Data were normalized to siLuc, which was set to 100%. (D) Western blot analysis of ZNF384, DNA-PKcs and PARP1 in cells from A. Tubulin is a loading control. Data shown represent 2 independent experiments. Statistical significance was calculated with the two-tailed unpaired Student's *t* test, assuming unequal variances. Scale bar 5 μ m. Source data are provided as Source Data file.



► **Supplementary Figure. 13 – related to Figure. 7. ZNF384 promotes efficient NHEJ independently of transcription.** (A) Cell cycle profile of the indicated siRNA-transfected U2OS cells. The fraction of G1-, S- and G2-phase cells was determined by propidium iodide staining and FACS analysis. >30000 cells per condition were analyzed. Data show mean \pm SEM from 3-4 independent experiments. (B) Western blot analysis of ZNF384 expression in U2OS cells from A. Tubulin is a loading control. Data shown represent 2 independent experiments. (C) Western blot analysis of the expression of NHEJ factors in siRNA transfected ZNF384 knockdown U2OS cells. Blots were probed for ZNF384, 53BP1, DNA-PKcs, KU80, KU70, PARP1, XRCC4 and LIG4. Tubulin is a loading control. (D) Quantification of XRCC4 expression in cells from C. Tubulin is a loading control, which was used for normalization of XRCC4 expression. The mean \pm SD from 2 independent experiments is shown. Data were normalized to WT + siLuc, which was set to 1. (E) Quantification of XRCC4 expression in cells from Figure 7E. Tubulin is a loading control, which was used for normalization of XRCC4 expression. The mean \pm SD from 2 independent experiments is shown. Data were normalized to WT + siLuc, which was set to 1. (F) Western blot analysis of IR-induced ATM phosphorylation (p-ATM) at Ser1981 and CHK1 phosphorylation (p-CHK1) at Ser345. Cells were collected 1 hour after exposure to 10 Gy of IR. Blots were also probed for ATM, ZNF384, CHK1 and Tubulin. Tubulin is a loading control. A representative blot from 3 independent experiments is shown. (G) Quantification of ATM expression in cells from F. Tubulin was used for normalization of ATM expression. The mean \pm SEM from 3 independent experiments is shown. Data were normalized to siLuc - IR, which was set to 1. (H) As in G, except for CHK1. (I) As in G, except for pATM. (J) As in G, except for pCHK1. Statistical significance was calculated with the two-tailed unpaired Student's *t* test, assuming unequal variances. Source data are provided as Source Data file.



► **Supplementary Figure. 14 – related to Figure. 7. ZNF384 is dispensable for HR.** (A) Schematic of the DR-GFP reporter for HR (left panel). Quantification of HR efficiencies in 3 independent DR-GFP- U2OS transfected cells with the indicated siRNAs. I-SceI transfection was corrected by co-transfection with mCherry expression vector. The mean \pm SEM from 3 independent experiments is shown (right panel). (B) Clonogenic survival of U2OS cells transfected with the indicated siRNAs following treatment with the PARPi. The mean \pm SEM from 3 independent experiments is shown. (C) Western blot analysis of ZNF384 and BRCA1 expression in U2OS cells. Tubulin is a loading control. Data shown represent 2 independent experiments. (D) RPA foci formation in U2OS cells transfected with the indicated siRNAs. Cells were exposed to 5 Gy of IR and foci were scored after 4 hours. (E) Quantification of RPA foci formation in cells from D. Foci were quantified in immuno-stained, geminin-positive S/G2 phase cells. The mean \pm SEM from >200 cells from 3-4 independent experiments is shown. (F) As in E, except that RPA foci intensity was measured. (G) Western blot analysis of ZNF384 and KU80 expression in cells from D. Tubulin is a loading control. (H) RAD51 foci formation in U2OS cells transfected with the indicated siRNAs. Cells were exposed to 5 Gy of IR and foci were quantified after 6 hours (left panel) The mean \pm SEM from >300 cells from 2-3 independent experiments is shown. Foci were quantified in immuno-stained, geminin-positive S/G2 phase cells (right panel). Statistical significance was calculated with the two-tailed unpaired Student's *t* test, assuming unequal variances. Scale bar 5 μ m. Source data are provided as Source Data file.



► **Supplementary Fig. 15 – related to Fig. 7. ZNF384 promotes DSB repair via cNHEJ.** (A) Schematic of the GC92 reporter for NHEJ. (B) Western blot analysis of ZNF384 and KU80 expression in GC92 fibroblasts. Tubulin is a loading control. Data shown represent 2 independent experiments. (C) Mutational signatures (top left panel, deletion sized (top right panel) and microhomology usage (in case of deletion formation) (bottom panel) at repair junctions in GC92 reporter for NHEJ. GC92 cells were transfected with the indicated siRNAs and I-SceI expression vector. Repair junctions were amplified by PCR and Sanger-sequenced. (D) Clonogenic survival of VH10-SV40 cells transfected with the indicated siRNAs and exposed to 4 Gy of IR. The mean \pm SEM from 4 independent experiments is shown. P-values were calculated using the two-tailed unpaired Student's *t* test, assuming unequal variances. (E) Western blot analysis of ZNF384 and XRCC4 expression in cells used in D. Tubulin is a loading control. Data shown represent 2 independent experiments. (F) γ H2AX foci formation (green) in stable Monomeric Kusabira-Orange (mKO)-Cdt1 expressing U2OS cells transfected with the indicated siRNAs. Cells were exposed to 2 Gy of IR and foci were scored after 15 minutes, 45 minutes, 2 hours and 24 hours. (G) Quantification of γ H2AX foci formation in Cdt1-positive G1 phase cells from F. The mean \pm SEM from 2-4 independent experiments. Statistical significance was calculated with the two-tailed unpaired Student's *t*-test, assuming unequal variances. (H) Western blot analysis of ZNF384 and KU80 expression in cells from F. Tubulin is a loading control. Data shown represent 2 independent experiments. (I) Gating strategy for flow cytometric analysis of cells for DR-GFP and EJ5- GFP reporter assays, as well as random plasmid integration assays. Scale bar 10 μ m. Source data are provided as a Source Data file.

[illegible]

HADA29P3R3	Codon frame 3	51	0.51	6	6	6	292	292	41.9	0	481	1.2E+09	59	G23212	G23212	27.69	27.21	27.00	27.90	28.30		
HADA02J301	Nucleoside diphosphate	NME1	0.80	0.49	7	7	3	36	36	82.842	0	21.8	1.1E+09	58	G23212	G23212	27.83	27.95	28.30	28.40	28.23	
HADA03P3R3	Haplogroup node	HNNP3	1.79	0.49	21	21	21	388	388	88.7	17.50	1.23	5.3E+08	154	HADA03P3R3	HADA03P3R3	28.99	29.39	30.07	30.17	30.38	
HADA03P3R3	Codon frame	NAK1	0.45	0.48	4	4	4	187	187	61.7	0	1.13	1.1E+09	57	HADA03P3R3	HADA03P3R3	27.88	27.88	27.25	27.08	27.91	
HADA03P3R3	Codon frame	NAK1	0.47	0.48	4	4	4	171	171	60.977	0	1.13	1.1E+09	57	HADA03P3R3	HADA03P3R3	27.88	27.88	27.25	27.08	27.91	
HADA03P3R3	Phosphatidylcholine	PC2	0.52	0.47	3	3	3	53	53	53.785	0	0.887	8.0E+08	56	HADA03P3R3	HADA03P3R3	26.28	26.27	24.23	24.28	24.38	
HADA03P3R3	Phosphatidylcholine	PC2	0.50	0.47	2	2	2	57	57	57.7	0	0.887	8.0E+08	56	HADA03P3R3	HADA03P3R3	26.28	26.27	24.23	24.28	24.38	
HADA03P3R3	14-3-3 protein	YH98	0.48	0.46	6	6	2	231	93	80.302	0	1.03	2.4E+08	4	HADA03P3R3	HADA03P3R3	25.29	25.28	25.68	25.38	25.31	
HADA03P3R3	14-3-3 protein	YH98	0.47	0.46	6	6	2	231	93	80.302	0	1.03	2.4E+08	4	HADA03P3R3	HADA03P3R3	25.29	25.28	25.68	25.38	25.31	
HADA03P3R3	Tubulin beta chain	YH98	0.48	0.44	16	3	3	225	65	65.391	0	1.06	3.2E+08	4	HADA03P3R3	HADA03P3R3	25.29	25.28	25.68	25.38	25.31	
HADA03P3R3	14-3-3 protein	YH98	0.48	0.44	7	4	4	29	186	186	72.4	0	5.23	6.8E+08	2	HADA03P3R3	HADA03P3R3	27.71	27.70	27.96	27.37	27.26
HADA03P3R3	Vibrio	VBI	0.17	0.43	37	36	34	788	743	72.634	0	0.33	2.8E+08	278	HADA03P3R3	HADA03P3R3	31.88	31.22	31.26	30.88	31.74	
HADA03P3R3	Vibrio	VBI	0.17	0.43	37	36	34	788	743	72.634	0	0.33	2.8E+08	278	HADA03P3R3	HADA03P3R3	31.88	31.22	31.26	30.88	31.74	
HADA03P3R3	Phosphatidylcholine	PC2	0.52	0.47	3	3	3	53	53	53.785	0	0.887	8.0E+08	56	HADA03P3R3	HADA03P3R3	26.28	26.27	24.23	24.28	24.38	
HADA03P3R3	Phosphatidylcholine	PC2	0.52	0.47	3	3	3	56	56	56.634	0	0.887	2.2E+08	57	HADA03P3R3	HADA03P3R3	25.62	25.62	25.50	25.52	25.48	
HADA03P3R3	Tubulin alpha chain	RAN1	0.65	0.40	12	12	12	381	381	58.608	0	0.478	1.3E+09	57	HADA03P3R3	HADA03P3R3	27.07	27.06	26.88	27.17	26.97	
HADA03P3R3	Tubulin alpha chain	RAN1	0.65	0.40	12	12	12	381	381	58.608	0	0.478	1.3E+09	57	HADA03P3R3	HADA03P3R3	27.07	27.06	26.88	27.17	26.97	
HADA03P3R3	Phosphatidylcholine	PC2	0.52	0.47	5	5	5	16	16	16.433	0	0.206	2.7E+08	4	HADA03P3R3	HADA03P3R3	25.36	25.32	25.16	25.31	25.49	
HADA03P3R3	ICG Kunitz-type cysteine	KRT6	0.53	0.39	16	15	10	4	423	321	48.057	0	1.574	2.7E+09	4	HADA03P3R3	HADA03P3R3	28.35	28.31	28.62	28.60	28.41
HADA03P3R3	ICG Kunitz-type cysteine	KRT6	0.64	0.39	11	11	7	389	389	247	28.788	0	1.83	1.7E+09	50	HADA03P3R3	HADA03P3R3	36.02	36.28	36.07	36.23	36.39
HADA03P3R3	ICG Kunitz-type cysteine	KRT6	0.64	0.39	11	11	7	389	389	247	28.788	0	1.83	1.7E+09	50	HADA03P3R3	HADA03P3R3	36.02	36.28	36.07	36.23	36.39
HADA03P3R3	ICG Kunitz-type cysteine	KRT6	0.64	0.39	11	11	7	389	389	247	28.788	0	1.83	1.7E+09	50	HADA03P3R3	HADA03P3R3	36.02	36.28	36.07	36.23	36.39
HADA03P3R3	ICG Kunitz-type cysteine	KRT6	0.64	0.39	11	11	7	389	389	247	28.788	0	1.83	1.7E+09	50	HADA03P3R3	HADA03P3R3	36.02	36.28	36.07	36.23	36.39
HADA03P3R3	ICG Kunitz-type cysteine	KRT6	0.64	0.39	11	11	7	389	389	247	28.788	0	1.83	1.7E+09	50	HADA03P3R3	HADA03P3R3	36.02	36.28	36.07	36.23	36.39
HADA03P3R3	ICG Kunitz-type cysteine	KRT6	0.64	0.39	11	11	7	389	389	247	28.788	0	1.83	1.7E+09	50	HADA03P3R3	HADA03P3R3	36.02	36.28	36.07	36.23	36.39
HADA03P3R3	ICG Kunitz-type cysteine	KRT6	0.64	0.39	11	11	7	389	389	247	28.788	0	1.83	1.7E+09	50	HADA03P3R3	HADA03P3R3	36.02	36.28	36.07	36.23	36.39
HADA03P3R3	ICG Kunitz-type cysteine	KRT6	0.64	0.39	11	11	7	389	389	247	28.788	0	1.83	1.7E+09	50	HADA03P3R3	HADA03P3R3	36.02	36.28	36.07	36.23	36.39
HADA03P3R3	ICG Kunitz-type cysteine	KRT6	0.64	0.39	11	11	7	389	389	247	28.788	0	1.83	1.7E+09	50	HADA03P3R3	HADA03P3R3	36.02	36.28	36.07	36.23	36.39
HADA03P3R3	ICG Kunitz-type cysteine	KRT6	0.64	0.39	11	11	7	389	389	247	28.788	0	1.83	1.7E+09	50	HADA03P3R3	HADA03P3R3	36.02	36.28	36.07	36.23	36.39
HADA03P3R3	ICG Kunitz-type cysteine	KRT6	0.64	0.39	11	11	7	389	389	247	28.788	0	1.83	1.7E+09	50	HADA03P3R3	HADA03P3R3	36.02	36.28	36.07	36.23	36.39
HADA03P3R3	ICG Kunitz-type cysteine	KRT6	0.64	0.39	11	11	7	389	389	247	28.788	0	1.83	1.7E+09	50	HADA03P3R3	HADA03P3R3	36.02	36.28	36.07	36.23	36.39
HADA03P3R3	ICG Kunitz-type cysteine	KRT6	0.64	0.39	11	11	7	389	389	247	28.788	0	1.83	1.7E+09	50	HADA03P3R3	HADA03P3R3	36.02	36.28	36.07	36.23	36.39
HADA03P3R3	ICG Kunitz-type cysteine	KRT6	0.64	0.39	11	11	7	389	389	247	28.788	0	1.83	1.7E+09	50	HADA03P3R3	HADA03P3R3	36.02	36.28	36.07	36.23	36.39
HADA03P3R3	ICG Kunitz-type cysteine	KRT6	0.64	0.39	11	11	7	389	389	247	28.788	0	1.83	1.7E+09	50	HADA03P3R3	HADA03P3R3	36.02	36.28	36.07	36.23	36.39
HADA03P3R3	ICG Kunitz-type cysteine	KRT6	0.64	0.39	11	11	7	389	389	247	28.788	0	1.83	1.7E+09	50	HADA03P3R3	HADA03P3R3	36.02	36.28	36.07	36.23	36.39
HADA03P3R3	ICG Kunitz-type cysteine	KRT6	0.64	0.39	11	11	7	389	389	247	28.788	0	1.83	1.7E+09	50	HADA03P3R3	HADA03P3R3	36.02	36.28	36.07	36.23	36.39
HADA03P3R3	ICG Kunitz-type cysteine	KRT6	0.64	0.39	11	11	7	389	389	247	28.788	0	1.83	1.7E+09	50	HADA03P3R3	HADA03P3R3	36.02	36.28	36.07	36.23	36.39
HADA03P3R3	ICG Kunitz-type cysteine	KRT6	0.64	0.39	11	11	7	389	389	247	28.788	0	1.83	1.7E+09	50	HADA03P3R3	HADA03P3R3	36.02	36.28	36.07	36.23	36.39
HADA03P3R3	ICG Kunitz-type cysteine	KRT6	0.64	0.39	11	11	7	389	389	247	28.788	0	1.83	1.7E+09	50	HADA03P3R3	HADA03P3R3	36.02	36.28	36.07	36.23	36.39
HADA03P3R3	ICG Kunitz-type cysteine	KRT6	0.64	0.39	11	11	7	389	389	247	28.788	0	1.83	1.7E+09	50	HADA03P3R3	HADA03P3R3	36.02	36.28	36.07	36.23	36.39
HADA03P3R3	ICG Kunitz-type cysteine	KRT6	0.64	0.39	11	11	7	389	389	247	28.788	0	1.83	1.7E+09	50	HADA03P3R3	HADA03P3R3	36.02	36.28	36.07	36.23	36.39
HADA03P3R3	ICG Kunitz-type cysteine	KRT6	0.64	0.39	11	11	7	389	389	247	28.788	0	1.83	1.7E+09	50	HADA03P3R3	HADA03P3R3	36.02	36.28	36.07	36.23	36.39
HADA03P3R3	ICG Kunitz-type cysteine	KRT6	0.64	0.39	11	11	7	389	389	247	28.788	0	1.83	1.7E+09	50	HADA03P3R3	HADA03P3R3	36.02	36.28	36.07	36.23	36.39
HADA03P3R3	ICG Kunitz-type cysteine	KRT6	0.64	0.39	11	11	7	389	389	247	28.788	0	1.83	1.7E+09	50	HADA03P3R3	HADA03P3R3	36.02	36.28	36.07	36.23	36.39
HADA03P3R3	ICG Kunitz-type cysteine	KRT6	0.64	0.39	11	11	7	389	389	247	28.788	0	1.83	1.7E+09	50	HADA03P3R3	HADA03P3R3	36.02	36.28	36.07	36.23	36.39
HADA03P3R3	ICG Kunitz-type cysteine	KRT6	0.64	0.39	11	11	7	389	389	247	28.788	0	1.83	1.7E+09	50	HADA03P3R3	HADA03P3R3	36.02	36.28	36.07	36.23	36.39
HADA03P3R3	ICG Kunitz-type cysteine	KRT6	0.64	0.39	11	11	7	389	389	247	28.788	0	1.83	1.7E+09	50	HADA03P3R3	HADA03P3R3	36.02	36.28	36.07	36.23	36.39
HADA03P3R3	ICG Kunitz-type cysteine	KRT6	0.64	0.39	11	11	7	389	389	247	28.788	0	1.83	1.7E+09	50	HADA03P3R3	HADA03P3R3	36.02	36.28	36.07	36.23	36.39
HADA03P3R3	ICG Kunitz-type cysteine	KRT6	0.64	0.39	11	11	7	389	389	247	28.788	0	1.83	1.7E+09	50	HADA03P3R3	HADA03P3R3	36.02	36.28	36.07	36.23	36.39
HADA03P3R3	ICG Kunitz-type cysteine	KRT6	0.64	0.39	11	11	7	389	389	247	28.788	0	1.83	1.7E+09	50	HADA03P3R3	HADA03P3R3	36.02	36.28	36.07	36.23	36.39
HADA03P3R3	ICG Kunitz-type cysteine	KRT6	0.64	0.39	11	11	7	389	389	247	28.788	0	1.83	1.7E+09	50	HADA03P3R3	HADA03P3R3	36.02	36.28	36.07	36.23	36.39
HADA03P3R3	ICG Kunitz-type cysteine	KRT6	0.64	0.39	11	11	7	389	389	247	28.788	0	1.83	1.7E+09	50	HADA03P3R3	HADA03P3R3	36.02	36.28	36.07	36.23	36.39
HADA03P3R3	ICG Kunitz-type cysteine	KRT6	0.64	0.39	11	11	7	389	389	247	28.788	0	1.83	1.7E+09	50	HADA03P3R3	HADA03P3R3	36.02	36.28	36.07	36.23	36.39
HADA03P3R3	ICG Kunitz-type cysteine	KRT6	0.64	0.39	11	11	7	389	389	247	28.788	0	1.83	1.7E+09	50	HADA03P3R3	HADA03P3R3	36.02	36.28	36.07	36.23	36.39
HADA03P3R3	ICG Kunitz-type cysteine	KRT6	0.64	0.39	11	11	7	389	389	247	28.788	0	1.83	1.7E+09	50	HADA03P3R3	HADA03P3R3	36.02	36.28	36.07	36.23	36.39
HADA03P3R3	ICG Kunitz-type cysteine	KRT6	0.64	0.39	11	11	7	389	389	247	28.788	0	1.83	1.7E+09	50	HADA03P3R3	HADA03P3R3	36.02	36.28	36.07	36.23	36.39
HADA03P3R3	ICG Kunitz-type cysteine	KRT6	0.64	0.39	11	11	7	389	389	247	28.788	0	1.83	1.7E+09	50	HADA03P3R3	HADA03P3R3	36.02	36.28	36.07	36.23	36.39
HADA03P3R3	ICG Kunitz-type cysteine	KRT6	0.64	0.39	11	11	7	389	389	247	28.788	0	1.83	1.7E+09	50	HADA03P3R3	HADA03P3R3	36.02	36.28	36.07	36.23	36.39
HADA03P3R3	ICG Kunitz-type cysteine	KRT6																				

h00058627.1, Intron base 1	IT001	0.34	0.19	3	3	2	58	58	58	87.46	0.638	2.23E-08	2522	2538	2541	2549	2549	2549	
h00058628.1, Exon 3	MATK3	0.33	0.14	14	14	14	267	267	267	88.56	0.166	2.83E-09	2530	2546	2551	2562	2564	2569	
h00058630.1, Cytosine light chain 1 C1TA		0.40	0.14	3	3	3	21.7	21.7	21.7	17.687	0.1636	1.69E-08	2542	2550	2551	2562	2563	2565	
h00058631.1, U small nuclear R, HNRPNP20		0.20	0.14	4	4	4	3.1	3.1	3.1	24.5	0.126	2.88E-08	2563	2553	2553	2560	2560	2570	
h00058632.1, Poliovirus, active, P1		0.45	0.16	4	4	4	32.1	32.1	32.1	85.72	0.1617	4.81E-08	2565	2568	2568	2576	2580	2581	
h00058633.1, Poliovirus, active, P2		0.45	0.13	1	1	1	3	3	3	37.504	0.3503	3.00E-09	2565	2568	2568	2576	2580	2581	
h00058634.1, 28S ribosomal protein, MRPS22		0.18	0.12	2	2	2	17	17	17	16.973	0.4503	1.27E-08	2581	2454	2457	2463	2461	2525	
h00058635.1, Intron subunit base, KPNR1		0.23	0.12	15	15	15	23.3	23.3	23.3	97.189	0.1138	2.86E-09	2582	2586	2585	2597	2615	2615	
h00058636.1, 26S proteasome, PSMC3		0.20	0.12	3	3	3	11.6	11.6	11.6	44.323	0.1102	3.22E-08	2583	2586	2587	2594	2590	2629	
h00058637.1, Cytosine complex, NCAPO22		0.22	0.12	3	3	3	34	34	34	197.48	0.4689	1.71E-08	2587	2513	2483	2547	2548	2585	
h00058638.1, A TP gamma subunit, ATP5A		0.17	0.12	3	3	3	44.4	44.4	44.4	12.507	0.1236	3.55E-08	2587	2597	2609	2672	2600	2608	
h00058639.1, Exon 1, ERF1	ERL1N, ERF1	0.14	0.11	3	3	3	10.9	10.9	10.9	38.171	0.2071	4.44E-08	2589	2609	2609	2678	2638	2643	
h00058640.1, Tompkin protein 1, C1CTA		0.22	0.11	6	6	6	16.6	16.6	16.6	56.024	0.1219	1.81E-09	2589	2622	2627	2596	2596	2621	
h00058641.1, 45S ribosomal protein, P1, P1T1		0.28	0.10	3	3	3	23.1	23.1	23.1	19.906	0.1073	4.04E-08	2589	2632	2638	2529	2529	2588	
h00058642.1, Tompkin protein 1, C1CTA		0.24	0.10	8	8	8	18.7	18.7	18.7	54.719	0.1286	1.05E-09	2589	2636	2636	2580	2580	2583	
h00058643.1, Histone subunit, H1, H1P0A0A		0.18	0.10	27	27	27	38.4	38.4	38.4	63.263	0.3233	1.79E-10	2592	2638	2638	2571	2571	2612	
h00058644.1, Mitochondrial protein, PDMC1		0.12	0.09	3	3	3	11.8	11.8	11.8	21.671	0.2081	7.5E-08	2594	2638	2638	2571	2571	2612	
h00058645.1, Elongation factor 2, E2F2		0.19	0.09	19	19	19	24.5	24.5	24.5	93.337	0.126	3.7E-09	2594	2638	2638	2571	2571	2612	
h00058646.1, Histone subunit, H1, H1P0A0A		0.18	0.09	15	15	15	40.9	40.9	40.9	46.562	0.1027	3.06E-09	2594	2638	2638	2571	2571	2612	
h00058647.1, A TP gamma subunit, ATP5C1		0.19	0.09	6	6	6	19.9	19.9	19.9	32.881	0.2732	1.96E-09	2594	2638	2638	2571	2571	2612	
h00058648.1, Tofin base 4, TUBB4		0.22	0.09	17	17	17	5.27	5.27	5.27	48.957	0.2518	6.52E-09	2594	2638	2638	2571	2571	2612	
h00058649.1, Intron subunit, IIR		0.27	0.09	4	4	4	15.3	15.3	15.3	39.91	0.17	2.08E-08	2594	2638	2638	2571	2571	2612	
h00058650.1, Nucleolar subunit, NOL1		0.18	0.08	10	10	10	14.4	14.4	14.4	15.450	0.3528	2.59E-09	2594	2638	2638	2571	2571	2612	
h00058651.1, Cytosine-associated, N1, C1D01		0.09	0.08	3	3	3	37.6	37.6	37.6	9.541	0.1207	3.88E-08	2594	2638	2638	2571	2571	2612	
h00058652.1, Histone subunit, H1, H1P0A0A		0.21	0.08	4	4	4	6.8	6.8	6.8	68.408	0.1284	2.87E-08	2594	2638	2638	2571	2571	2612	
h00058653.1, Histone subunit, H1, H1P0A0A		0.19	0.08	3	3	3	16.8	16.8	16.8	38.788	0.248	4.57E-08	2594	2638	2638	2571	2571	2612	
h00058654.1, Histone subunit, H1, H1P0A0A		0.18	0.07	5	5	5	13.4	13.4	13.4	40.033	0.8236	3.03E-08	2594	2638	2638	2571	2571	2612	
h00058655.1, Histone subunit, H1, H1P0A0A		0.17	0.07	3	3	3	10	10	10	48.102	0.6507	2.47E-08	2594	2638	2638	2571	2571	2612	
h00058656.1, Histone subunit, H1, H1P0A0A		0.15	0.07	11	11	11	61.2	61.2	61.2	11.367	0.107	9.51E-10	2594	2638	2638	2571	2571	2612	
h00058657.1, Histone subunit, H1, H1P0A0A		0.03	0.07	8	8	8	31.6	31.6	31.6	21.6	35.5	0.5535	2.26E-09	2594	2638	2638	2571	2571	2612
h00058658.1, Histone subunit, H1, H1P0A0A		0.07	0.06	4	4	4	6.8	6.8	6.8	11.53	0.6803	3.81E-08	2594	2638	2638	2571	2571	2612	
h00058659.1, Histone subunit, H1, H1P0A0A		0.06	0.06	9	9	9	43.1	43.1	43.1	24.488	0.2171	1.84E-09	2594	2638	2638	2571	2571	2612	
h00058660.1, Histone subunit, H1, H1P0A0A		0.02	0.06	3	3	3	17	17	17	16.714	0.4313	2.62E-08	2594	2638	2638	2571	2571	2612	
h00058661.1, Histone subunit, H1, H1P0A0A		0.08	0.06	9	9	9	16.9	16.9	16.9	63.587	0.2814	9.25E-09	2594	2638	2638	2571	2571	2612	
h00058662.1, Histone subunit, H1, H1P0A0A		0.10	0.06	3	3	3	27.2	27.2	27.2	27.2	0.380	7.88E-08	2594	2638	2638	2571	2571	2612	
h00058663.1, Histone subunit, H1, H1P0A0A		0.07	0.06	2	2	2	31.9	31.9	31.9	11.263	0.283	9.25E-09	2594	2638	2638	2571	2571	2612	
h00058664.1, Histone subunit, H1, H1P0A0A		0.16	0.05	3	3	3	16	16	16	18.72	0.2039	8.17E-08	2594	2638	2638	2571	2571	2612	
h00058665.1, Histone subunit, H1, H1P0A0A		0.01	0.05	6	6	6	5.8	5.8	5.8	12.38	0.1387	3.17E-08	2594	2638	2638	2571	2571	2612	
h00058666.1, Histone subunit, H1, H1P0A0A		0.08	0.04	5	5	5	5.4	5.4	5.4	170.59	0.1385	4.21E-09	2594	2638	2638	2571	2571	2612	
h00058667.1, Histone subunit, H1, H1P0A0A		0.10	0.04	19	19	19	51.9	51.9	51.9	27	0.485	1.03E-10	2594	2638	2638	2571	2571	2612	
h00058668.1, Histone subunit, H1, H1P0A0A		0.07	0.04	6	6	6	1.4	1.4	1.4	18.716	0.1418	1.81E-08	2594	2638	2638	2571	2571	2612	
h00058669.1, Histone subunit, H1, H1P0A0A		0.04	0.03	2	2	2	9.9	9.9	9.9	25.223	0.2035	4.25E-08	2594	2638	2638	2571	2571	2612	
h00058670.1, Histone subunit, H1, H1P0A0A		0.05	0.03	24	24	24	48.3	48.3	48.3	61.054	0.3233	1.26E-10	2594	2638	2638	2571	2571	2612	
h00058671.1, Histone subunit, H1, H1P0A0A		0.02	0.03	4	4	4	2.1	2.1	2.1	22.275	0.469	1.11E-08	2594	2638	2638	2571	2571	2612	
h00058672.1, Histone subunit, H1, H1P0A0A		0.03	0.03	10	10	10	14.2	14.2	14.2	14.522	0.1839	8.81E-09	2594	2638	2638	2571	2571	2612	
h00058673.1, Histone subunit, H1, H1P0A0A		0.03	0.02	22	22	22	40.8	40.8	40.8	37.9	0.603	4.81E-08	2594	2638	2638	2571	2571	2612	
h00058674.1, Histone subunit, H1, H1P0A0A		0.04	0.02	6	6	6	7.2	7.2	7.2	98.719	0.1887	6.89E-08	2594	2638	2638	2571	2571	2612	
h00058675.1, Histone subunit, H1, H1P0A0A		0.03	0.02	5	5	5	28.1	28.1	28.1	23.078	0.4836	5.41E-09	2594	2638	2638	2571	2571	2612	
h00058676.1, Histone subunit, H1, H1P0A0A		0.04	0.02	6	6	6	17.2	17.2	17.2	48.133	0.2633	8.21E-08	2594	2638	2638	2571	2571	2612	
h00058677.1, Histone subunit, H1, H1P0A0A		0.03	0.02	2	2	2	12.8	12.8	12.8	22.042	0.4386	2.11E-08	2594	2638	2638	2571	2571	2612	
h00058678.1, Histone subunit, H1, H1P0A0A		0.03	0.02	2	2	2	7.1	7.1	7.1	32.408	0.4309	2.47E-08	2594	2638	2638	2571	2571	2612	
h00058679.1, Histone subunit, H1, H1P0A0A		0.01	0.01	3	3	3	7.6	7.6	7.6	47.776	0.7289	2.11E-08	2594	2638	2638	2571	2571	2612	
h00058680.1, Histone subunit, H1, H1P0A0A		0.00	0.00	15	15	15	45.9	45.9	45.9	47.168	0.2039	1.75E-09	2594	2638	2638	2571	2571	2612	
h00058681.1, Histone subunit, H1, H1P0A0A		0.01	0.00	6	6	6	29	29	29	29	0.1916	1.33E-09	2594	2638	2638	2571	2571	2612	
h00058682.1, Histone subunit, H1, H1P0A0A		0.00	0.00	5	5	5	7.5	7.5	7.5	93.307	0.112	3.83E-08	2594	2638	2638	2571	2571	2612	
h00058683.1, Histone subunit, H1, H1P0A0A		0.00	0.00	12	12	12	1	1	1	42.051	0.4577	5.35E-09	2594	2638	2638	2571	2571	2612	
h00058684.1, Histone subunit, H1, H1P0A0A		0.02	0.00	4	4	4	18.7	18.7	18.7	31.628	0.2225	5.83E-08	2594	2638	2638	2571	2571	2612	
h00058685.1, Histone subunit, H1, H1P0A0A		0.03	0.00	3	3	3	2	2	2	48.79	0.114	2.86E-08	2594	2638	2638	2571	2571	2612	
h00058686.1, Histone subunit, H1, H1P0A0A		0.03	0.00	2	2	2	17.9	17.9	17.9	16.689	0.3212	5.53E-08	2594	2638	2638	2571	2571	2612	
h00058687.1, Histone subunit, H1, H1P0A0A		0.01	0.00	2	2	2	15.7	15.7	15.7	17.235	0.3643	1.56E-08	2594	2638	2638	2571	2571	2612	
h00058688.1, Histone subunit, H1, H1P0A0A		0.03	0.00	13	13	13	31.1	31.1	31.1	68.589	0.9636	2.21E-09	2594	2638	2638	2571	2571	2612	
h00058689.1, Histone subunit, H1, H1P0A0A		0.04	0.00	4	4	4	8.1	8.1	8.1	93.522	0.4122	3.26E-08	2594	2638	2638	2571	2571	2612	
h00058690.1, Histone subunit, H1, H1P0A0A		0.03	0.00	2	2	2	12.8	12.8	12.8	22.042	0.4386	2.11E-08	2594	2638	2638	2571	2571	2612	
h00058691.1, Histone subunit, H1, H1P0A0A		0.02	0.00	2	2	2	30.4	30.4	30.4	7.931	0.3786	2.44E-08	2594	2638	2638	2571	2571	2612	
h00058692.1, Histone subunit, H1, H1P0A0A		0.03	0.00	5	5	5</													

REP2209(MCM) DNA replication fork MCM3	0.03	-0.15	10	10	17.1	17.1	17.1	60.96	0.4834	1.28E+09	47	P2209(P2209)	28.12	28.07	28.22	27.97	27.84	28.12	
REP3023(L3) H3 ribosomal prot. RPL3	0.09	-0.15	7	7	20.8	20.8	46.108	0.2908	8.74E+08	17	P3023(P3023)	28.18	28.06	28.01	25.70	28.60	28.09	28.09	
REP4140(G2A1) Ras GTPase-activat. G2A1	0.22	-0.15	5	5	4.2	4.2	36.192	0.1536	1.80E+08	9	P4140(P4140)	25.28	24.94	25.20	25.40	24.90	24.60	24.60	
REP5212(TNA) Caprin alpha(Ca) CNA motif TNA3	0.51	-0.15	2	2	2.9	2.9	10.027	0.00452	2.20E+08E+08	4	P5212(P5212)	30.36	29.82	30.32	30.30	29.87	30.08	30.08	
REP6107(R32) Histone H3A type-2, H3B TUBA2(TH3AA)	0.15	-0.16	7	7	1	63.6	63.6	22.5	1.8906	1.07E+08	63	G6107(G6107)	32.30	32.34	32.08	31.94	31.36	32.34	
REP5152B(AP3) B cell nucleosome-assembly RCPA31	0.11	-0.16	4	4	4	16.7	16.7	16.7	0.174	2.86E+08	17	P5152B(P5152B)	25.67	25.59	25.78	25.84	25.34	25.70	
REP5152B(SD3) Drosophila melanogaster ADAR	0.48	-0.16	4	4	4	5.3	5.3	10.64	0.8326	1.77E+08	5	P5152B(SD3)	25.47	25.05	25.17	25.15	24.94	25.13	
REP5152B(TC) Tetracycline-activated, HADA	0.49	-0.16	9	9	9	13.6	13.6	66.371	0.1439	1.02E+08	39	H5152B(TC)	27.74	27.64	27.66	27.67	27.61	27.69	
REP6700(R10X) Nucleosome-assembly YK01	0.38	-0.17	7	7	5	41	31.2	35.926	0.9446	6.84E+08	37	P6700(P6700)	27.81	27.65	27.21	27.34	27.46	27.38	
REP5084(EF3B) Eukaryotic translation EFB3	0.22	-0.17	2	2	2	2.8	2.8	82.48	0.9189	1.82E+08	16	P5084(EF3B)	25.31	25.52	25.30	25.60	24.87	24.98	
REP008152(E2P) Uncharacterized protein C0K0P7	0.31	-0.18	3	3	3	6.2	6.2	62.5180	0.1532	1.28E+08	9	C008152(E2P)	24.85	24.66	24.71	24.82	24.12	24.77	
REP12120P(L2) Nucleon polypeptide P120	0.46	-0.18	4	4	4	40.4	40.4	40.4	0.4627	2.23E+08	27	P12120P(L2)	27.84	27.44	26.95	27.13	27.00	27.05	
REP0419(R3) Phosphorylation state P19A	0.34	-0.19	8	8	8	35.8	35.8	18.012	0.7549	3.95E+08	40	P0419(R3)	30.29	30.20	30.50	30.55	29.84	30.10	
REP2208(P0A2) Haemoglobin subunit HNRNP0A21	0.24	-0.19	16	16	15	42.2	42.2	42.2	0.1471	4.34E+08	110	P2208(P2208)	29.99	29.65	29.86	30.16	29.67	29.75	
REP04040(D5) 5' Deoxythymidylate D004T	0.30	-0.20	5	5	5	16.2	16.2	48.789	0.9434	1.01E+08	17	P04040(D5)	27.82	27.47	28.31	27.89	27.44	27.88	
REP0191(R10A2) Haemoglobin subunit HNRNP0A2	0.39	-0.20	7	7	7	31.2	31.2	31.2	0.1054	1.22E+08	40	P0191(R10A2)	28.65	27.91	27.78	27.96	27.71	27.85	
REP0030B(L3) Ribosomal protein RAB19	0.23	-0.20	4	3	3	30.5	15	22.491	0.1333	4.42E+08	4	P030B(L3)	28.54	28.37	27.17	28.47	28.38	28.38	
REP50040(APO) Exportin-2 CSE1	0.44	-0.21	14	14	14	16.8	16.8	10.88	0.1904	1.25E+08	62	P50040(APO)	31.38	31.34	31.39	31.49	31.02	30.83	
REP0428(P1A) H3 histone chain H1.1 H1H7P22H3V03R16M5	0.31	-0.21	4	4	4	36.7	36.7	16.159	0.1832	7.89E+08	15	P0428(P1A)	27.53	27.15	27.34	26.81	27.56	27.14	
REP04040(D5) H3 histone chain H1.1 H1H7P22H3V03R16M5	0.16	-0.21	9	9	2	44	4	6.1804	0.1642	5.53E+08	79	P04040(D5)	28.66	33.16	33.16	33.23	33.88	32.94	
REP04040(D5) H3 histone chain H1.1 H1H7P22H3V03R16M5	0.24	-0.21	10	10	8.2	8.2	8.2	18.601	0.3489	6.02E+08	22	C04040(D5)	28.63	27.02	27.47	27.48	26.56	26.98	
REP04040(D5) H3 histone chain H1.1 H1H7P22H3V03R16M5	0.70	-0.21	6	3	3	62.8	30.8	30.8	0.9402	5.58E+08	15	C04040(D5)	28.61	26.00	26.88	26.13	26.52	26.56	
REP04040(D5) H3 histone chain H1.1 H1H7P22H3V03R16M5	0.34	-0.22	7	7	7	34.5	34.5	28.621	0.1123	1.65E+08	42	E04040(D5)	28.58	28.44	28.66	27.82	28.32	28.32	
REP04040(D5) H3 histone chain H1.1 H1H7P22H3V03R16M5	0.11	-0.22	7	7	7	12.8	12.8	62.238	0.148	5.43E+08	23	P04040(D5)	28.60	28.62	27.94	28.64	26.47	26.77	
REP04040(D5) H3 histone chain H1.1 H1H7P22H3V03R16M5	0.46	-0.22	2	2	2	3.7	3.7	17.085	0.2373	1.47E+08	6	E04040(D5)	25.52	25.16	24.80	24.63	25.04	24.98	
REP04040(D5) H3 histone chain H1.1 H1H7P22H3V03R16M5	0.17	-0.22	5	5	5	16	16	69.491	0.4536	1.25E+08	26	C04040(D5)	25.56	27.71	27.45	28.04	25.09	25.71	
REP04040(D5) H3 histone chain H1.1 H1H7P22H3V03R16M5	0.71	-0.24	5	4	4	14.6	12.4	12.4	40.34	0.1029	2.56E+08	18	P04040(D5)	25.87	25.73	25.29	25.75	25.40	25.82
REP04040(D5) H3 histone chain H1.1 H1H7P22H3V03R16M5	0.03	-0.24	2	2	2	17.8	17.8	11.167	0.153	1.60E+08	22	P04040(D5)	25.97	25.71	25.88	25.13	25.43	25.38	
REP04040(D5) H3 histone chain H1.1 H1H7P22H3V03R16M5	0.23	-0.24	2	2	2	1.5	1.5	1.5	0.125	1.45E+08	37	E04040(D5)	26.03	25.83	25.83	25.83	25.83	25.83	
REP04040(D5) H3 histone chain H1.1 H1H7P22H3V03R16M5	0.30	-0.25	6	6	6	16	16	16	46.971	0.2457	9.07E+08	24	G04040(D5)	27.71	27.51	27.56	26.88	27.17	26.90
REP04040(D5) H3 histone chain H1.1 H1H7P22H3V03R16M5	0.03	-0.25	11	10	10	23.8	21.9	21.9	68.047	0.7576	1.29E+08	47	P04040(D5)	26.87	27.06	27.37	27.87	27.87	27.87
REP04040(D5) H3 histone chain H1.1 H1H7P22H3V03R16M5	0.45	-0.25	11	6	6	18	10.8	10.8	80.253	0.2834	1.42E+08	18	P04040(D5)	26.88	26.83	26.83	26.83	27.15	27.12
REP04040(D5) H3 histone chain H1.1 H1H7P22H3V03R16M5	0.13	-0.25	11	11	11	5.3	5.3	5.3	13.1	0.441	1.50E+08	3	C04040(D5)	26.87	26.87	26.87	26.87	26.87	26.87
REP04040(D5) H3 histone chain H1.1 H1H7P22H3V03R16M5	0.05	-0.26	6	6	3	52.7	52.7	20.9	9.762	0.367	2.29E+08	37	C04040(D5)	28.12	28.91	28.90	28.91	28.60	28.65
REP04040(D5) H3 histone chain H1.1 H1H7P22H3V03R16M5	0.31	-0.26	1	1	1	1.8	1.8	1.8	144.47	0.2441	1.46E+08	14	H04040(D5)	31.74	31.37	31.35	31.16	31.36	32.02
REP04040(D5) H3 histone chain H1.1 H1H7P22H3V03R16M5	0.04	-0.27	11	11	11	61.5	61.5	61.5	22.782	0.1866	8.54E+08	10	P04040(D5)	31.05	30.99	31.05	30.99	31.04	30.98
REP04040(D5) H3 histone chain H1.1 H1H7P22H3V03R16M5	0.32	-0.27	12	11	11	47.2	44.3	44.3	33.159	0.146	2.29E+08	49	P04040(D5)	26.90	26.90	26.90	26.90	26.90	26.90
REP04040(D5) H3 histone chain H1.1 H1H7P22H3V03R16M5	0.11	-0.27	5	5	5	19	19	19	64.922	0.2437	1.45E+08	12	E04040(D5)	26.93	26.93	26.93	26.93	26.93	26.93
REP04040(D5) H3 histone chain H1.1 H1H7P22H3V03R16M5	0.44	-0.27	7	4	4	25.6	17.7	17.7	47.497	0.2544	1.55E+08	24	C04040(D5)	26.98	26.97	26.98	26.97	26.97	26.97
REP04040(D5) H3 histone chain H1.1 H1H7P22H3V03R16M5	0.44	-0.28	2	2	2	21.7	21.7	18.891	0.1901	5.42E+08	10	G04040(D5)	27.55	26.99	26.99	26.99	26.99	26.99	
REP04040(D5) H3 histone chain H1.1 H1H7P22H3V03R16M5	0.30	-0.30	24	24	24	57.8	57.8	57.8	34.004	0.3233	4.30E+08	28	P04040(D5)	33.32	33.28	33.28	33.28	33.28	33.28
REP04040(D5) H3 histone chain H1.1 H1H7P22H3V03R16M5	0.35	-0.30	5	5	5	18.9	18.9	18.9	35.48	0.3025	1.50E+08	48	C04040(D5)	26.95	26.15	26.95	26.95	26.95	26.95
REP04040(D5) H3 histone chain H1.1 H1H7P22H3V03R16M5	0.90	-0.30	5	5	5	5.3	5.3	5.3	12.75	0.1233	2.80E+08	15	H04040(D5)	25.99	25.97	25.99	25.99	25.99	25.99
REP04040(D5) H3 histone chain H1.1 H1H7P22H3V03R16M5	0.88	-0.30	6	5	5	16.6	14.2	14.2	47.087	0.1910	2.13E+08	43	E04040(D5)	26.99	26.75	26.98	26.81	26.93	26.93
REP04040(D5) H3 histone chain H1.1 H1H7P22H3V03R16M5	0.22	-0.31	4	4	4	6.6	6.6	6.6	11.005	0.5638	1.24E+08	31	P04040(D5)	26.92	26.92	26.92	26.92	26.92	26.92
REP04040(D5) H3 histone chain H1.1 H1H7P22H3V03R16M5	0.11	-0.31	5	5	5	19	19	19	64.922	0.2437	1.45E+08	12	E04040(D5)	26.93	26.93	26.93	26.93	26.93	26.93
REP04040(D5) H3 histone chain H1.1 H1H7P22H3V03R16M5	0.53	-0.31	10	10	5	36.2	36.2	32.711	0.1472	2.80E+08	40	C04040(D5)	29.21	29.21	29.21	29.21	29.21	29.21	
REP04040(D5) H3 histone chain H1.1 H1H7P22H3V03R16M5	0.30	-0.32	6	3	3	63	22	22	14.558	0.7405	1.45E+08	13	C04040(D5)	26.42	26.11	27.01	26.80	26.03	26.28
REP04040(D5) H3 histone chain H1.1 H1H7P22H3V03R16M5	0.19	-0.32	6	6	6	24.7	24.7	24.7	32.728	0.5336	1.70E+08	12	C04040(D5)	27.40	26.53	27.19	26.01	26.02	26.48
REP04040(D5) H3 histone chain H1.1 H1H7P22H3V03R16M5	0.91	-0.32	16	16	16	61.2	61.2	61.2	28.415	0.3233	4.40E+08	15	C04040(D5)	26.25	26.15	26.25	26.15	26.25	26.15
REP04040(D5) H3 histone chain H1.1 H1H7P22H3V03R16M5	0.43	-0.33	4	4	4	5.2	5.2	5.2	10.31	0.1219	2.75E+08	9	C04040(D5)	26.12	25.91	25.94	25.90	24.96	25.75
REP04040(D5) H3 histone chain H1.1 H1H7P22H3V03R16M5	1.04	-0.33	8	8	8	21.7	21.7	21.7	47.837	0.4275	1.55E+08	35	G04040(D5)	26.01	26.00	26.00	26.00	26.00	26.00
REP04040(D5) H3 histone chain H1.1 H1H7P22H3V03R16M5	0.87	-0.33	5	5	5	21.9	21.9	21.9	31.8	0.2045	1.55E+08	12	C04040(D5)	27.08	26.97	26.97	26.97	26.97	26.97
REP04040(D5) H3 histone chain H1.1 H1H7P22H3V03R16M5	1.23	-0.33	10	10	10	25.9	25.9	25.9	44.955	0.9549	1.85E+08	21	C04040(D5)	27.61	27.68	27.53	27.50	27.20	27.55
REP04040(D5) H3 histone chain H1.1 H1H7P22H3V03R16M5	0.15	-0.34	2	2	2	16.8	16.8	16.8	17.838	0.345	1.29E+08	11	P04040(D5)	26.95	26.95	26.95	26.95	26.95	26.95
REP04040(D5) H3 histone chain H1.1 H1H7P22H3V03R16M5	0.32	-0.34	4	4	4	6.7	6.7	6.7	84.97	0.1485	1.61E+08	15	P04040(D5)	26.68	26.94	26.98	26.68	26.41	26.80
REP04040(D5) H3 histone chain H1.1 H1H7P22H3V03R16M5	0.23	-0.35	2	2	2	23	23	23	11.477	0.2144	4.01E+08	12	L04040(D5)	26.33	26.14	26.47	26.47	27.00	25.59
REP04040(D5) H3 histone chain H1.1 H1H7P22H3V03R16M5	0.75	-0.37	6	6	6	1.65	1.65	1.65	42.033	0.2846	1.50E+08	25	C04040(D5)	27.04	26.71	26.78	26.51		

hZNF384ZC1 Zinc finger CCHC1 ZC3H4C1	+	1.59	-0.69	4	4	4	16.7	16.7	16.7	32.962	0	15.37	3.86E-08	19	GM01787	GM01787	26.90	26.90	26.24	25.99	25.62	25.90
hZNF146KOT1 Kaposin domain PRKORP	+	1.85	-0.71	6	6	6	23.9	23.9	23.9	34.412	0	32.04	2.38E-08	45	Q9H4B4	Q9H4B4	29.59	29.40	29.40	29.54	29.67	29.07
hZNF036JG10 Ribosomal protein RPL19	+	0.32	-0.72	4	4	4	22.6	22.6	22.6	23.134	0	29.82	4.88E-08	19	JG0109	JG0109	26.76	26.35	26.33	24.18	27.33	25.77
hZNF027CSP1 Cysteine and glycine CCRP2	+	2.04	-0.73	5	5	5	35.6	35.6	35.6	20.994	0	33.98	2.78E-07	49	CH2777	CH2777	29.70	29.29	29.32	29.60	29.65	28.87
hZNF106H121 Thiodian TSN	+	2.17	-0.74	5	5	5	42.9	42.9	42.9	11.727	0	28.86	3.03E-08	47	P10580P	P10580P	29.46	29.73	29.60	29.64	29.65	29.98
hZNF036R151A 60S ribosomal protein RPL15A	+	0.41	-0.75	3	3	3	13.4	13.4	13.4	24.831	0	5.087	2.17E-08	6	PC6206	PC6206	25.46	25.54	25.79	23.50	26.18	26.86
hZNF403Z5R15 Sonchomycin RSRP3	+	1.37	-0.77	4	4	4	3.06	3.06	3.06	14.203	0	21.2	1.59E-08	31	PM4032	PM4032	29.08	28.57	28.21	27.72	27.87	27.97
hZNF0454SER1 Sigan II BSRPNP	+	0.36	-0.78	3	3	3	11.7	11.7	11.7	46.41	0	16.11	1.20E-08	11	PS046E	PS046E	25.88	25.50	25.12	25.41	25.67	22.88
hZNF406Z0A22 Cysteine histidine DAZN2EN2EN2EN2EN	+	0.54	-0.79	2	2	2	7.3	7.3	7.3	46.46	0	2.987	2.32E-08	10	PS046E	PS046E	25.51	25.86	25.56	25.81	25.60	26.24
hZNF011SER1P 40S ribosomal protein RPS1	+	0.57	-0.80	9	9	9	63.3	63.3	63.3	17.407	0	21.97	1.34E-08	40	EMPPU1	EMPPU1	26.35	26.15	26.14	26.40	26.54	27.28
hZNF458UK1A Sonchomycin RSR46	+	1.56	-0.80	5	5	5	20.8	20.8	20.8	15.263	0	6.505	5.58E-08	19	AGA580	AGA580	27.44	27.17	26.96	26.76	26.21	26.19
hZNF273E1E1 E1uayalotransit R401	+	0.64	-0.82	2	2	2	1.7	1.7	1.7	19.604	0	6.418	8.94E-02	4	E1E1E1	E1E1E1	24.24	24.39	24.42	24.12	23.38	24.09
hZNF478R151Z 40S ribosomal protein RPS9	+	0.61	-0.85	10	10	10	43.8	43.8	43.8	22.591	0	16.33	1.2E-08	30	PA6781B	PA6781B	26.28	27.00	26.11	26.42	26.43	26.06
hZNF01010A1 Peptide S100A1P S100A1	+	0.56	-0.83	3	3	3	26.9	26.9	26.9	10.834	0	9.983	8.98E-08	20	P05509	P05509	27.61	27.74	28.86	26.40	27.56	26.95
hZNF460Z1A1 Peptide glutamine gl T003	+	1.07	-0.85	6	6	6	8.6	8.6	8.6	78.556	0	11.45	4.94E-08	15	ADA4AC	ADA4AC	26.36	26.96	27.47	25.77	26.42	26.08
hZNF4227R151 40S ribosomal protein RPS13	+	1.04	-0.85	6	6	6	35.8	35.8	35.8	17.222	0	25.31	1.2E-08	38	PE227J	PE227J	26.47	26.22	27.96	26.92	26.06	27.12
hZNF357R151Z 60S ribosomal protein RPL13	+	0.28	-0.85	7	7	7	28.9	28.9	28.9	24.261	0	48.13	8.96E-08	35	P38373	P38373	27.81	26.80	27.34	24.17	25.51	26.53
hZNF040ZCAT1 Catalase	+	0.93	-0.86	6	6	6	16	16	16	99.758	0	42.37	4.33E-08	18	PO4402	PO4402	26.82	27.91	27.13	26.05	26.99	26.24
hZNF127LZUK1 60S ribosomal protein RPL38	+	1.03	-0.87	3	3	3	38.1	38.1	38.1	7.849	0	3.66	1.12E-08	23	LK7L3J	LK7L3J	28.57	28.22	27.91	26.71	27.47	27.60
hZNF350ZTTP1 Thioalanyl temp G1225A1	+	0.66	-0.88	2	2	2	7.7	7.7	7.7	34.012	0	11.6	1.28E-08	6	P53077	P53077	25.43	24.91	23.72	23.53	24.14	24.22
hZNF425Z2H11 Histidine ammonia HAL	+	0.84	-0.89	2	2	2	3.4	3.4	3.4	64.887	0	2.738	1.03E-08	8	P42852	P42852	24.42	24.57	25.50	23.26	24.48	24.08
hZNF017C1S10 Peptide S100A14 S100A14	+	0.81	-0.91	2	2	2	25	25	25	21.662	0	12.99	1.08E-08	9	GHY7C5	GHY7C5	24.83	24.64	24.66	24.27	24.46	22.89
hZNF451R1P1P1 Peptide PEP1	+	1.24	-0.92	4	4	4	12	12	12	30.391	0	6.4	2.55E-08	13	GH0118	GH0118	26.28	25.91	26.20	25.22	24.63	26.05
hZNF008Z0A22 Acids bacitracin ANP38	+	0.68	-0.93	5	4	4	28.7	22.1	22.76	10.01	6.76E-08	16	GH008A2	GH008A2	27.95	27.96	28.13	26.74	26.20	26.25		
hZNF131R151 60S ribosomal protein RPL15	+	0.32	-0.93	6	6	6	32.8	32.8	32.8	24.146	0	30.22	4.7E-08	36	PE131A	PE131A	26.80	26.17	26.22	23.99	27.48	25.85
hZNF104R1C401 Catapsoin D Catap C18D	+	1.08	-0.93	4	4	4	12.2	12.2	12.2	35.765	0	21.82	3.93E-08	13	HTC48U	HTC48U	26.18	26.85	27.08	25.88	26.33	25.29
hZNF016R0ZS1Z 26S proteasome PMS2	+	0.56	-0.95	4	4	4	27.7	27.7	27.7	21.679	0	54.09	1.2E-08	19	HTC48U	HTC48U	26.11	26.19	26.15	25.90	26.52	27.17
hZNF356R1P1Z 26S proteasome PMS2	+	0.39	-0.96	3	3	3	7.6	7.6	7.6	46.633	0	4.284	2.63E-08	5	P3588P	P3588P	26.11	26.79	25.99	26.16	25.84	22.82
hZNF1706H10A1 High mobility glob HBSA1	+	1.32	-0.96	2	2	2	22.4	22.4	19	11.676	0	16.07	1.96E-08	8	P1706P	P1706P	26.28	25.54	25.17	24.81	24.52	24.77
hZNF107H10A1 40S ribosomal protein RPS2	+	0.69	-0.99	4	4	4	22.6	22.6	22.6	21.154	0	29.05	1.13E-08	23	HOY10E	HOY10E	26.21	26.15	27.82	26.10	26.29	26.81
hZNF026R1P1S1 Sigan B12 BSRPNB	+	1.85	-1.03	6	6	6	17.8	17.8	17.8	46.278	0	35.11	1.78E-08	39	GM01787	GM01787	27.87	28.33	27.99	26.63	27.26	27.21
hZNF017ZUK1Z1 Cysteine CDSNA	+	0.71	-1.04	2	2	2	13.9	13.9	13.9	17.918	0	4.498	1.04E-02	3	JKP48Z	JKP48Z	23.77	23.76	25.40	22.83	23.72	23.61
hZNF012Z0R1Z 40S ribosomal protein RPS16	+	0.90	-1.04	5	5	5	40.3	40.3	40.3	14.419	0	16.86	9.64E-08	33	MR01201	MR01201	26.28	27.53	27.66	26.09	27.20	26.74
hZNF107H10A1 Peptidase activator PMS2	+	0.41	-1.06	5	5	5	23.2	23.2	23.2	26.011	0	25.41	7.45E-08	8	HOY10E	HOY10E	27.56	26.97	27.41	27.30	24.08	27.30
hZNF1N4Z1H1 Hydroxybenzyl doly HSD12	+	0.57	-1.07	2	2	2	10.1	10.1	10.1	37.32	0	18.41	2.28E-08	14	OY1N16	OY1N16	26.46	25.96	25.21	25.40	25.25	23.16
hZNF026R1P1S1 Peptide heat shock HSP90AB2P	+	0.41	-1.08	6	1	1	16.3	3.9	3.9	44.348	0	3.401	4.9E-08	13	GH0978	GH0978	27.05	26.36	26.35	26.68	26.68	23.37
hZNF104ZC1K1 Cytokine CML	+	2.03	-1.14	7	7	7	39	39	39	33.777	0	6.05	1.39E-08	31	PA6781B	PA6781B	26.69	26.64	26.46	27.09	27.40	27.68
hZNF017Z0R1Z Chromatin loop CT CHTD1	+	1.11	-1.17	2	2	2	11.7	11.7	11.7	23.661	0	16.42	1.54E-08	12	XBP1201	XBP1201	25.47	24.56	24.65	23.36	23.29	24.94
hZNF127LZUK1Z1 Sonchomycin RSR41	+	2.06	-1.19	7	7	7	26.1	26.1	26.1	28.329	0	20.09	8.86E-08	32	LK7L3J	LK7L3J	28.36	27.87	27.52	26.85	26.70	26.83
hZNF018ZEG1 Galactin7 LGAL87	+	1.28	-1.23	4	4	4	35.3	35.3	35.3	15.075	0	12.68	6.78E-08	17	PA4709	PA4709	26.78	27.71	28.98	26.21	26.61	26.22
hZNF016R0ZAT1 Lung nuclear amino G127AS	+	1.10	-1.27	2	2	2	6.3	6.3	6.3	36.01	0	16.79	2.91E-08	17	GH0480	GH0480	26.07	26.96	26.38	25.39	23.16	25.37
hZNF026Z0R1Z Cysteine CDSNA	+	0.89	-1.28	3	3	3	9.6	9.6	9.6	51.539	0	45.11	8.98E-08	16	GH0480	GH0480	27.80	26.81	26.77	26.06	27.12	26.36
hZNF016R0ZAT1 BSA-like protein 2 BSA2B80A2	+	0.89	-1.29	2	2	2	46.3	46.3	46.3	6.3612	0	15.71	1.38E-08	5	H03Y16	H03Y16	25.07	25.61	24.99	22.63	24.49	24.68
hZNF356R1P1Z Adenoviral RNA pol S181	+	1.64	-1.29	7	7	7	46.5	46.5	46.5	14.995	0	26.62	3.66E-08	34	PS386P	PS386P	30.31	30.36	29.34	28.86	28.45	28.82
hZNF136ZPLA1 Junction plasmogon JUP	+	1.58	-1.31	23	23	23	33.8	33.8	33.8	81.744	0	22.74	1.31E-08	179	P14832C	P14832C	31.58	32.39	31.25	30.13	30.72	30.44
hZNF026Z0R1Z Damsolone1 DSG1	+	1.23	-1.31	10	10	10	16.2	16.2	16.2	93.834	0	18.61	4.98E-08	49	GH0554Z	GH0554Z	30.05	30.05	29.28	28.83	28.16	28.65
hZNF008R1R01 Arginase-1 ARG1	+	1.66	-1.32	13	13	13	37.1	37.1	37.1	21.765	0	10.56	2.5E-08	33	PS0588P	PS0588P	28.97	28.94	28.32	27.66	25.54	25.19
hZNF017Z0R1Z Peptidase col de PDCD6	+	1.38	-1.35	2	2	2	10.1	10.1	10.1	21.664	0	4.346	6.94E-02	6	OTS0402	OTS0402	25.05	24.79	24.77	23.44	22.78	24.33
hZNF017H10B1 Nuclear pore complex NUP93	+	0.62	-1.37	3	3	3	33.8	33.8	33.8	15.23	0	6.954	1.87E-08	4	H03Y11	H03Y11	25.26	24.99	25.07	25.72	27.29	22.69
hZNF017H10B1E Sigan B12 BSRPNB	+	0.83	-1.39	6	6	6	24.9	24.9	24.9	19.997	0	25.62	1.12E-08	17	HOY10E	HOY10E	26.83	26.57	26.61	27.10	26.95	26.89
hZNF150ZESP1 Damsolone DSG7	+	1.46	-1.42	102	102	102	32.6	32.6	32.6	39.777	0	32.93	3.12E-08	58	P15845P	P15845P	32.97	32.74	32.27	31.26	31.78	31.67
hZNF300ZAT1Z1 Inhibin alpha3m3y ITGA3	+	1.30	-1.42	2	2	2	1.9	1.9	1.9	16.61	0	4.294	1.35E-08	5	P2060P	P2060P	25.07	24.99	25.30	23.15	24.27	23.65
hZNF016R0ZAT1 Hydroxybenzyl doly HSB88B1D	+	2.28	-1.45	4	4	4	64.4	64.4	64.4	9.67	0	11.53	3.57E-08	16	FW016P	FW016P	26.88	26.98	26.22	25.04	25.40	25.31
hZNF026Z0R1Z Damsolone1 DSG1	+	1.33	-1.45	18	18	18	24.9	24.9	24.9	115.75	0	31.54	1.02E-08	124	GH0480C	GH0480C	31.20	32.15	30.88	29.97	30.26	30.02
hZNF016R0ZAT1 Peptide hydroxybenzyl doly PMS1	+	1.17	-1.46	5	5	5	25.9	25.9	25.9	15.944	0	12.28	2.72E-08	33	GH0480C	GH0						

Supplementary Table 2. List of siRNAs

Target	Sequence (5'-3')
BRCA1	AGAUAGUUCUACCAGUAAA
ZNF384-1	GCACAUCCGUAUACACUCA
ZNF384-3	GGCAACACAACAAAGAUAA
DNA-PKcs	CUUUAUGGUGGCCAUGGAG
Ku80	CAAGGAUGAGAUUGCUUUAGU
Luciferase	CGUACGCGGAUACUUCGA
PARP1	CCAUCGAUGUCAACUAUGA
XRCC4	AUAUGUUGGUGAACUGAGA
PARP3	SMARTpool: ON-TARGETplus (Dharmacon)
Ku70	SMARTpool: siGENOME (Dharmacon)

Supplementary Table 3. List of primers

Name	Sequence (5'-3')
HindIII FW	TAAAAAGCTTATATGGAAGAATCTCACTTCAATTCTAAC
KpnI RV	TAATAATGGTACCCTAAGAGCTGGCCAGGTGC
ZNF384-3_siRNAres_ HindII Rv	ACTTGAAGGGCTTGTCTTATTATGCTGTCGTCT
ZNF384-3_siRNAres_KpnI FW	AGACGACAGCATAATAAGGACAAGCCCTTCAAGT
CMV1 FW	TGGCCCGCCTGGCATTATGCC
CD4int RV	GCTGCCCCAGAATCTTCTCT
M13 FW	GTAAAACGACGGCCAGT
M13 RV	CAGGAAACAGCTATGAC
ZNF384 ΔN-terminus(1-209) Fw	CGAGCTCAAGCTTATATGGACCATCAGAAAGAC
ZNF384 ΔN-terminus(1-209) Rv	GCCGTCTTTCTGATGGTCCATATAAGCTTGAGC
ZNF384 ΔC2H2(205-410) Fw	ATGCTGGAATCAGGGCTGGCAGTGGCCAG
ZNF384 ΔC2H2(205-410) Rv	GGCCTGGGCCACTGCCAGCCCTGATTCGTC
ZNF384 ΔC-terminus(401-516) Fw	CCGCCTGATCTTCAGCCGTTTAAACCCGCT
ZNF384 ΔC-terminus(401-516) Rv	AGCGGGTTTAAACGGCTGAAGATCAGGCGG
ZNF384 N-terminus Fw	ATTAAAAAGCTTCTATGGAAGAATCTCACTTC AATTCTAACCC

Name	Sequence (5'-3')
ZNF384 N-terminus Rv	TAATAATGAATTCTTAGAATTCTTAATCATCATCCT CAGGGGAGAGGAC
ZNF384 C-terminus Fw	ATTAAAAAGCTTCTCAACAGGTGCAGGCAGCAG
ZNF384 C-terminus Rv	TAATAATGAATTCTTAAGAGCTGGCCAGGTGC
ZNF384 C2H2 Fw	ATTAAAAAGCTTCTCCCGAGATGAATGACCC TTATGTCC
ZNF384 C2H2 Rv	TAATAATGAATTCTTATGCCGCTGCTGCTGCTG
pET-His6-MBP-ZNF384 Fw	TACTTCCAATCCAATGCAATGGAAGAATCTCACTTC AATTCTAAC
pET-His6-MBP-ZNF384 Rv	TTATCCACTTCCAATGTTATTACTAAGAGCTGG CCAGGTG
pET-His6-MBP-N-term Fw	ATTAAAAATATTATGGAAGAATCTCACTTCAATT CTAACCC
pET-His6-MBP-N-term Rv	TAATAATGGATVVTTAATCATCATCCTCAGGGG AGAGGAC
pET-His6-MBP-C-term Fw	ATTAAAAATATTCAACAGGTGCAGGCAGCAG
pET-His6-MBP-C-term Rv	TAATAATGGATCCCTAAGAGCTGGCCAGGTGC
pET-His6-MBP-C2H2 Fw	ATTAAAAATATTCCCGAGATGAATGACCCTTATGTCC
pET-His6-MBP-C2H2 Rv	TAATAATGGATCCTTATGCCGCTGCTGCTGCTG
ssDNA T-strand / 3'overhang FW / dsDNA ^{3'-T} FW	/5Biosg/CGCTATCGTCTACGTCATGATCGCAGAAAAAG AAAAAAAAAGAA
ssDNA A-strand / dsDNA ^{5'-T} FW	TTCTTTTTTTTTTCTTTTTCTGCGATCATGACGTAG ACGATAGCG
forward 5'overhang / dsDNA ^{3'-T} RV	CGCTATCGTCTACGTCATGATCGC
5'overhang RV	/5Biosg/CGCTATCGTCTACGTCATGATCGC
3'overhang RV	/5Biosg/GCGATCATGACGTAGACGATAGCGTTCT TTTTTTTTTCTTTTTCT
dsDNA ^{3'-T} RV	AGAAAAAGAAAAAAAAAAGAACGCTATCGTCTACG TCATGATCGC
RNA U-strand	/5Biosg/GCGAUC AUGACGUAGACGAUAGCGUUCUUUU UUUUUCUUUUUCU

Supplementary Table 4. List of primary antibodies

Protein	Host	Company	IF	WB
BRCA1	Mouse	Santa Cruz (sc-6954)		1:500
DNA-PKcs	Mouse	Abcam (clone 18-2)		1:750
p-DNA-PKcs (S2056)	Rabbit	Abcam (ab18192)		1:750
GFP	Mouse	Roche (11814460001)		1:2500
Ku80	Rabbit	Santa Cruz (H-300, sc-9034)	1:500	1:1000
PAR	Rabbit	Enzo Lifesciences	1:1000	1:2000
Ku70	Mouse	Santa Cruz (sc-17789)		1:1000
RAD51	Mouse	GeneTex (clone 14B4)	1:200	
α -Tubulin	Mouse	Sigma (cloneDM1A, T6199)		1:5000
XRCC4	Rabbit	Gift from D. van Gent	1:500	
XRCC4	Mouse	SAB (40455)		1:1000
ZNF384	Rabbit	Abcam (ab176689)		1:1000
γ H2AX	Mouse	Millipore (clone JBW301, 05-636)	1:2000	1:1000
PARP1	Rabbit	Cell signaling (9542S)		1:1000
GFP	Mouse	Sigma (11814460001)		1:1000
H3	Rabbit	Abcam (ab1791)		1:10000
LIG4	Rabbit	Abcam (ab193353)		1:1000
53BP1	Rabbit	Novus Biologicals (NB100-304)		1:2000
γ H2AX	Mouse	Upstate (clone JBW301, #05-636)	1:100	
ZNF384	Rabbit	ATLAS antibodies	1:1000	
PARP3	Rabbit	Gift from F. Dentzer		1:10000
Geminin	Rabbit	Proteintech (10802-1AP)	1:400	
ATM	Rabbit	Cell signaling (clone D2E2)		1:2000
pATM (S1981)	Mouse	Cell signaling (4526)		1:2000
CHK1	Mouse	Santa Cruz (clone G-4, sc8408)		1:1000
pCHK1 (S345)	Rabbit	Cell signaling (clone 133D3)		1:1000
RPA32	Mouse	Abcam (ab1275)	1:1000	
PARP2	Mouse	ENZO lifesciences		1:1000
Pan-ADPr	Rabbit	Sigma (MABE1016)		1:1500
Actin	Rabbit	Sigma (A5060)		1:1000
MBP	Mouse	NEB (E8032S)		1:10000

Supplementary Table 5. List of biotin-labeled DNA substrates

Name	Sequence
ssDNA T-strand	/5Biosg/-GCGATCATGACGTAGACGATAGCGTTCTTTTTTTTTTCTT TTTCT
ssDNA A-strand	TTCTTTTTTTTTTCTTTTTTCTGCGATCATGACGTAGACGATAGCG- /5Biosg
5'overhang	TTCTTTTTTTTTTCTTTTTTCTGCGATCATGACGTAGACGATAGCGC GCTAGTACTGCATCTGCTATCGC-/5Biosg/
3'overhang	/5Biosg/-GCGATCATGACGTAGACGATAGCGTTCTTTTTTTTTTCTT TTTCTCGCTAGTACTGCATCTGCTATCGC
dsDNA ^{3'-T}	/5Biosg/-GCGATCATGACGTAGACGATAGCGTTCTTTTTTTTTTCTT TTTCTCGCTAGTACTGCATCTGCTATCGCAAGAAAAAAAAAAGAAA AAGA
dsDNA ^{5'-T}	TTCTTTTTTTTTTCTTTTTTCTGCGATCATGACGTAGACGATAGCG AAGAAAAAAAAAAGAAAAAGACGCTAGTACTGCATCTGCTATCGC- /5Biosg/

Supplementary References

1. Sprague, B.L., et al., *Analysis of binding reactions by fluorescence recovery after photobleaching*. Biophys J, 2004. **86**(6): p. 3473-95.
2. Smith, R., et al., *Poly(ADP-ribose)-dependent chromatin unfolding facilitates the association of DNA-binding proteins with DNA at sites of damage*. Nucleic Acids Res, 2019. **47**(21): p. 11250-11267.